

The Pennsylvania State University
The Graduate School
Department of Engineering Science and Mechanics

**ENGINEERING PLASMONICS: AN ENGINEERING APPROACH TO
INTERDISCIPLINARY CHALLENGES**

A Dissertation in
Engineering Science and Mechanics

by
Yanhui Zhao

© 2014 Yanhui Zhao

Submitted in Partial Fulfillment
of the Requirements
for the Degree of

Doctor of Philosophy

December 2014

The dissertation of Yanhui Zhao was reviewed and approved* by the following:

Tony Jun Huang
Professor of Engineering Science and Mechanics
Department of Engineering Science and Mechanics
Dissertation Advisor
Chair of Committee

Jian Xu
Associate Professor
Department of Engineering Science and Mechanics

Bruce Gluckman
Associate Professor, Associate Director
Center of Neural Engineering, Department of Engineering Science and
Mechanics, Department of Neurosurgery

Iam-Choon Khoo
William E. Leonhard Professor of Electrical Engineering
Department of Electrical Engineering

Stephen Benkovic
Evan Pugh Professor and Eberly Chair in Chemistry
Department of Chemistry

Judith Todd
P. B. Breneman Department Head
Department of Engineering Science and Mechanics

*Signatures are on file in the Graduate School

ABSTRACT

“Engineering Plasmonics” describes application-oriented engineering approaches that utilizes the knowledge base of the plasmonic research to address most significant issues encountered in different research fields. By combination of optics and nanotechnology, “Engineering Plasmonics” has been proved to be the answers to many challenges at the nanoscale. This dissertation summaries my exploration and accomplishments within this new direction of plasmonic research, while particularly focusing on: (1) Understanding the fundamental basics of plasmonic physics and designing simple plasmonic devices; (2) Designing and demonstrating engineering plasmonic devices such as plasmonic absorbers and plasmonic color filters that target practical applications of solar energy harvesting and ultra-high resolution display techniques; (3) Developing and innovating single-molecule techniques based on engineering plasmonic methods to address the most fundamental biological problems concerning DNA-replisomes interactions during DNA replication process. As the very first dissertation devoted to this topic, it is an attempt to highlight importance of the plasmonic research from a different perspective and is expected to promote engineering plasmonic researches to target most challenging issues among different research fields.

TABLE OF CONTENTS

List of Figures	vi
List of Tables	xiv
Acknowledgements.....	xv
Chapter 1 Introduction	1
1.1. General Backgrounds on Surface Plasmons and Plasmonics.....	2
1.2. Dissertation Structures	6
Chapter 2 Engineering Plasmonics for Single-Molecule Investigations: T4 DNA Replication Studies	8
2.1. Single-Molecule Studies and Challenges.....	9
2.2. Brief Review on Single-Molecule Techniques	10
2.3. T4 DNA Replication Studies	16
2.4. Engineering Approach for Protein-Protein Interactions in T4 DNA Replisomes: Zero-Mode Waveguide (ZMW)/Microfluidics Hybrid Chip	16
2.4.1. Nanofabricated Zero-Mode Waveguides (ZMWs) for Single Molecule Studies	18
2.4.2. Zero-mode Waveguide Fabrication and Characterization.....	20
2.4.3. Conical Lens-based Dark-Field Illumination on a ZMW/Microfluidic Hybrid Chip	22
2.4.4. Background Noise Levels and Fluorescence of Epi and Dark-Field Fluorescence Microscope	28
2.4.5. Single-Molecule Photobleaching Measurements with ZMWs in the Presence/Absence of Fluorophores in Bulk	29
2.4.6. ZMW/Single-Molecule FRET between DNA-Protein and Protein-Protein Among the T4 Replisomal Proteins	36
2.5. Engineering Approach for Processivity Study of UvsW Proteins on Duplex DNAs: DNA Racks	39
2.5.1. DNA Curtain Technique Stretching DNA Molecules Using Artificial Barriers	40
2.5.2. Towards Engineering DNA Racks: DNA Stretching without Continuous Flow.....	42
2.5.3. Towards Engineering DNA Racks: Capturing Single DNA Molecule using Distributed Metallic Arrows and Metallic Pentagons.....	45
2.5.4. DNA Racks Studying Kinetics of UvsW Proteins Sliding along Stretched DNA Substrate	48
2.6. Summary	52
Chapter 3 Engineering Plasmonics for Practical Applications: Solar Energy Harvest and Color Pixel Display	54

3.1. Near Perfect Absorber Based on Engineering Plasmonic Nanostructures	55
3.1.1. Polarization-Independent Dual-Band Infrared Perfect Absorber Based on A Metal-Dielectric-Metal Elliptical Nanodisk Array	56
3.1.2. Light-Driven Tunable Dual Band Absorber with Liquid-Crystal Plasmonic Asymmetric Nanodisk Array	66
3.2. Transmissive and Reflective Ultra-Small Color Filters Based on Engineering Nanophotonic Nanostructures	75
3.2.1. Reflective Plasmonic Color Filters Based on Lithographically Patterned Silver Nanorod Arrays.....	75
3.2.2. Annular Aperture Array Based Wavelength Selector in the Visible Range...	85
3.3. Summary	94
Chapter 4 Engineering Plasmonics: Manipulating Light at Nanoscale using Active and Passive Plasmonic Devices	95
4.1. Reconfigurable Plasmonic Devices via Active Mediums and Controlling Methods.....	96
4.1.1. Mechanically Tuning the Localized Surface Plasmon Resonances of Gold Nanostructure Arrays	97
4.1.2. High-Contrast Modulation of Nanoplasmonic Signals using Nanoscale Dual-Frequency Liquid Crystals	106
4.2. Light Routing and Re-directing via Passive Plasmonic Nanostructures.....	118
4.2.1. Nanoscale Super-Resolution Imaging via Metal-Dielectric Metamaterial Lens System	118
4.2.2. Beam Bending via Plasmonic Lenses	132
4.3. Summary	142
Chapter 5 Summary and Perspective	144
References.....	149

LIST OF FIGURES

Figure 1-1. (a) Kretschmann configuration for surface plasmon excitation. The matching of wave vectors between surface plasmons and the incident light is achieved with the help of a prism with high refractive index. (b) The large surface plasmon wave vectors can also be obtained with the help of a grating. The grating provides additional wave vector components that can assist the conversion from incident light into surface plasmon waves.	3
Figure 2-1. Different techniques for single-molecule studies. (a) the working mechanism of super resolution microscopies differentiating two adjacent biomolecules with fluorescence labels; (b) magnetic tweezers utilizing magnetic beads to stretch and extend DNA molecules; (c) dual-trap optical tweezers that can suspend DNA molecules in solutions, with addition interrogation laser studying single-molecule dynamics; (d) DNA curtains allows DNA molecules to be aligned and stretched under fluid flow for high-throughput single-molecule reactions, and (e) solid-state nanopores structure detecting electronic signals from single molecules passing through the nanopores. Images are adapted from Ref. [89, 94, 97, 101].	15
Figure 2-2. (a) Schematic of zero-mode waveguide (ZMW) array. The typical ZMWs are subwavelength-diameter cylindrical nanowells in ~100 nm-thick aluminum coated on top of a silica substrate. The magnified square region shows the SEM image of the 90 nm-diameter ZMW used throughout this study. (b) The optical confinement property of ZMW for single-molecule fluorescence studies. As light (i.e., 532 nm green laser) penetrates into a 50- to 100- nm-diameter ZMW from the silica side, its intensity exponentially attenuates to generate an evanescent excitation field of ~zeptoliters (10^{-21} L). This optical property allows for single-molecule fluorescence studies of biomolecular interactions (i.e., interactions between ZMW-immobilized DNA and a DNA-interacting protein in bulk solution) to be carried out in ZMWs at micromolar (μ M) bulk concentrations of fluorescent biomolecules.	19
Figure 2-3. SEM images of (a) a representative ZMW structure (90 nm in diameter) and (b) a ZMW array after developing the E-beam exposed photoresist are shown. SEM images of (c) a ZMW and (d) its array after dry etching and removal of residual photoresist are shown.	22
Figure 2-4. Conical lens-based dark-field microscopy in combination with ZMW/microfluidic chip for single-molecule imaging. (a) The microscope setup was built on an inverted microscope. The 532 nm (Green), 635 nm (Red), and 488 nm (Blue) lasers were superimposed by mirrors (M1-M6) and beam splitters (BS1, BS2). The merged beams were then expanded by lenses (L1 and L2) and rendered into a doughnut shape by a conical lens (CL). Lenses L3 and L4, together with a dichromic mirror (DM) and a field stopper (FS1), directed the beams to focus at the back focal point of a water-immersion 60X objective. Placed on top of the objective, the ZMW/microfluidic channel connected with a syringe pump acted as a sealed reaction chamber. Fluorescence emission signals (Orange arrow) from Cy3 and Cy5 dyes collected through the objective were split by BS3, BS4, M6, and M7 for the dual-channel EMCCD detection. Any peripheral reflected excitation beams (dotted line), which leaked into the detection module, were removed by FS2. (b)	

ZMW/microfluidic chip for single-molecule fluorescence measurements, (c) the doughnut-shape illumination beam (532 nm) rendered by the dark-field illumination configuration, and (d) optical image of a ZMW array.25

Figure 2-5. (a) Detailed view of our setup conducting single-molecule experiment using ZMW/microfluidic hybrid chip. (b) A microfluidic channel design that enables three single-molecule experiments running in parallel at the same time. (c) Our customized optical path for dark-field illumination of ZMW. The dark field image of the 2.8 μm -diameter magnetic beads captured using our system for calibration is shown in (d).27

Figure 2-6. EMCCD images of the background fluorescence in emission detection channels for (a) Cy2, (b) Cy3, and (c) Cy5 for ZMWs in dark field (DFI, Left panel) and Epi (EPI, Right panel) configurations illuminated by the blue (488 nm), green (532 nm), and red (635 nm) lasers, respectively. The ZMWs were free of fluorescent molecules. The fluorescence intensity in the image was color-coded according to the spectral gradient from blue (intensity minimum) to red (intensity maximum). (d) A representative time trace for the background fluorescence in the Cy3 detection channel of ZMWs in Epi (Gray) and dark field (Black) configurations illuminated with the green (532 nm) laser. (e) Fluctuations of the background fluorescence of a representative time trace. The histograms were plotted using the data in (d) and were fit to a Gaussian function to give standard deviations for the noise level of 832 AU for Epi and 312 AU for dark-field. AU: arbitrary units. (f) Distribution of the background fluorescence intensity in the Cy3 detection channel of ZMWs in Epi (Gray) and dark-field (Black) configurations illuminated with the green (532 nm) laser. The mean background values from 250 fluorescence traces from either illumination configuration were plotted in histograms, which were fit to a Gaussian function to give the median background fluorescence levels of 853 ± 417 AU for Epi and 376 ± 61 AU for dark-field.29

Figure 2-7. (a) Schematic of single-molecule photobleaching of the immobilized Cy3-DNA primer in a ZMW using the green (532 nm) laser in either the Epi or dark-field microscopy configurations. ZMWs were functionalized with anti-digoxigenin antibody and then passivated with BSA. A Cy3-DNA primer was immobilized through a digoxigenin: anti-digoxigenin antibody interaction. EMCCD images and IDL analysis results of the Cy3-primers immobilized in ZMW arrays excited by the 532 nm laser in the Epi or dark-field configuration are shown. Fluorescence intensity was color-coded according to the spectral gradient from blue (intensity minimum) to red (intensity maximum). AU indicates arbitrary units. Representative single-step photobleaching trajectories of the Cy3-DNA primer excited by the 532 nm green laser in the (b) Epi and (c) dark-field configurations. (d) Distribution of the signal-to-noise ratio (S/N) in the single-molecule photobleaching measurements using the Epi (Gray) and the dark-field configurations (Black). Histograms were plotted using the S/N values from 240 (Epi) and 253 (dark-field) photobleaching events. The mean S/N ratios for the Epi and dark-field microscopies were 1.78 and 5.13, respectively. (e) Distribution of the fluorescence duration of the immobilized Cy3-DNA primers in single-molecule photobleaching measurements using the Epi (Red) and dark-field (Gray) configurations. Single-exponential fitting yielded the

- fluorescence durations (τ) of 11.11 ± 1.22 s ($n = 373$) for the Epi and 13.80 ± 2.43 s ($n = 412$) for dark-field setup.32
- Figure 2-8. (a) Schematic of single-molecule photobleaching of the immobilized Cy3-DNA primer in ZMWs in the presence of bulk gp59(C42)-Cy5 excited by the green (532 nm) laser in the dark-field illumination configuration. Representative time traces of the single-molecule photobleaching of the Cy3-DNA primer in the presence of (b) 1 μ M, (c) 100 nM and (d) 10 μ M gp59(C42)-Cy5. The fluorescence intensities of the Cy3 and Cy5 channels are in green and red, respectively. (E) Distribution of the S/N ratio in the single-molecule photobleaching measurements of the Cy3-DNA primer in the presence of 0 nM (Blue), 100 nM (Black), 1 μ M (Dark gray), 3 μ M (Gray), 6 μ M (Red, dot line) and 10 μ M (Red, dash line) gp59(C42)-Cy5. (F) Mean S/N ratios ($\langle S/N \rangle$) and probability of S/N ratio larger than 3 as a function of gp59(C42)-Cy5 concentration.34
- Figure 2-9. (a) Representative FRET and FRET efficiency trajectories for the interaction between the Cy3-ssDNA primer and gp59(C42)-Cy5 in a ZMW. gp59(C42)-Cy5 was at 1 μ M bulk concentration. The fluorescence intensities of the Cy3 and Cy5 emissions are in green and red, respectively. (b) A magnified view of the FRET events and their FRET efficiency in the square region of (a). (c) FRET and FRET efficiency time trajectories show the presence of three major FRET states with apparent FRET efficiencies of 0.37, 0.45, and 0.6. (d) Representative FRET and FRET efficiency time trajectory between the gp59(C42)-Cy3 and Cy5-N-gp43(exo-) on the immobilized DNA primer in a ZMW.37
- Figure 2-10. (a) DNA curtain stops and stretches DNA molecules at a nano barrier or engineered straight line. (b) DNA curtains formed utilizing the discontinuities carved in glass substrate. Both cases can accumulate, stretch, and align DNA molecules for single-molecule experiment.41
- Figure 2-11. (a) Functionalization of duplex DNA molecules with one end modified with biontin, and the other end modified with digoxigenin. The biotin and digoxigenin will form chemical links with neutravidin and antidigoxigenin, respectively. (b) DNA molecules stretched with a modified DNA curtain design with two stop barriers. The dig end of DNA molecules will form chemical links to the second stop barrier which is treated with thiol-antidig. The DNA molecules can then be stretched even without continuous flow.43
- Figure 2-12. The design and optical image of “zigzag” nanostructure to stop, stretch, and isolate DNA molecules flowing the contour of the zigzag shape. The EMCCD results confirmed the structure can be used to stretch and isolate DNA molecules. The DNA molecules are stretched without any hydrodynamic forces.45
- Figure 2-13. The design and optical image of distributed metallic nano arrows and pentagons that can capture and stretch on single DNA molecules. The break on the continuity of the original zigzag nanostructure design has significantly reduced the accumulation of a large number of DNA molecules at one capturing spot, offering better single-molecule signals and more single-molecule event numbers as compared with the original design.46

- Figure 2-14. EMCCD images of distributed metallic arrows and pentagons for single DNA molecule capturing and stretching. The Cy3 channel shows the fluorescence labeled DNA molecules that are captured and stretched at different arrow-pentagon sites. The uniformity of the fluorescence signals confirm many single-molecule events in one observation regions. The Cy5 channel indicate the quantum dot signals that are correlated to the positions of T4 replisome proteins.47
- Figure 2-15. The EMCCD images of the same observing region before and after adding ATP. Because quantum dots don't photobleach, the missing quantum dots signals after adding ATP are likely caused by the movements, and possible sliding off, of the UvsW protein labeled with those quantum dots.....48
- Figure 2-16. The trace of UvsW movement confirmed by the changes on captured signals from one quantum dots.49
- Figure 2-17. Kymography analysis on sliding of UvsW proteins along stretched lambda DNAs using Nikon NIS software.....50
- Figure 2-18. Tracking results of quantum dots signal movements recorded as kymographs using Nikon NIS. The control experiment with and without ATP confirmed sliding of UvsW protein under ATP hydrolysis. The dynamics of UvsW have been confirmed as back and forth sliding behaviors, as well as preferable sliding directions towards certain ends of stretched DNA molecules.....52
- Figure 3-1. Schematic of the dual-band perfect absorber structure and the incident polarization configuration. (b) A SEM image of the designed structure.57
- Figure 3-2. The reflection and transmission spectra under normally incident electromagnetic plane waves with the fixed polarization state given in Fig. 1(a). Results are shown in linear scale (a) and logarithmic (dB) scale (b), respectively.....59
- Figure 3-3. Simulated reflectance spectra of the designed absorber structure at normal incidence with different dimensions of the elliptical gold nanoparticles. A 700 nm tunable range can be conveniently achieved by engineering the sizes of the gold nanoparticles on the top layer. The two absorption peaks can be easily tuned both (a) in parallel and (b) independently.....60
- Figure 3-4. The simulated absorption efficiencies as a function of wavelength and angle of incidence under (a) TE and (b) TM polarization.61
- Figure 3-5. Measured and simulated reflection spectra of the dual-band absorber under (a) TE polarization and (b) TM polarization at normal incidence.63
- Figure 3-6. Calculated charge and field distribution at resonances (a) (c) $\lambda_1 = 1697$ nm (cross section given along major axis) and (b) (d) $\lambda_2 = 1247$ nm (cross section given along minor axis) where perfect absorbance occur. Anti-parallel currents are indicated by the charge distribution and the enhanced electric fields are confined between the top gold nanodisks and the bottom gold mirror.65

- Figure 3-7. Schematic of light-driven tunable plasmonic absorber. Light sensitive liquid crystal mixture on top of the absorber can be modulated with light. (b) The top layer consists of two sets of alternatively arranged two dimensional nanodisks with the same period, followed up by a spacing layer of SiO_2 and a bottom gold layer. (c) SEM images of fabricated near perfect plasmonic absorber working at dual frequencies.67
- Figure 3-8. (a) Two design instances of the near-perfect plasmonic absorber (i) $a = 300$ nm, $b = 200$ nm, and (ii) $a = 280$ nm, $b = 180$ nm. FDTD simulations show that near perfect absorption can be achieved at selected wavelength ranges (b) Experiment results of the two designs Over 90% absorbing efficiencies can be achieved.69
- Figure 3-9. (a) Experimental setup for measuring optically tunable plasmonic absorber. (b) FDTD simulation results of the performance of the plasmonic absorber with an overlayer of liquid crystals Around 30 nm shiftiness can be observed. (c) Measured absorption band shifts with the pumping light turned ON and OFF. The band shifting process is reversible and repeatable. (d) Zoom in view of the first absorption dip. Around 25 nm shift can be observed. (e) Zoom in view of the second absorption dip. The shift is around 20 nm.72
- Figure 3-10. Schematic diagram of the color filter working under reflection mode.76
- Figure 3-11. (a) SEM image showing the top view of a silver nanorod array with period $p = 550$ nm. (b) Measured and (c) calculated reflection spectra for nanorod arrays with periodicities from 400 nm to 700 nm. The arrow indicates increasing periodicities.78
- Fig. 3-12. Calculated reflection of nanorod arrays with constant periodicity $p = 400$ nm and varying inter-rod gaps and diameters corresponding to different d/p values ranging from 0.375 to 0.875.....81
- Figure 3-13. SEM images showing oblique views of dense nanorod arrays with different periodicities from (a) 540 nm to (e) 320 nm in step size of 55 nm. (f) Magnified top view of (d) with $p = 375$ nm and $d = 350$ nm.83
- Figure 3-14. (a) Optical image showing the reflective colors from different silver nanorod arrays. Measured reflection (b) and transmission (c) spectra of the corresponding arrays as a function of wavelengths.84
- Figure 3-15. Schematic drawing of the proposed wavelength selector working under transmission measurement.87
- Figure 3-16. SEM images showing (a) overview of a fabricated 9 by 9 AAA and (b) magnified view of a single ring with 25 nm gap width. (c) Measured and (d) simulated transmission spectra of AAAs as a function of gap width. Simulated spectra are normalized for clarity. The apertures have fixed inner radius at 200 nm and varying outer radii from 225 nm to 270 nm in steps of 15 nm. The arrow in (c) indicates decreasing gap width. Inset of (d), magnified peak tops with 700-800 nm wavelength range to show the shift more clearly90

- Figure 3-17. Top panel: top view; Bottom panel: cross sectional view of electric intensity distribution of a single ring with 55 nm gap width illuminated at 740 nm (λ_{\max}) and 600 nm (λ_{\min}), respectively.....92
- Figure 3-18. SEM images of the fabricated AAAs with (a) 40 nm, (b) 80 nm, (c) 120 nm, and (d) 160 nm gap width (outer radii equal to 240 nm, 280 nm, 320 nm, and 360 nm with 200 nm fixed inner radius). Scale bars are 200 nm. (e) Corresponding optical image presenting different colors. (f) Measured transmission spectra of the AAAs with different color outputs shown in (e).....93
- Figure 4-1. Schematic of the experimental setup. The active tuning of LSPR of the Au nanodisk arrays is achieved by mechanically stretching the sample.....98
- Figure 4-2. Procedures of fabricating Au nanostructure arrays on a PDMS substrate using the Langmuir-Blodgett technique, deposition, and etching: (a) Disperse PS nanospheres in DI water. (b) Compress the squeeze bars to form a compact monolayer of PS nanospheres. (c) Attach a smooth PDMS substrate to the monolayer of nanospheres. (d) The bonding force between PS nanospheres and PDMS substrate helps to transfer the nanosphere arrays onto the surface of PDMS substrate. (e) Reshape nanospheres using plasma etching. (f) Deposit Cr/Au on top of the nanosphere arrays. SEM images of the sample after step (e) and (f) are shown in (g) and (h), respectively.100
- Figure 4-3. (a) Microscopic image of Au nanodisk array immobilized on a PDMS substrate. Three axes of the hexagonal array are marked for measuring the geometry change upon stretching. (b–d) The measured change in array period along three axes.102
- Figure 4-4. Measured (a) and FDTD-simulated (b) LSPR reflectance spectrum of the Au nanodisk arrays immobilized on a PDMS substrate in the relaxed state.....103
- Figure 4-5. (a) Extinction spectra recorded from the Au nanodisk arrays immobilized on a PDMS substrate undergoing various levels of stretching. A blueshift of reflectance peak wavelength is observed. (b) Shift of reflectance peak wavelength as a function of amount of stretch. A tunable reflectance peak shift up to 30 nm is achieved.....104
- Figure 4-6. Schematic of the DFLC-based nanoplasmonic modulator. An SPP is excited through diffraction-mediated transfer of momentum from the input. The SPP wave (shown here in pink) then propagates through the DFLCs, which exhibits either an ordinary or extraordinary refractive index, depending on the frequency of an applied voltage. Thus, the signal enters the interference stage at a phase that is dependent on the path length traveled and refractive index of the DFLC. Finally, a pump beam creates an interference pattern with the plasmonic signal, which is read as output information.....107
- Figure 4-7. (a) Detailed geometry of the DFLC-enabled plasmonic modulator. The groove-slit separation distance is denoted as D , and is used as a parameter to find a usable modulation depth, while maintaining nanoscopic dimensions. The 200 nm gray layer represents the DFLC, whereas the tan structure is silver, modeled

- according to the Drude approximation. The entire structure is surrounded by air. (b) Field intensity plots for 1-groove, 1-slit device in the (b) ON state and (c) OFF state. The relative magnitude of the Poynting vector is shown against the two-dimensional geometry of the device. 112
- Figure 4-8. Amplitude contrast for single-groove device. Measurements were conducted at 25 nm intervals over the given range of groove-slit separation distances. The distance at which the phase difference between the SPP waves is greatest is marked for clarity. This distance corresponds to $D = 450$ nm, at which a modulation depth of ~ 8 dB was exhibited. Notably, the magnitude of contrast at $D = 325$ nm and $D = 600$ nm is comparable to that at $D = 450$ nm. 113
- Figure 4-9 (a) Detailed geometry of the double-groove single-slit DFLC-enabled nanoplasmonic modulator. Field intensity plots for the (b) ON state ($n = n_o$) and (c) OFF state ($n = n_e$). The relative magnitude of the Poynting vector is shown against the two-dimensional geometry of the device. 115
- Figure 4-10. Intensity contrast for 1-groove and 2-groove devices. The contrast of the 2-groove device is ~ 15 dB whereas the 1-groove device exhibits contrast of ~ 8.1 dB. 116
- Figure 4-11. Intensity contrast for 2-groove device with three different observation planes. The contrast measured at each plane is ~ 15 dB, verifying that, while the power of the signal decreases with distance from the lower slit edge, the contrast between corresponding n_o and n_e signals remains constant. 117
- Figure 4-12. Schematic of the metamaterial lens system for imaging. Incident light passing through slit object will diverge in metamaterial lens 1 (ML1) and converge in metamaterial lens 2 (ML2), forming an image on the top surface of ML2. 121
- Figure 4-13. (a) Hyperbolic dispersion relations for $\epsilon_x < 0, \epsilon_z > 0$ (blue) and $\epsilon_x > 0, \epsilon_z < 0$ (red). The arrows indicate the direction of group velocity for two frequencies with $\omega_1 < \omega_2$. The dashed circle represents the dispersion curve for isotropic materials. (b) Schematic of imaging process by ML1 ($\epsilon_x < 0$ and $\epsilon_z > 0$, below) and ML2 ($\epsilon_x > 0$ and $\epsilon_z < 0$, above). 122
- Figure 4-14. The simulation result of ML imaging, corresponding to the structure shown in Figure 4-12. (b) The normalized intensity of the images of two slit objects on the input and output planes. Two slit objects are 20 nm in width each and their center-to-center distance is 40 nm. 124
- Figure 4-15. (a) The dispersion curves in first quadrant for a fixed frequency calculated by EMT and TMM with the same parameters. (b) The ray trace in the imaging structure, estimated using EMT and TMM, the inner plot shows the different shift errors corresponding to different k_x 127
- Figure 4-16. (a) Focus with full-width-half-maximum (FWHM) of 25 nm is achieved when the thickness is 5 nm for each layer and the total thickness of the imaging structure is 200 nm. (b) FWHM is ~ 35 nm when the layer thickness is increased to 10 nm and the total thickness of the structure is 400 nm. (c) The FWHM is ~ 400 nm

when the thickness of each film is 20 nm and the total thickness of the structure is 800 nm. (d) Using the same structure in Figure 5(c) while changing the thickness ratio of ML1 and ML2 based on the ray trace analysis. The size of the focus reduced back to 40 nm. 130

Figure 4-17. (a) The comparison of our lens system with a hyperlens configuration under the perfect matching condition ($Re(\epsilon_m) = -\epsilon_d$). Comparable transmission (around 10 %) can be observed in both systems. (b) Much higher transmission (50 %) can be achieved in our lens system (30 %) when the system is redesigned with fewer layers. All the results are obtained through a cross section cut from the center of slit through the center of the lens. 131

Figure 4-18. (a) Schematic of a plasmonic lens that can bend a light beam or focal point in transverse direction; (b), (c) and (d) are the isometric views of three proposed designs of the plasmonic lens, termed as Lens I, Lens II, and Lens III. 134

Figure 4-19. (a) Relative phase change caused by varying the width of a rectangular slit w . (b) Relative phase difference caused by varying the length of the slit d . (c) Relative phase difference of a tapered slit. The input aperture w_1 is varying, while the output aperture w_2 is fixed at 50 nm. 135

Figure 4-20. (a), (c) and (e) are three representative designs of plasmonic lenses (Lens I, Lens II, Lens III), corresponding to Fig. 1(b), (c) and (d). The constructed phase differences are 1.5π , 0.96π , and 1.45π , respectively. (b), (d) and (f) the corresponding simulation results. All the simulations show the bending of light off the optical axis. 139

Figure 4-21. Influence of different incident angles on the bending effects of Lens III. The red dashed lines denote the phase front change caused by both incident light and plasmonic lenses. (a) Schematic of light incidence at an angle of -10° to the optical axis; (b) Simulation results corresponding to (a). (c) Schematic of light incidence at an angle of 10° to the optical axis. (d) Simulation results corresponding to (c). 142

LIST OF TABLES

Table 3-1. Absorption efficiencies of different angles for each peak under TE and TM polarization.....	61
Table 3-2 Optimized parameters of the nanorod arrays and the corresponding reflected colors.....	84
Table 4-3. Efficiency calculation of the proposed plasmonic lenses	140

ACKNOWLEDGEMENTS

Research is fun and painful. However, it could be much more painful without the aid of great mentors to guide, advice, and also share successes as well as failures with you. I feel very fortunate to have so many great scientists and researchers as my mentors in my research, with some of the mentoring eventually developing into long-term friendship and potential collaboration. I want to express my deepest gratitude to my adviser, Prof. **Tony Jun Huang**. Without his unconditional supports and encouragements, this dissertation would not be possible.

My most sincere thankfulness also goes to my committee members: Professor **Stephen Benkovic** from Penn State Chemistry Department, Professor **Iam-Choon Khoo** from Penn State Electrical Engineering, Professor **Bruce Gluckman** from Penn State Engineering Science and Mechanics and Neurosurgery, and Professor **Jian Xu** from Penn State Engineering Science and Mechanics. In addition, I want to thank Professor **Guangyuan Si** from Northeastern University in China, Dr. **Yan Jun Liu** from A*STAR Singapore, Dr. **Danqi Chen** from Penn State Chemistry Department, Dr. **Chenglong Zhao** from National Institute of Standards and Technology. The list would go much longer without the page limit, and I really want to thank all those who have helped me in the past!

I also want to thank my wife **Lan Lin**, and my parents **Xicai Zhao** and **Yanhua Zhang**, as well as **Dale Wright** and **Teresa Wright**. Thank you for your caring and supports for the years passed and the years to come. Your loves are my power taking over challenges and seeking for personal improvements!

Last but not least, I want to take this opportunity to thank the finical supports from the **Penn State University**, **Penn State Alumni Associations**, **the Optical Society (OSA)** and **the Canadian Associations of Physicists (CAP)**, and **the International Society of Optics and Photonics (SPIE)**.

Chapter 1

Introduction

Plasmonics describes the unique interactions that take place between light and matter at the micro/nano scale. [1-6] At such small length scales, the free electrons in a metal or semiconductor play a significant role in altering the behavior of incoming electromagnetic radiation. Similarly, incoming electromagnetic radiation can interact with free electrons and produce notable changes in a material, such as localized heating. Although the underlying mechanisms are quite simple, the applications of plasmonic devices are diverse and have been employed to solve many of the challenges that arise from large scale limitations on light-matter interactions. The success of plasmonic research is largely due to its integration with other research disciplines, such as material sciences and life sciences, leading to the inventions of new “clocking” materials [7-11] that don’t exist naturally in the world, as well as small “satellites” that investigate internal organ structures inside single cells. [12-15] While some view plasmonics as an already mature field without many new physics left to explore, its huge potential and promising future as an engineering approach has yet to be discovered. The destiny of plasmonics and its inevitable merger with other disciplines such as biology and microfluidics are by no means accidental. Each field possesses inherent challenges and those are the opportunities of the other fields. Biological studies focus on the most significant problems and challenges of all research fields, concerning the health of the whole human beings, but generally falls behind other engineering fields in terms of technology development due to various reason. Here, I want to solve this problem through a new research topic of “Engineering Plasmonics”, which is based on

plasmonic fundamental physics but expressed in engineering ways to really consider the needs from another field.

Engineering Plasmonics describes the engineering approaches that are application-oriented, which utilize the knowledge base of the plasmonic research but emphasizing its objective to address most significant issues encountered by different research field. It serves as an engineering approach combining the optics and nanotechnology, and is the answer to lots of challenges at the nanoscale. My research work over the past five years have been focused on: (1) Understanding the fundamental basics of plasmonic physics and designing simple plasmonic devices; (2) Designing and demonstrating engineering plasmonic devices such as plasmonic absorbers and plasmonic color filters that targeted practical applications of solar energy harvesting and ultra-high resolution display techniques; (3) Developing and innovating single-molecule techniques based on engineering plasmonic methods to address the most fundamental biological problems concerning DNA replisomes interactions during DNA replication process.

1.1. General Backgrounds on Surface Plasmons and Plasmonics

Surface plasmons are a special kind of light formed by collective electron oscillations at the interface of a noble metal and dielectric. [16-19] They can only propagate at the metal/dielectric interface and decay exponentially away from the interface. Surface plasmons exhibit different properties as their counterparts with the same frequencies, like much larger wave vectors, very short wavelengths, and limited propagating length with the dumping loss while propagating inside the metal. They also fit into Maxwell equations and the wave vector supported by different combinations of metal and dielectric interfaces can be calculated by solving the equation as shown below: [19]

$$k_{sp} = k_0 \sqrt{\frac{\epsilon_m \epsilon_d}{\epsilon_m + \epsilon_d}} \quad (1-1)$$

where k_{sp} represents the wave vector of surface plasmons and k_0 is the wave vector of the incident light in vacuum. ϵ_m and ϵ_d are dielectric constants of metal and dielectric, respectively. From the equation above, it is clear that direct conversion from propagating electromagnetic waves into surface plasmons is impossible due to the mismatch of their wave vectors. There are many different ways to solve this problem and the most commonly used ones are Kretschmann/Otto configurations and gratings, as illustrated in Figure 1-1.

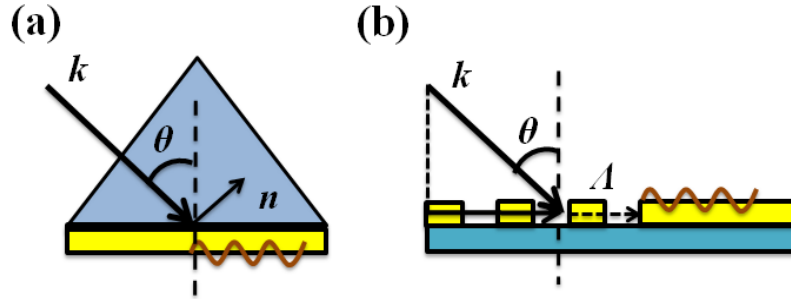


Figure 1-1. (a) Kretschmann configuration for surface plasmon excitation. The matching of wave vectors between surface plasmons and the incident light is achieved with the help of a prism with high refractive index. (b) The large surface plasmon wave vectors can also be obtained with the help of a grating. The grating provides additional wave vector components that can assist the conversion from incident light into surface plasmon waves.

The Kretschmann configuration consists of a prism with high refractive index attaching to a glass slide with refractive index matching to oil; the other side of the glass slide is covered with a thin layer of gold film. There are two metal/dielectric interfaces found in this system as air/gold and glass/gold interfaces. According to Equation (1-1), the two different interfaces support different surface plasmon modes. Incident light from the prism side cannot excite surface plasmons on both interfaces; however, with the help of large refractive index from the prism side,

it is possible that the leakage horizontal wave vectors from the incident light on the prism side will match the surface plasmon wave vector on the air side, validating the relation of

$$n_p k_0 \sin \theta = k_0 \sqrt{\frac{\epsilon_m \epsilon_{air}}{\epsilon_m + \epsilon_{air}}} = k_{sp,air} \quad (1-2)$$

where n_p is the refractive index of the prism, ϵ_{air} is the dielectric constant of air, and θ represents the incident angle from the prism side. One alternative way is to use gratings, where the grating constant provides the missing momentum components from the incident light to surface plasmons. In order to do so, the period of the gratings should be at the close range of the incident wavelength. The equation describing this process can be expressed as:

$$k_{sp} = n_i k_0 \sin \theta \pm m \Lambda \quad (1-3)$$

$\Lambda = 2\pi/d$ is the grating constant (d is the period of grating). n_i is the refractive index of incident plane, θ is the incident angle, and m is integer. Both methods are well investigated and have found their wide applications in plasmonic-related research with many other excitation methods being developed. Sometimes they can be combined together to maximize the system performance. The excitation conditions have to be strictly followed to allow surface plasmons to be excited; while a less strict method requiring irregular sharp edges can also excite surface plasmons through the strong scattering caused wave vector match; however, the exciting efficiency is quite low since only a small amount of wave vectors can match with surface plasmon wave vectors during the exciting process.

Complex mechanisms are involved when periodical plasmonic nanostructure arrays are illuminated with light, including localized surface plasmon resonance (LSPR), [20-22] Wood's anomalies [23-26] and Bloch wave surface plasmon polaritons. [27] The collective plasmonic resonances at different wavelengths are the combined results of all those three effects and their mutual coupling. LSPR can be estimated using the coupling dipole theory, which has been

developed and discussed comprehensively elsewhere. [28, 29] Each single nanoparticle (rod or disk) can be modeled by a dipole of polarizability α , which can be written as: [30]

$$\alpha^{static} \propto V \frac{\epsilon_m - \epsilon_d}{3\epsilon_m + 3\chi(\epsilon_m - \epsilon_d)} \quad (1-4)$$

where ϵ_m and ϵ_d are the relative permittivities of metal and surrounding environment, respectively. χ is the shape factor relating to the physical shape of the nanorod and V is the volume of the nanorod. When the nanorod array is excited by an electromagnetic field with frequency ω , the rod dipole will radiate a scattering field in proportion to its dipole moment. The total LSPR field with an effective polarizability α^* is a combined effect of the incident field and radiations from each individual nanorods, which can be expressed as: [30]

$$\alpha^* = \frac{1}{1/\alpha - S} \quad (1-5)$$

with the array factor S denoting the collective effect of all nanorods and depending only on the geometrical factors of the nanorods. The S factor for a square array of nanorods under normal incidence can be written as: [30]

$$S = \sum_{dipoles} e^{ikr} \left[\frac{(1 - ikr)(3\cos^2 \theta - 1)}{r^3} + \frac{k^2 \sin^2 \theta}{r} \right] \quad (1-6)$$

S is the retarded dipole sum, indicating the collective contributions from all the other dipole impacting on the interested particles. Theta is the angle between position vector and the polarization direction. Depending on the geometries of the nanostructures, S would contribute to radiative damping, or dynamic depolarization effects, and can be solved numerically. More detailed discussion on S can be found in Ref. [30], and other references. [31-33] A peak in the reflection spectrum can be achieved when the condition $S = 1/\alpha$ is satisfied, which is the theoretical basis to build our plasmionic resonating system since designated wavelengths can be separated by varying the sizes and periods of nanorod arrays.

Plasmonics is a research topic covering both surface plasmons, localized surface plasmons resonance, and related interesting phenomena, with its focus on the light-matter interaction occurring at nanoscales along with different nanoparticles and nanostructures. At this scale, light can not only be confined at the metal/dielectric interface, but also can be squeezed, tightly focused/confined, manipulated at will with the assistance from various nanostructures. This unique feature of light manipulation at nanoscale allow huge potentials and enormous opportunities for various plasmonic devices to address issues concerning small-scale light in different field, resulting plasmonic devices such as plasmonic lenses, plasmonic absorbers, zero-mode waveguide, and their applications on different research fields.

1.2. Dissertation Structures

My dissertation is structured into three topics with a last part of summary and perspectives. The three topics are: (1) Engineering Plasmonics for Single-Molecule Investigations: T4 DNA Replication Studies; (2) Engineering Plasmonics for Practical Applications: Solar Energy Harvest and Color Pixel Display; and (3) Engineering Plasmonics: Manipulating Light at Nanoscale using Active and Passive Plasmonic Devices. Each topic will discuss two to four works I have completed and published as journal publications. Each subsection consists of its own storyline as an individual publication, and serves as an example for the major topic I want to discuss. The topics are arranged based on the significance of each subject, starting from the most significant challenges of single-molecule interactions in DNA replications, to plasmonic absorbers and color pixels related to industrial products, to the fundamental understandings on plasmonic physics and simple plasmonic devices. However, the chronical sequence reverses and shows my efforts pushing the plasmonic researches from fundamental physics, to individual devices, to system and platform with much enhanced

functionalities. Even arranged in this way, I hope none of the topic gets devalued because they are equally important and make a complete dissertation together. It indicated the development of a new direction in the whole field of plasmonic research, which emphasizing on the application-oriented techniques that serve as an engineering approach to address challenges in a different field.

Chapter 2

Engineering Plasmonics for Single-Molecule Investigations: T4 DNA Replication Studies

The term “single-molecule” refers to the standalone molecules, such as single nucleic acid, lipid, protein, or dye molecule of different kinds. In contrast to conventional biological studies that often focus on the group behavior of a large number of molecules, single-molecule experiments, which spatially and temporally isolate individual molecules so that they can be observed and manipulated, are capable of distinguishing individual molecular properties from the overwhelming background of bulk populations. In addition, these techniques provide a method for reporting on variations in kinetics and conformational dynamics, existence of rare species, transient intermediates and heterogeneous behaviors among molecules of the same type. Being more unveiling than ensemble methods, single-molecule investigations based on engineering nanophotonic techniques have been successfully employed in the research of fundamental biological processes, gracing the landscape of a broad range of disciplines in the biosciences and biotechnology.[34] In this chapter of engineering nanophotonics for single-molecule investigations, I will discuss my research works on developing innovative single-molecule detection and analysis techniques based on theories and knowledge presented in plasmonic researches, laying down foundations of adopting advanced fabrication techniques together with plasmonic physics to address interdisciplinary challenges in biological fundamental studies.

This section consists of the information from my follow publication and on-going works with necessary adaptations.

Dark-Field Illumination on Zero-Mode Waveguide/Microfluidic Hybrid Chip Reveals T4 Replisomal Protein Interactions, *Nano Letters*, Vol. 14, pp 1952–1960, 2014. [35]

DNA Racks Studying Processivity of UvsW Proteins, to be submitted, 2014.

2.1. Single-Molecule Studies and Challenges

Single molecule studies can reveal unknown molecular dynamics at the single-molecule level and provide an in-depth understanding of the various interactions among different single-molecule units. Specifically, they can provide information on (1) molecular properties including multiple folding and rare states that can not be detected in ensemble experiments; (2) molecular dynamics at or far from equilibrium; (3) the steps in multi-protein complex formation; and (4) the behavior of the molecule at the low concentrations that approach those that are physiologically relevant. To achieve these objectives using a single-molecule approach, the technique must provide (1) high sensitivity to precisely monitor molecular properties and molecular dynamics, and (2) high throughput for sufficient observations for the detection to be statistically significant.

Single molecule techniques in biology refer to techniques that monitor or measure the properties of single biomolecules that participate in a fundamental biochemical reaction. In conventional ensemble bio-experiments, these biomolecules are probed in large numbers, leading to the observation of averaged-out properties of the bulk analytes. The development of improved single-molecule techniques is thus of great interest for the study of complex biological and chemical systems, with the objective to elucidate those details that are inaccessible by conventional ensemble experiments.

Single-molecule fluorescence microscopy is among the plethora of single-molecule techniques that have been devised to interrogate individual molecules and complexes at the molecular level. [36-41] This imaging technique has shown the capacity to discover and quantify

the lifetimes and movements of novel species obscured by ensemble averaging in a broad spectrum of biological systems.[42-54] The pursuit of detailed behavior concerning biomolecules through single-molecule fluorescence imaging, however, encounters the impediment of spatial resolution (~250 nm in lateral) imposed by the wave-like diffraction of light. [55-63] As a result, to maintain single-molecule resolution within the typical focal volume of an ~attoliter (10^{-18} L) of diffraction-limited microscopy, the accessible concentration range of fluorescent species is restricted to nanomolar to sub-nanomolar, markedly lower than the typical micromolar dissociation constants of biomolecular interactions. [38, 64, 65]

A common scheme to overcome this “concentration barrier” in single-molecule fluorescence imaging is to have the fluorescently labeled biomolecules at their optimal concentrations, but to excite only a limited number of molecules in the pool within the focal volume and have the majority of molecules unexcited. [64] This can be achieved by 1) stochastic activation of photoactivatable/switchable fluorophores, as in the case of stochastic optical reconstruction (STORM) and photoactivated localization (PALM) -type super-resolution microscopy and the photoactivation, diffusion, and excitation (PhADE) approach; [66-69] and 2) decreasing the focal volume in fluorescence imaging [70, 71], as in the case of total internal reflection fluorescence (TIRF), confocal, and stimulated emission depletion (STED) microscopies, and zero-mode waveguides (ZMWs). [72-81]

2.2. Brief Review on Single-Molecule Techniques

Conventional solid-state imaging and detection techniques, [82-87] such as scanning electron microscopy (SEM) and surface enhanced Raman scattering (SERS), are not used for single-molecule studies owing to the potential for damage to the molecules during the imaging or detection process. Optical microscopies of limited resolution (~1 μm) are still the major method

for single-molecule observation. Fluorescence labeling is the most common detection method. Thus, most single-molecule techniques rely heavily on developments in optical microscopy and fluorescence detection. Figure 2-1 shows the most popular single-molecule techniques that are currently applied in fundamental single-molecule studies. Brief introductions on each techniques are presented as follows:

Super-resolution microscopies:

Recent development of various super-resolution microscopies provides unprecedented imaging capability, with some methods attaining a maximum resolution down to 20 nm. [69, 75, 88] The working mechanism of these super-resolution microscopes differs from conventional microscopes because it relies on active/passive blinking of fluorophores assisted by advanced imaging processing algorithms. This technique provides significantly improved image quality and resolution for sub-cellular structures such as intracellular organelles. However, there are several drawbacks that hinder their application to many fundamental biological/biochemical problems. Firstly, the high spatial-resolving power of most super-resolution microscopes is achieved by sacrificing temporal resolution, thus limiting such techniques to time scales of seconds to minutes. This limits its application in single-molecule studies with fast reactions and dynamics. Secondly, the algorithm used to process the image might lead to the possible false interpretation of single-molecule interactions.

Magnetic tweezers:

Magnetic tweezers utilize magnetic beads that respond to an external magnetic field to manipulate single molecules such as DNA.[89-91] For example, to investigate single DNA

molecules, the molecules are usually functionalized to have one end bonding to the substrate after surface passivation, and the other end attached to a magnetic bead. In such a way, the magnetic force applied on the magnetic bead acts to lift up the bead from the substrate surface stretching the single DNA molecule to different lengths depending on whether the DNA is a duplex or single stranded. The stretched DNA can then interact with different proteins leading to length changes owing to duplication, exonuclease activities, etc. Functional consequences of the protein-DNA interactions are then inferred from changes in the DNA length. The precision of the magnetic tweezers can be several base-pairs with relatively high throughputs (~1000 beads). However, this technique has limited versatility because any interactions that do not alter the length of DNA can not be studied using this technique.

Optical tweezers:

Optical tweezers have been applied to single-molecule studies because of their capability to manipulate small particles with high precision. [36, 92, 93] This technology utilizes a similar concept as magnetic tweezers, with the added advantage that with dual-trap optical tweezers there is no need to attach one end of the molecule to the substrate. [94] Each end of the molecule of interest is linked to a bead that can be precisely controlled by lasers. The biochemical process is usually observed using a fluorescent reporter. Despite its utility, the laser-generated heat prevents the optical tweezers from being used with sensitive substrates. In addition, undesirable energy transfer to the fluorescent dyes may result, causing photobleaching or blinking signals even before the experiment starts. Moreover, optical tweezers are limited in their ability to achieve high throughput.

DNA curtains:

The application of DNA curtains is another promising technique developed to observe single-molecule interactions. [95-98] Nanofabricated walls, posts, and grooves are used as barriers to stop DNA molecules sliding on a lipid surface. Under the hydrodynamic force in a fluidic environment, those anchored DNA molecules will be stretched out and form a curtain along the nano-walls or nano-grooves. Molecular-level interactions then can be observed in parallel from DNA curtains and much additional information can also be extracted at the same time. Although a DNA curtain is a powerful platform for some single-molecule experiments, the disturbance from the fluidic environment reduces the detection sensitivity. In addition, this technique may not be applied to single-molecule studies that do not involve DNAs.

Nanopores and nanochannels:

Nanopores can be described as a miniaturized chip version of a “Coulter counter”. [99-102] A signal is observed when biomolecules are electrophoretically driven through a nanoscopic pore deposited on a membrane that separates two electrolyte filled chambers and briefly blocks the ionic current. Resistive-pulse measurement across the nanopore yields characteristic modulation of an ionic current (e.g., amplitude and duration of the current block) that is related to the properties of the molecule present in the nanopore at a given time. Solid-state nanopores deliver the advantages of low cost, exceptional durability, precise tuning of the size and structure, and ease in fabricating high-density nanopore arrays. These synthetic nanopores are rapidly becoming a promising alternative to their biological counterparts. Although single-nucleotide discrimination has not been achieved using solid-state nanopores, with advances in nanofabrication the list of biomolecules that can be sensed by solid-state nanopores has

successfully expanded to include short nucleic acids of some ten base pairs. The nanopore-based techniques measuring the electric signals for single-molecule detections are usually conducted on single-nanopore basis, causing relative low throughput that hinders the applications of this technique for large quantity data acquisition and analysis.

Nanoaperture-based sensors:

Conventional nanoaperture-based sensors such as zero-mode waveguides (ZMW) are emerging tool for parallel single-molecule detections through fluorescence detections. [103-110] These sensors reduce background for single-molecule detections in a high concentration solution, utilize confined local field cut-off by the nanoapertures to excite single-molecule fluorescence for detections. Nanoaperture-based sensor potentially can achieve very high throughput. However, as of today nanoaperture-based sensors have relatively low sensitivity and low signal-to-noise ratio, which are caused by low excitation energy and high background noise level.

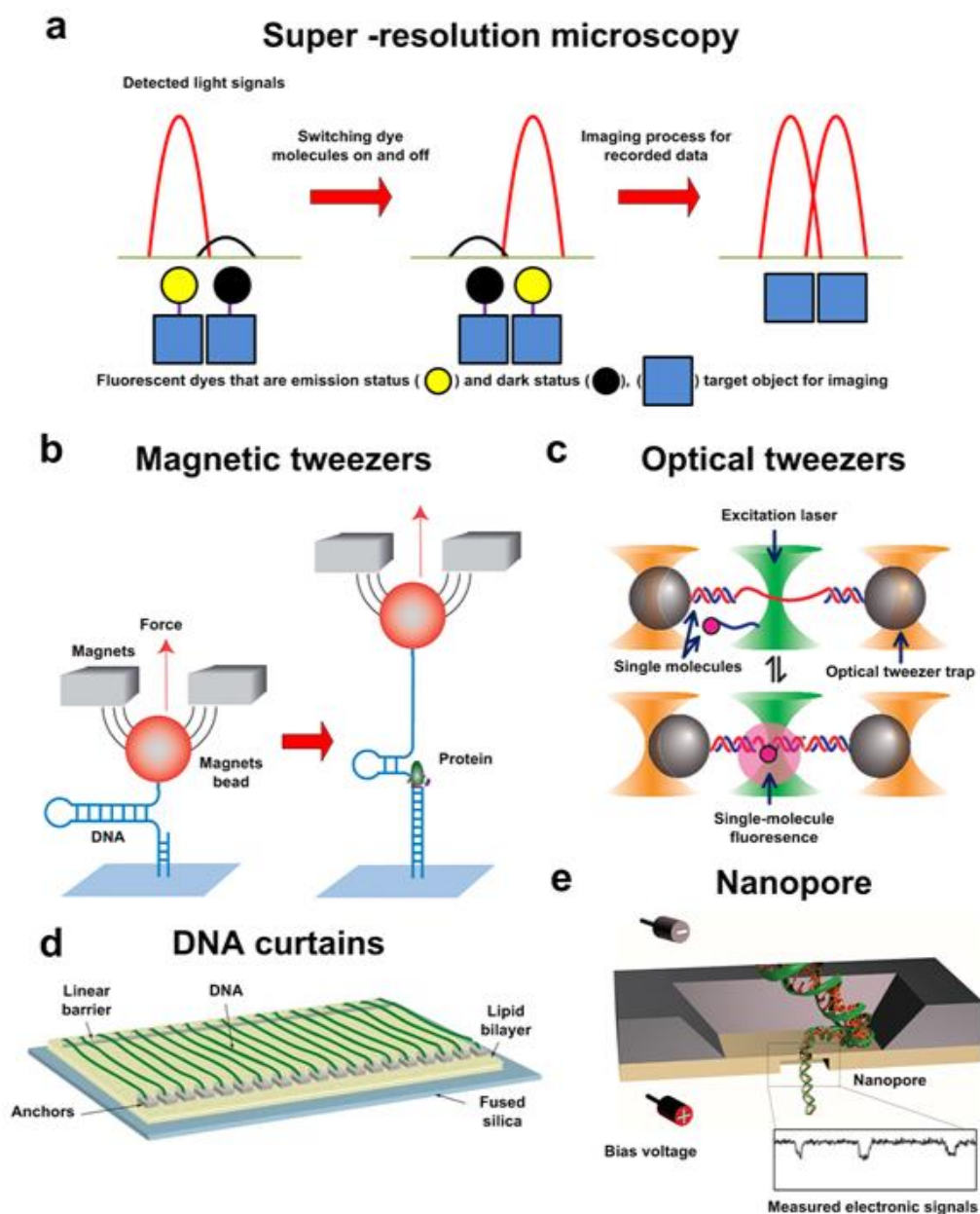


Figure 2-1. Different techniques for single-molecule studies. (a) the working mechanism of super resolution microscopies differentiating two adjacent biomolecules with fluorescence labels; (b) magnetic tweezers utilizing magnetic beads to stretch and extend DNA molecules; (c) dual-trap optical tweezers that can suspend DNA molecules in solutions, with addition interrogation laser studying single-molecule dynamics; (d) DNA curtains allows DNA molecules to be aligned and stretched under fluid flow for high-throughput single-molecule reactions, and (e) solid-state nanopores structure detecting electronic signals from single molecules passing through the nanopores. Images are adapted from Ref. [89, 94, 97, 101].

2.3. T4 DNA Replication Studies

DNA replication is the basis for biological inheritance. It is a fundamental process occurring in all living organisms and requires the complete genome to be copied before each cell division. Replisome mediated DNA replication in bacteriophage T4 requires the coordinated effort of eight proteins to efficiently and accurately replicate DNA on both the leading and lagging strands. Synthesis of the leading and lagging strand is a highly coordinated process and the specific mechanisms of the coordination between the two strands among different replisomes are yet to be validated through single-molecule techniques. Specifically, the protein-protein interactions of T4 system that await single-molecule dynamical characterization include: 1) the gp59 helicase loader and gp41 helicase pair that leads to proper assembly of the hexameric helicase complex, which unwinds the parental strands for duplication by the leading and lagging-strand polymerases; 2) the gp45 clamp and gp43 polymerase pair, the holoenzyme by which the T4 replisome obtains high processivity in replication; and 3) the gp61 primase and gp41 pair that forms primosome, the subassembly that lays down primer for iterative initiation of the lagging strand fragment syntheses and also serves to enable sufficient primase activity for lagging strand reinitiation. Solving those puzzles in T4 DNA replication will provide precise information on modeling the replisome interactions during the replication process, as well as valuable references understanding the human DNA systems.

2.4. Engineering Approach for Protein-Protein Interactions in T4 DNA Replisomes: Zero-Mode Waveguide (ZMW)/Microfluidics Hybrid Chip

The ability of nanofabricated zero-mode waveguides (ZMW) to guide light energy into subwavelength-diameter cylindrical nanoapertures has been exploited for single-molecule fluorescence studies of biomolecules at micromolar concentrations, the typical dissociation

constants for biomolecular interactions. Although epi-fluorescence microscopy is now adopted for ZMW-based imaging as an alternative to the commercialized ZMW imaging platform, its suitability and performance awaits rigorous examination. In this section, we present conical lens-based dark-field fluorescence microscopy, in combination with a ZMW/microfluidic chip, for single-molecule fluorescence imaging. It is demonstrated that compared to epi-illumination, the dark-field configuration displayed diminished background and noise and enhanced signal-to-noise ratios. This signal-to-noise ratio for imaging using the dark-field setup remains essentially unperturbed by the presence of a few micro-molar background fluorescent molecules. The novel nanophotonic design approach allowed single-molecule FRET studies on revealing weak DNA-protein and protein-protein interactions found with T4 replisomal proteins.

In this section, I will discuss my work on designing and testing a proof-of-concept ZMW/microfluidic hybrid chip as a prototype for an engineering nanophotonics enabled, ZMW-based, on-chip single-molecule imaging platform. This proof-of-concept ZMW/microfluidic hybrid design benefits single-molecule experiments from the following aspects: (1) Microfluidics help to reduce the sample consumption of reagents that are difficult to obtain, such as human proteins. It can effectively deliver such reagents precisely to where the experiment will be monitored and significantly reduce the sample consumption. (2) The microfluidic systems can precisely control the reaction fluids in terms of reaction amount, volume, time, etc. The microfluidic systems also help to ensure consistent reaction conditions for each experiment, increasing reproducibility for large quantities of data collection and analysis. (3) The microfluidic channels can effectively seal the reaction solutions inside the microfluidic channel, protecting and isolating the reactants and the reaction from the environment. (4) Using microfluidic systems, we are able to achieve numerous parallel reactions on one chip permitting automated high-throughput screening and analysis.

In addition to the ZMW/Microfluidic hybrid chip, we took a further step developing a conical lens-based dark-field fluorescence microscope tailored for ZMW illumination, and utilizing this illumination method to achieve high signal-to-noise ratio on single-molecule studies on the hybrid chip. Through side-by-side comparison with Epi, we found that the dark-field setup effectively decreased the background fluorescence and noise levels by alleviating the leakage of ZMW surface reflected illumination into the fluorescence detection module. In single-molecule photobleaching measurements with Al/ZMWs, the dark-field setup has an average signal-to-noise ratio (S/N) of 5.13 compared to 1.78 for the Epi setup. This substantial improvement in imaging performance permitted ZMW-based single-molecule FRET studies at micromolar background fluorophore concentrations without substantial deterioration of the S/N ratio. This in turn enabled real-time investigation of a weak single-stranded DNA (ssDNA)-protein interaction and a rare protein-protein interaction within the T4 replisome.

2.4.1. Nanofabricated Zero-Mode Waveguides (ZMWs) for Single Molecule Studies

Zero-Mode Waveguide (ZMW) is an attractive platform for single-molecule imaging due to the high parallelism and most importantly, to its tolerance of high concentrations of fluorescent species.[111-114] ZMWs, the subwavelength-diameter cylindrical nanoapertures clad in metal (e.g., aluminum) (Fig. 2-2a), guide the incident excitation beam in a non-propagating “zero mode” to form an evanescent excitation field at the entrance of the cylinder with a typical observation volume of ~zeptoliter (10^{-21} L) (Fig. 2-2(b)), a volume ~3 orders of magnitude smaller than that in diffraction-limited microscopy. Due to this superior optical confinement property, single-molecule fluorescence imaging using a ZMW allows for the detection of single excited fluorescently labeled biomolecules in spite of the presence of up to 10 μ M out-of-focus background fluorescent species.

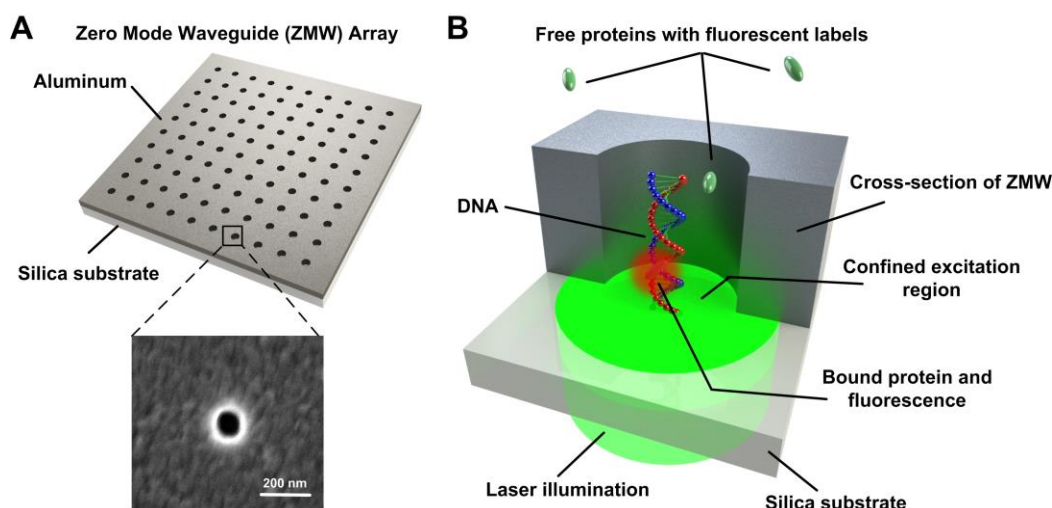


Figure 2-2. (a) Schematic of zero-mode waveguide (ZMW) array. The typical ZMWs are subwavelength-diameter cylindrical nanowells in ~ 100 nm-thick aluminum coated on top of a silica substrate. The magnified square region shows the SEM image of the 90 nm-diameter ZMW used throughout this study. (b) The optical confinement property of ZMW for single-molecule fluorescence studies. As light (i.e., 532 nm green laser) penetrates into a 50- to 100- nm-diameter ZMW from the silica side, its intensity exponentially attenuates to generate an evanescent excitation field of \sim zeptoliters (10^{-21} L). This optical property allows for single-molecule fluorescence studies of biomolecular interactions (i.e., interactions between ZMW-immobilized DNA and a DNA-interacting protein in bulk solution) to be carried out in ZMWs at micromolar (μ M) bulk concentrations of fluorescent biomolecules.

Since its inception, this nanostructure has found ample utility in single-molecule investigations of a growing list of biological targets.[102, 115-120] The accessibility of a ZMW-based single-molecule fluorescence platform, however, remains limited to a handful of specialized laboratories, due to the stringent technical requirements in nanofabrication, surface passivation, and microscopy instrumentation.[121, 122] Although these constraints have recently been relieved somewhat as more efforts have been directed to the optimization of ZMW nanofabrication protocols and the development of surface passivation methods, the simplification of a single-molecule fluorescence microscopy setup for ZMWs and the optimization of its performance have remained challenging. Holographic confocal fluorescence microscopy, in which sophisticated optics are employed in complex light paths to generate thousands of sub-

illumination spots and corresponding prism-dispersed emission spots that match the pattern of ZMW arrays, was originally developed for ZMW-based single-molecule imaging.[123] The level of complexity and the costly investment of this microscopy setup are not amenable to its widespread implementation, despite its superior performance. Alternatively, epi-fluorescence microscopy (Epi) was implemented in ZMW-based fluorescence imaging;[115] however, this microscopy setup is not tailored for illuminating ZMWs and the performance of Epi to image single fluorophores residing in the highly reflective aluminum clad ZMWs (Al/ZMWs) has not been rigorously investigated. In short, a simple, optimized microscope setup would facilitate the generalization of the ZMW-based single-molecule imaging technique.

The accessibility of a high-performance, single-molecule fluorescence microscope for ZMW-based imaging has constrained the widespread implementation of this technology in biological studies. On one hand, dissemination of this method has been hampered by the complexity and high cost associated with the multiplexed confocal microscopy designed for ZMW in which a collimated laser beam is holographically split into thousands of sub-beams, each one designated to a specific ZMW. On the other hand, an alternative Epi setup was employed for illuminating the highly reflective Al/ZMWs, which taxed the efficiency of conventional Epi to filter the potentially strong reflected excitation beam from the fluorescence signal.

2.4.2. Zero-mode Waveguide Fabrication and Characterization

Zero-Mode waveguides (ZMWs) used in this study were fabricated by electron beam (E-beam) lithography (Vistec EBPG5200). The base samples for E-beam lithography were prepared through high vacuum deposition (Semicore) of a 100 nm thick aluminum layer on top of 25 x 25

mm² silica glass coverslips and then spin-coating (4000 rpm for 45 s) a ~ 350 nm thick positive E-beam photoresist (ZEP-520A, ZEON Corporation) layer on top of the aluminum layer.

The pattern of the ZMW arrays was designed using L-Edit and exported as a .gds file. The file was then converted using Layout Beamer to a system-recognizable pattern. The E-beam used to transfer the pattern of the ZMW arrays to the photoresist layer of the base sample worked under a 400 μ m aperture and had an electron current of 1 nA, resulting in a sufficient spatial resolution of 13 nm for ZMWs with diameters of 50 to 100 nm. The markers for polydimethylsiloxane (PDMS) microfluidic channel alignment were fabricated using a 200 nA current E-beam. The optimized E-beam lithography doses for writing the ZMW pattern and markers were obtained through dose array tests. E-beam lithography was conducted in a vacuum environment of 10⁻⁶ Torr. Depending on the sample designs, the E-beam exposure time usually took from 15 to 20 mins for one sample fabrication. The E-beam exposed photoresist was developed in n-amyl acetate for 3 mins, and then rinsed using 2-propanol for 1 min.

After being dried with nitrogen, the samples were dry-etched in a reactive-ion etcher (Plasma-ThermVersalock 700 ICP) with a mixture of chlorine (Cl₂), boron trichloride (BCl₃), and argon (Ar). The exposed aluminum layer was etched to form the programmed ZMW arrays, while the remaining unexposed photoresist acted as a protection mask for the aluminum underneath. The photoresist mask would easily sustain the etching time of 90 s, resulting in a successful ZMW pattern transfer to the aluminum film with little over-etching into the silica glass substrate. After the etching, the samples were immediately immersed into deionized water to wash away any residual chlorine, which is corrosive to aluminum in a moist environment. E-beam photoresist remover (Microposit remover 1165, Shipley Company) was then used to remove the photoresist residue on top of the aluminum ZMW samples.

The ZMW samples were then characterized using a scanning electron microscope (Leo 1530 FESEM) and optical microscope (TE2000-U, Nikon). The SEM images (Fig. 2-3) showed

the dimensions and uniformity of the ZMW wells fabricated on both E-beam photoresist and aluminum film. The optical image captured from the microscope in a transmission mode (Figure 2-4(d)) indicated that the ZMW wells were etched through the aluminum film.

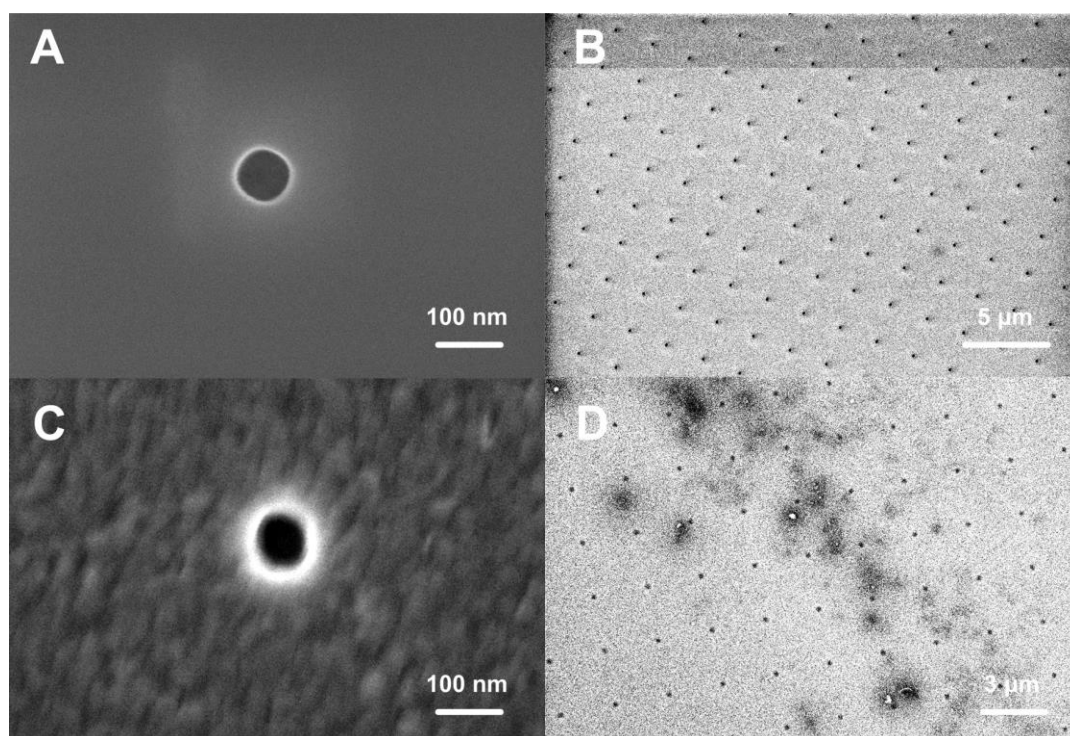


Figure 2-3. SEM images of (a) a representative ZMW structure (90 nm in diameter) and (b) a ZMW array after developing the E-beam exposed photoresist are shown. SEM images of (c) a ZMW and (d) its array after dry etching and removal of residual photoresist are shown.

2.4.3. Conical Lens-based Dark-Field Illumination on a ZMW/Microfluidic Hybrid Chip

The working mode of a ZMW demands that both the incident illumination laser and the signal collection be carried out from the coverslip side of ZMW arrays through an objective lens causing the reflected incident laser light to overlap with the weak back-scattering fluorescent signals. To avoid signal deterioration, a proper dichroic filter is often installed in conventional microscopy to selectively collect the fluorescent emissions and block the unwanted reflected excitation beam. When Al/ZMWs are illuminated in the Epi mode, the strong reflected

illumination beam caused by the smooth, highly reflective Al film surface imposes high demands on the dichroic filter for complete reflection blocking. Unlike the Epi configuration, a multiplexed confocal microscope sidesteps the interference from the reflected excitation beam by generating a patterned illumination composed of numerous split beams that pinpoint the silica bottom of the ZMWs. [123] However, this confocal microscope arrangement is technically challenging to implement.

We have attempted to address the issues with a simple yet effective conical lens-based dark-field fluorescence microscope. Commercially available dark-field microscopes that work either by a transmission mode, as in the case of an inverted dark-field microscope, or rely on specially designed objective lenses, as in the case of an up-right dark-field microscope, are incompatible with the reflection mode required by ZMW imaging. The detailed optical setup is shown in Fig. 2-4(a). The three lasers (488 nm, 532 nm, and 633 nm) aligned and superimposed by beam splitters, BS1 (645dxcr, Chroma) and BS2 (488rdc, Chroma), were converted by a conical lens (160 degree in conical angle) (Chroma) from a Gaussian circular illumination beam to a doughnut-shaped ring beam. This ring beam was then collected and focused by a lens group before it was coupled into an inverted microscope (Nikon TE2000-U) through a dichromic mirror (T560LPXR, 532 nm/633 nm for 532 nm and 635 nm lasers or HQ500LP for 488 nm laser, Chroma) and focused onto the back focal plane of the objective lens (Plan APO VC, water immersion, NA 1.2, 60X, Nikon). The output beam from the objective lens maintained its ring pattern and exhibited angled illuminations on the bottom sample interface between the ZMW patterns and fused silica substrate. Any reflections from the incident beam following Snell's law would be directed along the optical path without overlapping the fluorescence emission collected from the center of the objective lens, pass through the dichromic mirror and enter into the detection module. The detection of single-molecule fluorescence was performed with an electron multiplied charge coupled device (EMCCD). The EMCCD was configured into a dual-channel

detection mode enabling concurrent observations of both Cy3 and Cy5 fluorescence at the same time with precise spatial correlations when both the 532 nm and 635 nm lasers were in operation. Beam splitters, BS3 (HQ535/50M, Chroma) and BS4 (HQ610/75M, Chroma), and mirror groups separate the collected fluorescent signals spatially, and align them parallel towards the target detection region of the EMCCD.

The instrument has a customized optical path where the light from its three lasers is first superimposed by two beam splitters (BS1 and BS2) and then rendered by a conical lens (CL) and lenses L1 and L2 to a “doughnut” like beam with zero intensity at the center and maxima at the rim (Fig. 2-3(c)). This light pattern is then tuned by lenses L3 and L4 to focus at the back focal plane of the 60 X objective to illuminate the ZMW array. Our proposed design addresses the reflection issue in AI/ZMW imaging because it separates the back-scattering fluorescence signal from the reflected, incident light. Given that the doughnut-shaped beam impinges on the ZMWs with a large incident angle through the 60X objective ($NA = 1.2$), any reflection from the metal interface would either escape by the same illumination pathway or be cut off by the aperture of the objective, thereby reducing any reflection that leaks into the center region of the objective lens. This then essentially separates the optical path of the desired fluorescence signal from that of the incident and reflected beams as the fluorescent signal (orange arrow, Fig. 2-4(a)), collected by the objective lens, localizes in the center region that is largely orthogonal to both the incident and reflected excitation located at the peripheral doughnut rim (dot line, Fig. 2-4(a)).

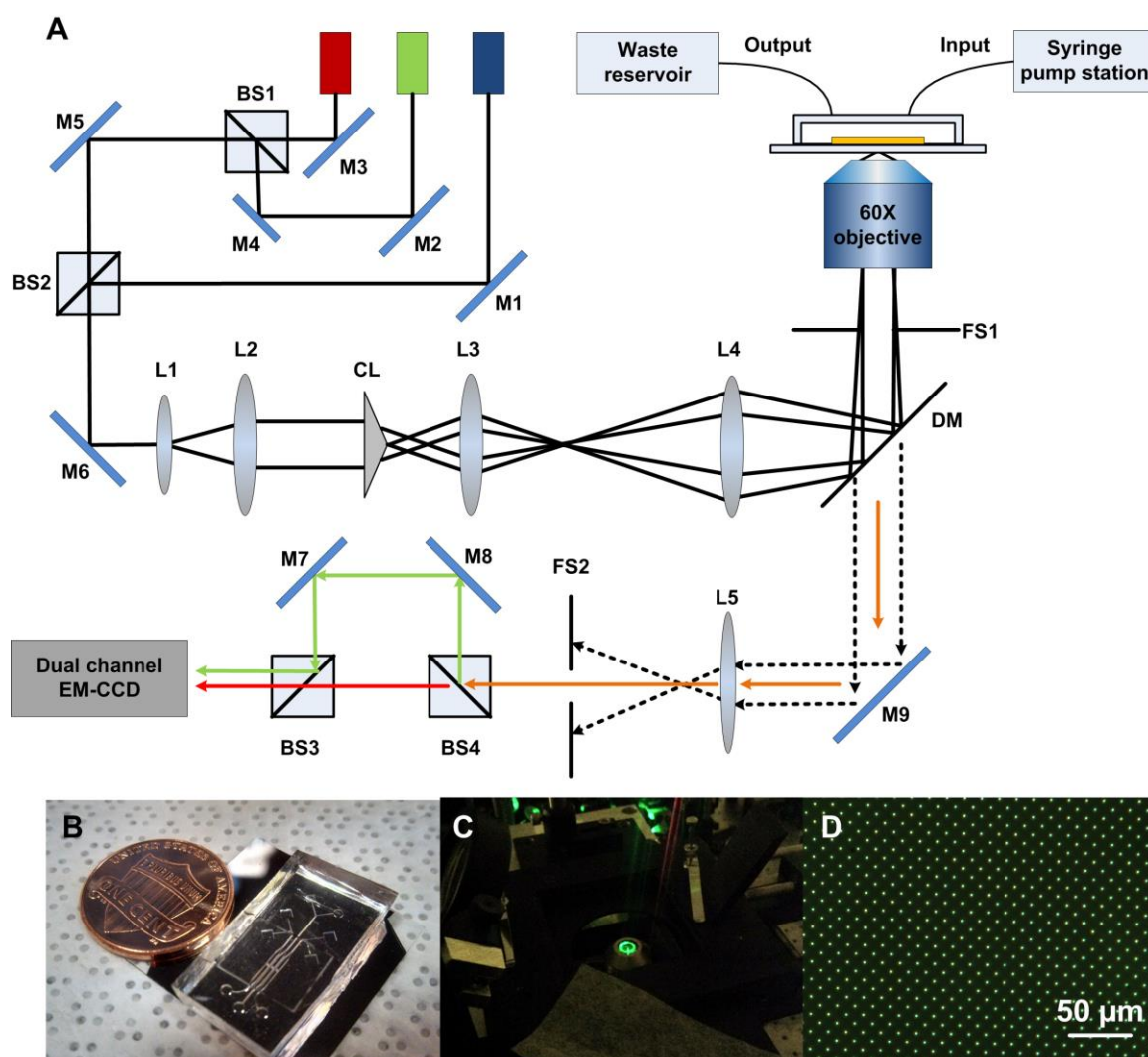


Figure 2-4. Conical lens-based dark-field microscopy in combination with ZMW/microfluidic chip for single-molecule imaging. (a) The microscope setup was built on an inverted microscope. The 532 nm (Green), 635 nm (Red), and 488 nm (Blue) lasers were superimposed by mirrors (M1-M6) and beam splitters (BS1, BS2). The merged beams were then expanded by lenses (L1 and L2) and rendered into a doughnut shape by a conical lens (CL). Lenses L3 and L4, together with a dichromatic mirror (DM) and a field stopper (FS1), directed the beams to focus at the back focal point of a water-immersion 60X objective. Placed on top of the objective, the ZMW/microfluidic channel connected with a syringe pump acted as a sealed reaction chamber. Fluorescence emission signals (Orange arrow) from Cy3 and Cy5 dyes collected through the objective were split by BS3, BS4, M6, and M7 for the dual-channel EMCCD detection. Any peripheral reflected excitation beams (dotted line), which leaked into the detection module, were removed by FS2. (b) ZMW/microfluidic chip for single-molecule fluorescence measurements, (c) the doughnut-shape illumination beam (532 nm) rendered by the dark-field illumination configuration, and (d) optical image of a ZMW array.

We have also demonstrated an integration of ZMWs with a microfluidic system (Fig. 2-4(b)) to take advantage of the high-precision fluidic control enabled by microfluidic techniques.[124-126] Mounted on the microscope stage, a coverslip with a 90 nm-diameter ZMW array (Fig. 2-4(d)) was integrated with a polydimethylsiloxane (PDMS) microfluidic channel and a syringe pump system to form a ZMW/microfluidic chip (Fig. 2-4(b)) as a reaction chamber for single-molecule fluorescence imaging.

The PDMS microfluidic device fabrication followed the standard procedure for soft-lithography. The mask for a PDMS microfluidic channel was designed using CAD software L-Edit or AutoCAD. A silicon wafer patterned with the mask design by photoresist was etched by deep reactive ion etching to generate the silicon master mold for PDMS casting. After the silicon mold was cleaned and coated with 1H, 1H, 2H, 2H-perfluorooctyltrichlorosilane (Sigma-Aldrich), the Sylgard 184 Silicone Elastomer base and curing agent (Dow Corning, Midland, MI) were mixed in a 10:1 weight ratio and poured onto the pretreated silicon master mold. After curing at 70 °C for 20 min, the PDMS imprinted microfluidic channels with dimensions of 10 mm x 2 mm x 0.2 mm were peeled from the silicon mold and perforated by mechanical punching to form microchannels with inlets and outlets. The PDMS microfluidic channel and ZMW substrate were treated with oxygen plasma and bonded to form a sealed ZMW/Microfluidic chip.

The precise, uniform dimensions (10 mm x 2 mm x 0.2 mm) of the microfluidic channels not only require very small volumes of the reaction mixture (~4 μ L), but they also permit deploying multiple microchannels in a 25 x 25 mm² area with ZMWs for parallel reactions. Equipped with a syringe pump system, the ZMW/microfluidic chip was functionalized/passivated by sequentially injecting one at a time anti-digoxigenin antibody (Anti-Dig), BSA, 5'-Dig-ssDNA primer labeled with Cy3, and dye-labeled fluorescent molecules with washes between each injection in a programmable fashion. In addition, the PDMS microfluidic molding served to seal the ZMW reactors helping to maintain the pH value of the reaction mixture by isolating the acid-

producing anti-photobleaching oxygen scavenger system from ambient oxygen. A prototype of the integration of a microfluidic chip and a ZMW single-molecule detection platform is shown in Fig. 2-5(a). All of our experiments discussed in this section are conducted using this lab-on-a-chip platform.

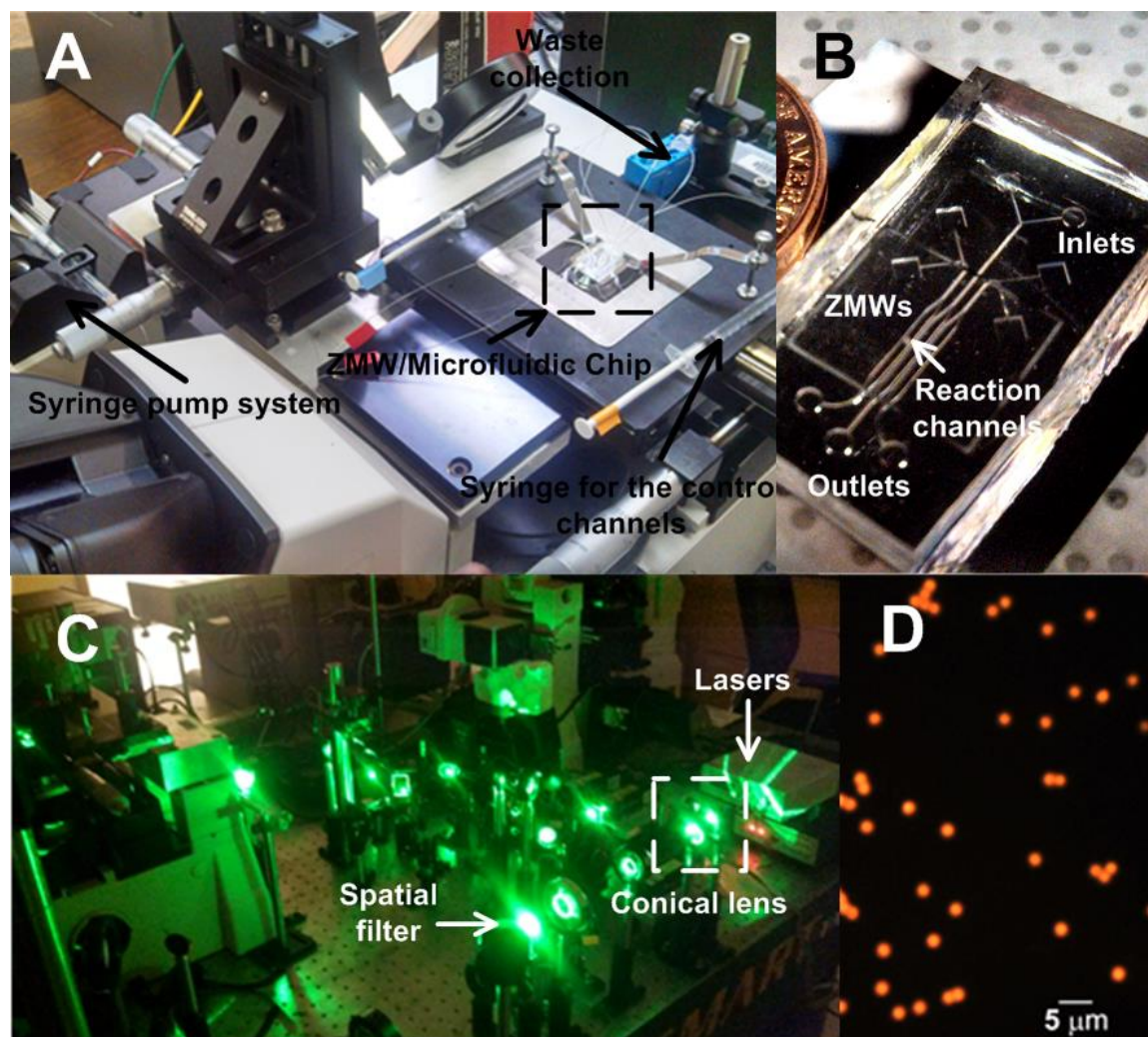


Figure 2-5. (a) Detailed view of our setup conducting single-molecule experiment using ZMW/microfluidic hybrid chip. (b) A microfluidic channel design that enables three single-molecule experiments running in parallel at the same time. (c) Our customized optical path for dark-field illumination of ZMW. The dark field image of the 2.8 μm -diameter magnetic beads captured using our system for calibration is shown in (d).

2.4.4. Background Noise Levels and Fluorescence of Epi and Dark-Field Fluorescence Microscope

To evaluate the collection of the reflected incident excitation beam by Al/ZMW arrays in the conventional Epi and the conical lens-based dark-field microscope setups, we measured the background fluorescence and noise levels of the two setups using the three different colored lasers (488, 532, and 635 nm) to illuminate the Al/ZMW chip without any fluorescent molecule present. The incident lasers were set at 50% power output (measured ~165 mW) with a proper dichroic filter installed for each laser to block the reflected excitation beam. As shown in the color-coded EMCCD images of ZMWs illuminated by the three lasers individually (Fig. 2-6 (a-c)), the background fluorescence of the Epi setup was substantially stronger than that of the dark-field setup, most likely caused by the leakage of the strong reflected excitation beam despite the installation of the dichroic filter in the Epi setup. From representative time-resolved fluorescence traces for the fluorescence in the Cy3-detection channel of ZMWs illuminated with the green (532 nm) laser in both configurations (Fig. 2-6(d)), we found that the background fluorescence levels (mean values, 1039 vs 363 in arbitrary units, AU), as well as the fluctuation of the background fluorescence levels defined as noise (832 vs 312 in AU) were substantially higher in the case of the Epi setup (Fig. 2-6(e)). The distribution histograms of the background fluorescence levels based on the statistics of 250 traces obtained from both setups (Fig. 2-6(f)) consistently showed that the dark-field setup has a lower average value (376 AU) than the Epi setup (853 AU) and a much narrower distribution of the background fluorescence fluctuations also.

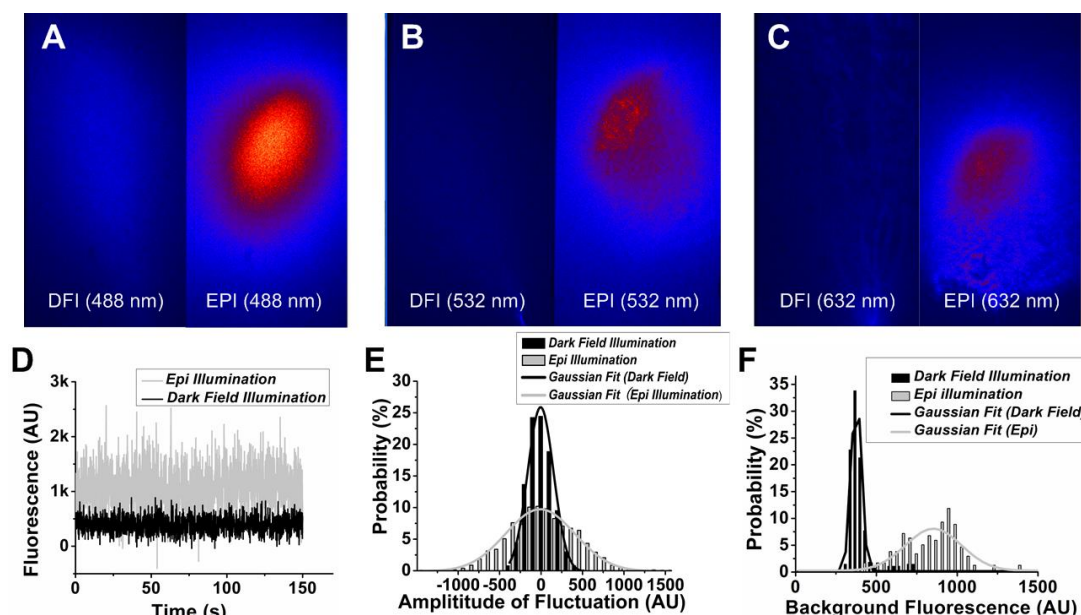


Figure 2-6. EMCCD images of the background fluorescence in emission detection channels for (a) Cy2, (b) Cy3, and (c) Cy5 for ZMWs in dark field (DFI, Left panel) and Epi (EPI, Right panel) configurations illuminated by the blue (488 nm), green (532 nm), and red (635 nm) lasers, respectively. The ZMWs were free of fluorescent molecules. The fluorescence intensity in the image was color-coded according to the spectral gradient from blue (intensity minimum) to red (intensity maximum). (d) A representative time trace for the background fluorescence in the Cy3 detection channel of ZMWs in Epi (Gray) and dark field (Black) configurations illuminated with the green (532 nm) laser. (e) Fluctuations of the background fluorescence of a representative time trace. The histograms were plotted using the data in (d) and were fit to a Gaussian function to give standard deviations for the noise level of 832 AU for Epi and 312 AU for dark-field. AU: arbitrary units. (f) Distribution of the background fluorescence intensity in the Cy3 detection channel of ZMWs in Epi (Gray) and dark-field (Black) configurations illuminated with the green (532 nm) laser. The mean background values from 250 fluorescence traces from either illumination configuration were plotted in histograms, which were fit to a Gaussian function to give the median background fluorescence levels of 853 ± 417 AU for Epi and 376 ± 61 AU for dark-field.

2.4.5. Single-Molecule Photobleaching Measurements with ZMWs in the Presence/Absence of Fluorophores in Bulk

It has been shown that the conical lens-based dark-field microscope suppresses the background fluorescence and noise levels as a result of the reduced collection of reflected excitation beam by the Al/ZMWs surface. We next set out to examine the impact of the reflected

excitation beams on the performance of the dark-field and Epi setups in single-molecule fluorescence measurements with ZMW arrays using S/N from Cy3 as the criterion.

Before the experiment, the surface passivation of the ZMW/microfluidic chip is conducted following the procedures below. The surface of the ZMW/microfluidic chip was treated with 5 nM anti-digoxigenin (anti-Dig) antibody (Roche) in Buffer A [20 mM Tris (pH 7.5) with 150 mM NaCl] for 1 hour to allow the antibody to bind nonspecifically on ZMW surface. The remaining bare surface was passivated by treating the chip with 30 μ M bovine saline albumin (BSA) (Calbiochem) in Buffer A for 1.5 hours. Finally, 4 nM single-stranded DNA primer of 40 nt [5'-ATG ATT GAG GTA GGA GTA GTT(Cy5) GAT GGA GAG AAG GTG AAT G-Dig-3'] (Integrated DNA Technologies) was incubated for 15 min. Following this treatment, ~40% of the ZMW nanoapertures had a single copy of the primer attached within the evanescent excitation field. The chip was flushed with Buffer A between steps to remove unbound materials.

Single-molecule fluorescence measurements were performed on a home-built Epi or dark-field microscope based on a TE2000U microscope (Nikon). Fluorescence emissions from Cy3 and Cy5 dyes were collected through a Plan Apo 60x 1.2 NA water immersion objective (Nikon) after filtering out other wavelengths using a dual-band TIRF filter cube (Chroma). An EMCCD camera was used to detect fluorescence emissions at an exposure time of 50 ms. A threshold intensity value was set to allow recognition of fluorescent spots in the image file whose spatial distribution matched with the corresponding pattern of the ZMW arrays.

In the single-molecule photobleaching assays, a signal was defined as the difference in fluorescence intensity before and after a single-step photobleaching event. Gaussian fitting of the residual fluorescent intensity after the photobleaching step yielded the median value that was defined as the background, and the standard deviation as the noise. The signal-to-noise (S/N) ratio

in photobleaching assays was calculated by dividing the signal by the noise. The apparent FRET efficiency (E_{FRET}) was calculated by using the following equation.

$$E_{\text{FRET}} = I_A / (I_A + I_D)$$

where I_D and I_A are the emission intensities of the donor (Cy3) and acceptor (Cy5), respectively

After the surface passivation, we firstly studied single-molecule fluorescence bleaching of Dig- and Cy3-labeled DNA primers immobilized in ZMWs. The 532 nm laser in either the Epi or dark-field mode excited the tethered primers until completely photobleached. The laser power was measured ~50 mW (measured at the objective) for all measurements. Noting that the power density calculated from measured illumination intensity over the illumination region may be different for each case, depending on the focusing condition and region; however, it is not a critical factor as the intensity is strong enough for fluorophore excitation in each experiment. The S/N ratio improvement has been achieved through splitting fluorescence and directing reflections away from our dark-field detection path. The Cy3 detection channel of the EMCCD-recorded images were used to identify individual emitters and analyzed to generate time-resolved single-molecule fluorescence traces. As shown in Fig. 2-7(a), the first recorded color-coded EMCCD images of the Cy3 primers excited by Epi gave an overall blurred image of the ZMW array pattern due to the significantly higher background fluorescence. Accordingly, numerous false emitters, in addition to the ones residing in ZMWs, were recognized and lead to uninformative time traces. In marked contrast, the image from the dark-field setup displayed suppressed background fluorescence and a clear view of ZMW array containing excited Cy3 primers, which were identified as individual fluorophores with little or no false positives.

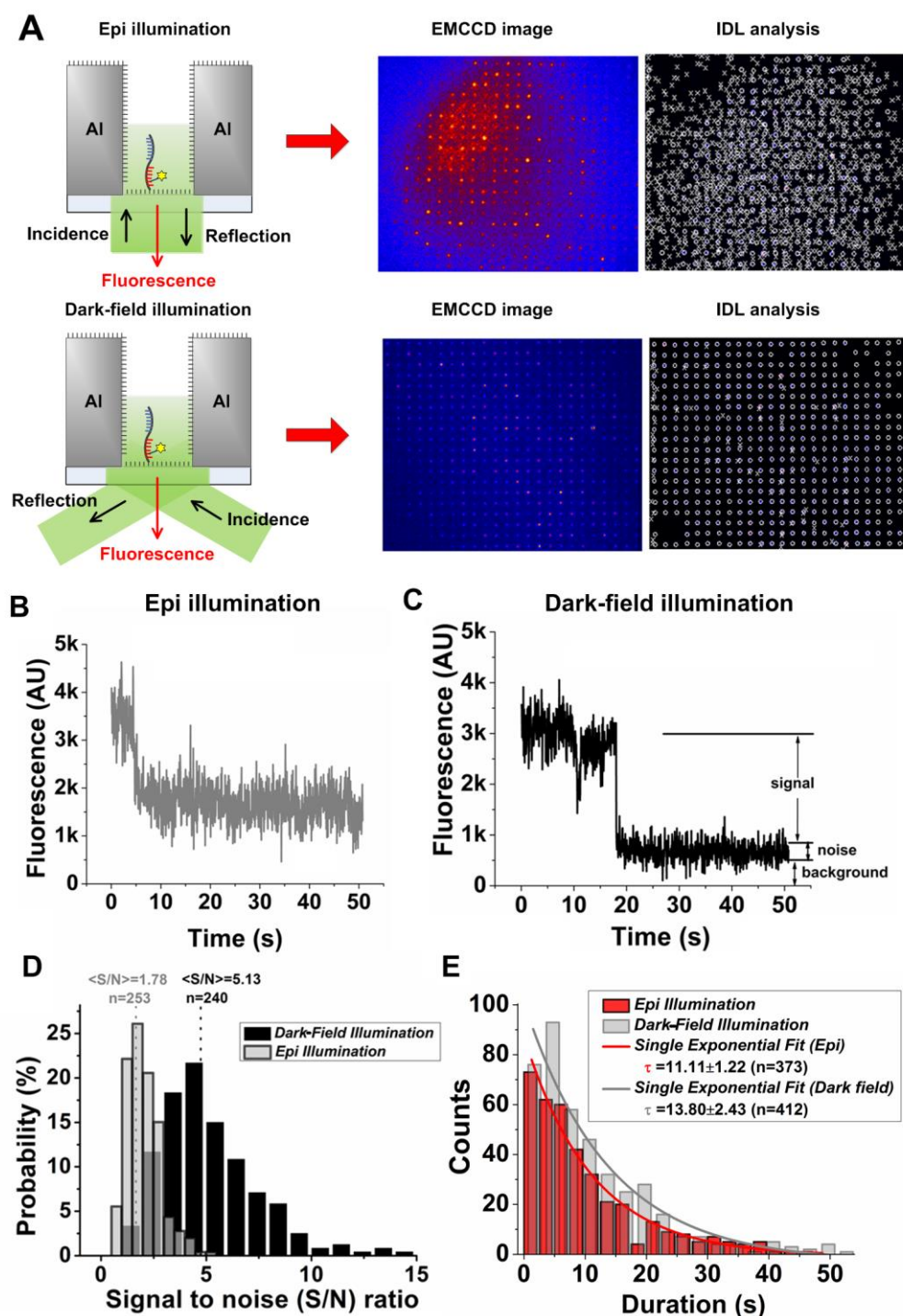


Figure 2-7. (a) Schematic of single-molecule photobleaching of the immobilized Cy3-DNA primer in a ZMW using the green (532 nm) laser in either the Epi or dark-field microscopy configurations. ZMWs were functionalized with anti-digoxigenin antibody and then passivated with BSA. A Cy3-DNA primer was immobilized through a digoxigenin: anti-digoxigenin antibody interaction. EMCCD images and IDL analysis results of the Cy3-primers immobilized

in ZMW arrays excited by the 532 nm laser in the Epi or dark-field configuration are shown. Fluorescence intensity was color-coded according to the spectral gradient from blue (intensity minimum) to red (intensity maximum). AU indicates arbitrary units. Representative single-step photobleaching trajectories of the Cy3-DNA primer excited by the 532 nm green laser in the (b) Epi and (c) dark-field configurations. (d) Distribution of the signal-to-noise ratio (S/N) in the single-molecule photobleaching measurements using the Epi (Gray) and the dark-field configurations (Black). Histograms were plotted using the S/N values from 240 (Epi) and 253 (dark-field) photobleaching events. The mean S/N ratios for the Epi and dark-field microscopies were 1.78 and 5.13, respectively. (e) Distribution of the fluorescence duration of the immobilized Cy3-DNA primers in single-molecule photobleaching measurements using the Epi (Red) and dark-field (Gray) configurations. Single-exponential fitting yielded the fluorescence durations (τ) of 11.11 ± 1.22 s ($n = 373$) for the Epi and 13.80 ± 2.43 s ($n = 412$) for dark-field setup.

Fig. 2-7(b-c) show examples of time-resolved fluorescence traces with single-step photobleaching events from the Epi and dark-field setups, respectively. Consistent with the reduced background fluorescence and noise, and the high S/N ratio of the dark-field arrangement in general, this configuration had an overall higher S/N ratio (5.13) compared to Epi (1.78) averaged from the measured ratios of ~250 photobleaching events in both cases (Fig. 2-7(d)). In addition, the probability of a S/N ratio ≥ 3 , a criterion for unambiguous identification of single-molecule events in microscopy analysis,[127] was 85.3% for the dark-field setup and 22.4% for the Epi setup. To warrant these S/N ratio comparisons, we tested the excitation/bleaching of the immobilized Cy3 primers in ZMWs under the same excitation intensity and statistically analyzed the fluorescence duration of ~400 photobleaching events using both setups (Fig. 2-7(e)). Because of the near-linear relationship between fluorescence duration and excitation intensity, the comparable characteristic duration time (τ) obtained by single-exponential fitting of the distribution plots (11.11 s (Epi) vs 13.80 s (dark-field)) proved that in spite of the different illumination modes, the two microscope arrangements generated excitation fields in the ZMW arrays with essentially equivalent intensities.[128]

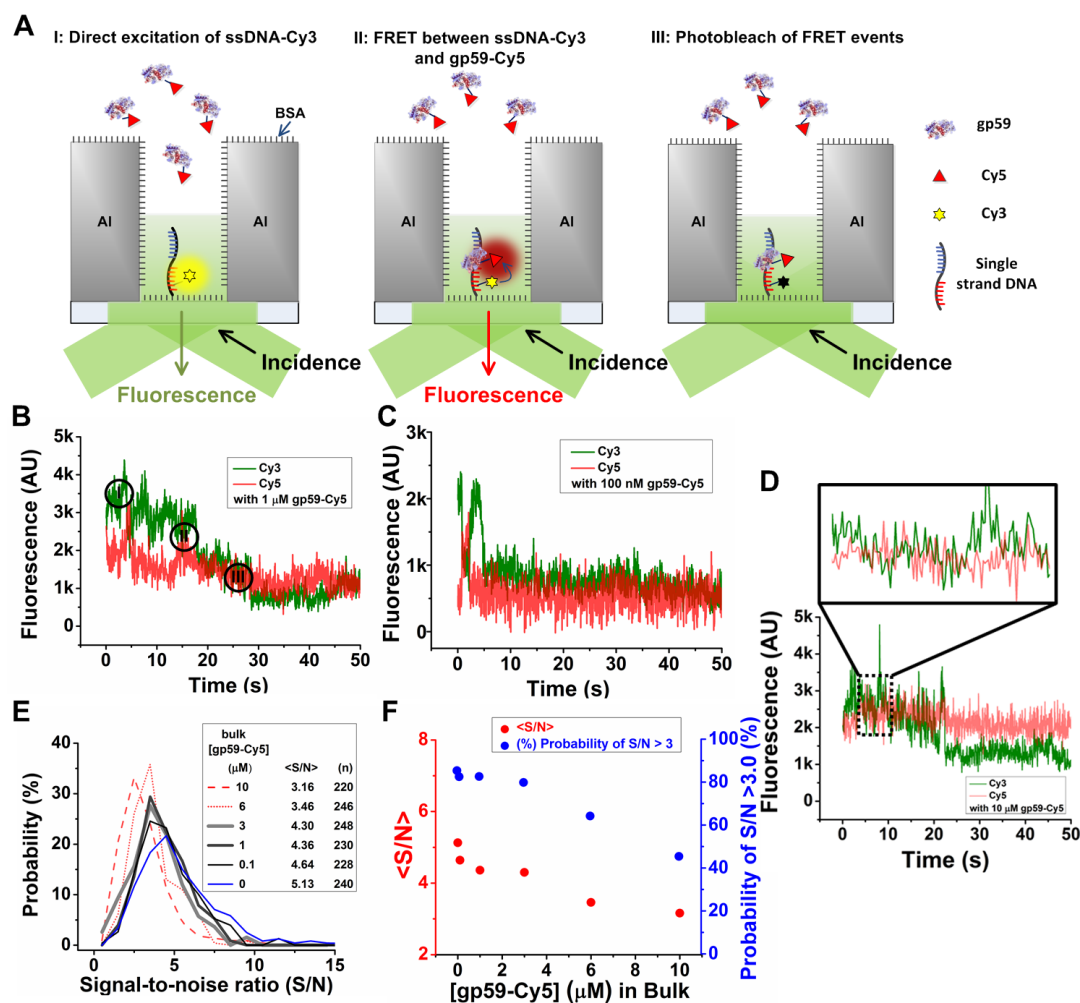


Figure 2-8. (a) Schematic of single-molecule photobleaching of the immobilized Cy3-DNA primer in ZMWs in the presence of bulk gp59(C42)-Cy5 excited by the green (532 nm) laser in the dark-field illumination configuration. Representative time traces of the single-molecule photobleaching of the Cy3-DNA primer in the presence of (b) 1 μ M, (c) 100 nM and (d) 10 μ M gp59(C42)-Cy5. The fluorescence intensities of the Cy3 and Cy5 channels are in green and red, respectively. (E) Distribution of the S/N ratio in the single-molecule photobleaching measurements of the Cy3-DNA primer in the presence of 0 nM (Blue), 100 nM (Black), 1 μ M (Dark gray), 3 μ M (Gray), 6 μ M (Red, dot line) and 10 μ M (Red, dash line) gp59(C42)-Cy5. (F) Mean S/N ratios ($\langle S/N \rangle$) and probability of S/N ratio larger than 3 as a function of gp59(C42)-Cy5 concentration.

ZMWs are known as nanostructures in which single-molecule imaging can be carried out in the presence of micromolar bulk fluorophores. To test whether the dark-field configuration was successful with ZMWs at high concentrations of bulk fluorophores, we determined S/N ratios

again in similar single-molecule photobleaching measurements, but in the presence of up to 10 μM Cy5-labeled gp59 (gp59(C42)-Cy5), the helicase loader protein in the T4 bacteriophage DNA replisome (Fig. 2-8(a)).[129-132] Because gp59 is known to bind to single-stranded DNA, the representative fluorescence time trace of tethered Cy3-DNA primer in ZMWs in the presence of 100 nM or 1 μM gp59(C42)-Cy5 displayed clear FRET events between the dyes on the DNA and gp59 before photobleaching of the Cy3 dye (Fig. 2-8(b-c)).[133] In the case of 10 μM bulk dye-labeled gp59, FRET events were less discernible in the representative time trace, owing to the increased level of cy5 emission (Fig. 2-8(d)). The occurrence of FRET events was dependent on the gp59 concentration. As shown in Fig. 5E, the overall S/N ratio distribution remained largely unperturbed by the presence of up to 3 μM of background gp59(C42)-Cy5. A noticeable shift of the distribution curve occurred at 6 μM gp59. The mean S/N ratio ($\langle\text{S/N}\rangle$) and probability of S/N larger or equal to 3 (% ($\text{S/N} \geq 3$)) remained constant at ~ 4.5 and 80% at less than 3 μM gp59. The deterioration of the two parameters was displayed when gp59 was greater than 6 μM . At 10 μM gp59, $\langle\text{S/N}\rangle$ decreased to 3.16 and % ($\text{S/N} \geq 3$) to 45%. In order to find out why the S/N ratio decreased as fluorophore concentration increased, we measured the background fluorescence level in the Cy3 emission channel for ZMWs with up to 8 μM bulk Cy3-labeled gp59. A ZMW chip, free of surface immobilized Cy3-fluorophores, was illuminated with the 532 nm laser. In good agreement with the above S/N changes, mean background fluorescence and the breadth of the distribution showed a substantial increase in the range of 4-6 μM bulk gp59 concentration. Thus, the decrease in S/N ratio at >6 μM bulk fluorophore originated from the deterioration of the background fluorescence. We attributed this to the increased non-specific binding of the protein on ZMW surface at higher concentrations and the relatively high focal volume of our dark-field setup. In light of these findings, we conclude that the conical lens-based dark-field microscopy achieve a substantial improvement in the S/N ratio in ZMW single-molecule imaging by alleviating the interference of the Al/ZMW surface-reflected excitation beam. Moreover, the

optimal background fluorophore concentration range of 0-4 μM is comparable to the previously reported range (up to 10 μM) of the commercialized ZMW imaging platform. These advantages, as well as the ease of implementation, make the dark-field microscope a more reliable alternative to the Epi setup, and a more implementable alternative to the commercialized one for ZMW-based imaging.

2.4.6. ZMW/Single-Molecule FRET between DNA-Protein and Protein-Protein Among the T4 Replisomal Proteins

The T4 DNA replication model system duplicates large DNA substrates at a rate of 400 bp/s by precisely orchestrating the complex interactions among the eight component proteins.[129, 134] This multi-protein complex has been a fertile ground for the practice of single-molecule fluorescence techniques, particularly single-molecule Fluorescence Resonance Energy Transfer (smFRET) by Total Internal Reflection Fluorescence Microscopy (TIRFM) for unveiling dynamic behaviors of the interacting proteins within the T4 replisome. [135-137] The concentration barrier of TIRFM, however, prevents single-molecule fluorescence studies on the T4 proteins at their physiological concentrations of sub-micromolar to micromolar. [137] We demonstrated here below that a conical lens-based dark-field microscope in combination with the ZMW/microfluidic chip is positioned to remove this obstacle in single-molecule dynamic studies on the T4 replisomes.

We focused on one of the T4 proteins, gp59. Known as the helicase loader, gp59 also plays additional roles in homologous recombination, DNA repair, and initiation of DNA replication. [137-140] Furthermore, it has remained elusive whether this protein acts as an integral component in the T4 replisome during DNA replication. We first studied smFRET between the immobilized Cy3-ssDNA primer in ZMWs and gp59(C42)-Cy5 in bulk. Previous

ensemble studies showed that gp59 binds to a short ssDNA weakly with sub-micromolar binding affinity in multiple proposed binding modes.[133] Using the ZMW/dark-field microscope, we carried out experiments with 1 μ M gp59 enabling single-molecule imaging at an adequate concentration for its interaction with the short ssDNA. We observed smFRET events and determined the FRET efficiency of each event (Fig. 2-9(a)). In addition, consistent with the proposed binding modes, we found that there were three main FRET states as indicated by populations with apparent FRET efficiencies of 0.37, 0.45, and 0.60 (Fig. 2-9(b-c)).

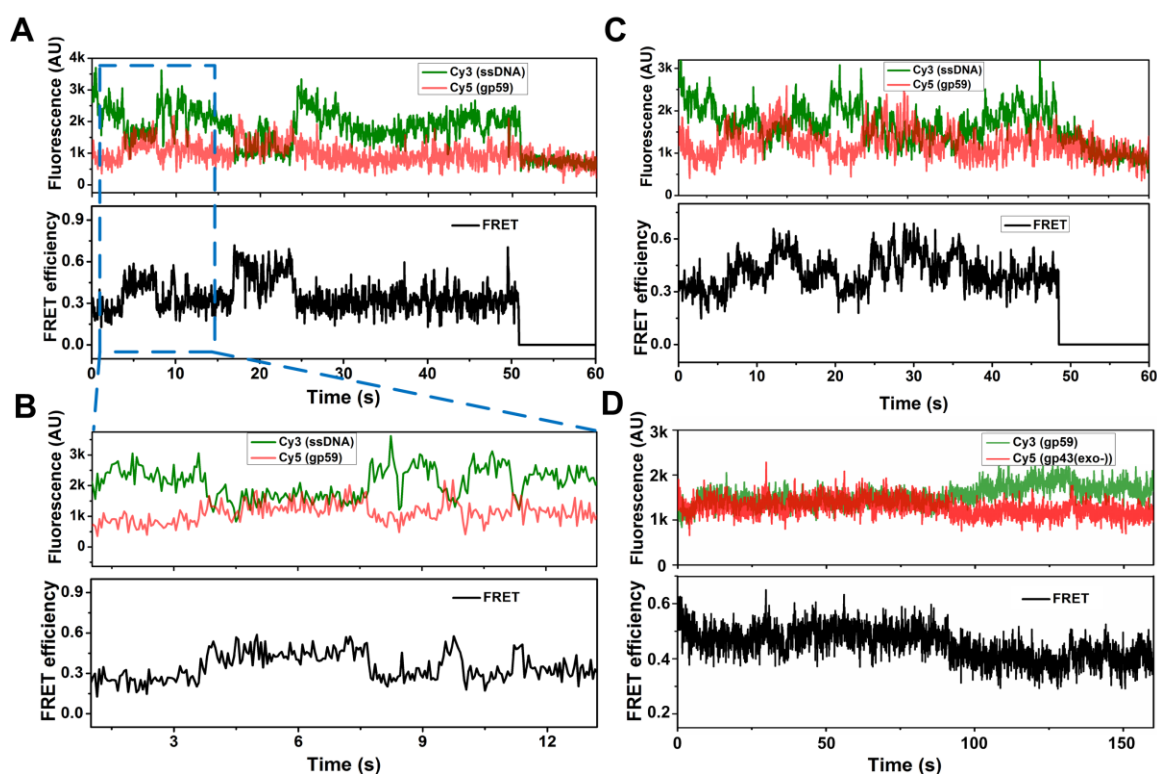


Figure 2-9. (a) Representative FRET and FRET efficiency trajectories for the interaction between the Cy3-ssDNA primer and gp59(C42)-Cy5 in a ZMW. gp59(C42)-Cy5 was at 1 μ M bulk concentration. The fluorescence intensities of the Cy3 and Cy5 emissions are in green and red, respectively. (b) A magnified view of the FRET events and their FRET efficiency in the square region of (a). (c) FRET and FRET efficiency time trajectories show the presence of three major FRET states with apparent FRET efficiencies of 0.37, 0.45, and 0.6. (d) Representative FRET and FRET efficiency time trajectory between the gp59(C42)-Cy3 and Cy5-N-gp43(exo-) on the immobilized DNA primer in a ZMW.

The real-time monitoring opened a new avenue of investigation into the kinetic characterization of the FRET states (binding modes) of gp59 on ssDNA, which would enormously contribute to the understanding of helicase loading by gp59. Through various ensemble investigations,[132, 141] it has been proposed that in the absence of the gp32 single-strand DNA binding protein, gp59 through its interactions with DNA substrates recruits and orients the helicase on a DNA as a hexameric assembly. Thus, a description of the dynamics of gp59 interacting with DNA is integral to a comprehensive knowledge of the assembly process. The identification of the three main FRET states of gp59 on ssDNA by single-molecule imaging at the physiological concentrations using our developed platform could be construed as an initial step to this end. Further characterization of the states is in a progressing effort.

In addition to the interaction with DNA, gp59 is also known to interact with other T4 replisomal proteins, including the gp43 polymerase, the gp32 single-stranded DNA binding protein, the gp61 primase, and the gp41 helicase on DNA substrates, implicating its multiple roles in replication.[132, 139, 142] We next attempted to study the dynamic interaction between gp59(C42)-Cy3 and Cy5-N-gp43(exo-) on the tethered ssDNA primer in ZMWs. Note that the interaction between gp59 and gp43 occurs preferably on forked DNA substrates and that there is no report of such interaction on a short ssDNA primer. [142] Fig. 2-9(d) shows a long (>80 s), rare FRET event between gp59 and gp43 on short ssDNA that was previously obscured in ensemble studies. As exemplified by this FRET study of a protein pair, our ZMW/dark-field single-molecule fluorescence microscope is poised to reveal a comprehensive kinetic picture of the interaction network involving gp59 and other proteins, and its functional relevance to the replication activity of the T4 replisome.

2.5. Engineering Approach for Processivity Study of UvsW Proteins on Duplex DNAs: DNA Racks

As the most common reaction substrate, DNA molecules are often the interest of many single-molecule studies. The kinetics of DNA replisome proteins, such as sliding, collision, knock-off and rebinding, are usually observed through single molecule Fluorescence Resonance Energy Transfer (smFRET) that requires labeling of at least two types of fluorescent dyes to observe the single-molecule dynamics indirectly. [54, 143] Both single-strand DNA and duplex DNA maintain their natural coiled states in the absence of external stretching forces, making it is even more difficult to track the DNA replisome interactions during the replication process. Recent development on single-molecule manipulation techniques led to the inventions of several single-molecule techniques, which have substantial contributions to the single-molecule studies through their capability of manipulating individual DNA molecules. Optical tweezers grab the two beads with each of them connected to one end of a linearized DNA molecule. [94] By controlling the two beads independently, moving and stretching on the DNA molecule can be controlled using optical tweezers, providing suspended DNA substrate in solution for single-molecule reactions. Magnetic tweezers relies on magnetic field to interact in a noncontact fashion with one magnetic bead connected to one end of the DNA, the translocation of the replisome proteins can be discerned with spatial resolution of several base-pair with the other end of DNA molecule tethered at a non-stretchable substrate. [89] DNA curtain techniques aim to improve the event number of manipulated DNA molecules with the trade-off on inferior spatial resolutions as compared with both optical tweezers and magnetic tweezers. The much simpler design scheme and its availabilities in almost every lab make DNA curtain grow into a very popular single-molecule technique recently. [95, 144]

In this section, I will discuss our most recent progress on designing and demonstrating metallic DNA racks using engineering approaches. DNA racks with distributed metallic arrows

and metallic pentagon structures can first capture and extend DNA molecules in a fluidic environment. Extended DNA molecules then can be tethered to metallic pentagons, and stretched DNA molecules maintain their stretched states even after the flow stops. The stretched DNA molecules across the metallic arrows and pentagons can be used as reaction substrates to observe kinetics of various proteins that interact with DNA molecules. As compared with DNA curtain techniques stretching DNA molecules, our techniques allows capturing and stationing single DNA molecules without flow assist, making it a simple yet effective single-molecule manipulation technique to study single-molecule dynamics. Demonstration on processivity study of a helicase (UvsW) sliding along stretched DNA molecules revealed single-molecule dynamics such as sliding, switching strands, dissociation, etc, for the UvsW protein powered by ATP hydrolysis. [145-148]

2.5.1. DNA Curtain Technique Stretching DNA Molecules Using Artificial Barriers

DNA curtain technique invented by Greene's group at Columbia University adopted the very simple method creating nano-barriers to stop and accumulate long strand DNA molecules that are tethered to lipid surface. [95, 144] The DNA molecules are modified through annealing biotinylated primers to create biotin binding sites at their both ends. The glass substrate are treated with liposome to form a lipid bilayer, neutravidin-lipid conjugates are mixed into the lipid bilayers to generate distributed binding sites. The chemical binding between biotin and neutravidin grabs one end of DNA molecule and links them to the lipid surface. Due to the fluidic nature of the lipid bilayers, hydrodynamic force will drive DNA molecules to move at the surface of lipid layers after a flow is introduced into the reaction chamber. The drifting DNA molecules that are tethered to the fluidic lipid surface can then be stopped by any barrier that leads to the discontinuities of the lipid bilayer. In their demonstrated cases of DNA curtain experiments, they

have discussed several different possible designs that have been proven to be effective forming the barriers, including scratches on the surface and nano fabricated lines. The aligned DNA molecules at the barriers will experience stronger hydrodynamic forces with its end anchored at the barrier, thus leading to the extensions of DNA molecules that can be clearly observed using microscopes. A large number of DNA are stopped and extended at the same time of observation, and the extending and releasing of DNA molecules can be easily controlled by applying and removing the hydrodynamic flow. The large number of DNA molecule trapped and extended at the barrier form a “DNA curtain”, providing an intuitive way to observe protein dynamic behavior on stretched DNA molecules. In their observation on DNA repairing protein traveling along stretched DNA molecules, the large amount of reaction substrates carrying proteins can be recorded at the same time, and statistically significant conclusion has been drawn based on the data analyzing many events recorded at the same time period.

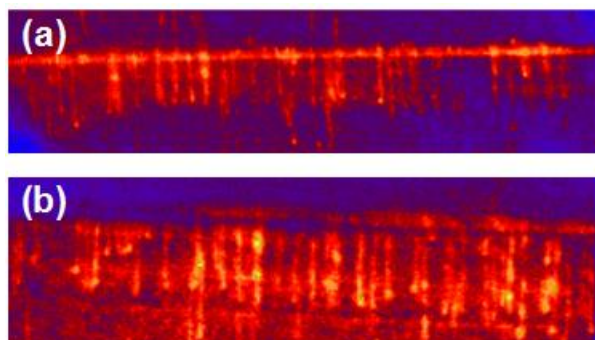


Figure 2-10. (a) DNA curtain stops and stretches DNA molecules at a nano barrier or engineered straight line. (b) DNA curtains formed utilizing the discontinuities carved in glass substrate. Both cases can accumulate, stretch, and align DNA molecules for single-molecule experiment.

As a very simple way to manipulate DNA molecules, DNA curtain technique shows great promises towards future single-molecule studies. However, it falls behind other single-molecule techniques in terms of spatial resolution, and most importantly, the capability of capturing single DNA molecules as desired. The large amount of DNA molecules accumulated at the barrier on one hand make it possible to observe and record many single-molecule events at one time; on the

other hand, the overwhelming number of DNA molecules will significantly reduce the sensitivity of detection due to the interference from adjacent molecules, and this undesirable effect grows worse as time goes because the continuous flow needed to stretch DNA molecules keeps bringing more DNA molecules to the barrier. In addition, the continuous flow which is crucial to stretch DNA molecules suffers from environmental vibrations, motor movements from mechanical pumps, as well as the deformation and possible leakage of the reaction chamber; thus creating great disturbance while stretching DNA molecules. The fluctuations of stretched DNA molecules caused by flow disturbance further reduce the spatial resolution of single-molecule imaging, making the technique more suitable for qualitative molecular studies rather than quantitative molecular studies. As such, it is necessary to develop a new single-molecule manipulation technique that can achieve DNA extending without flow disturbance and single molecule stretching and stationing at the same time.

2.5.2. Towards Engineering DNA Racks: DNA Stretching without Continuous Flow

Inspired by DNA curtain technique that utilizes the biotin-neutravidin binding to anchor DNA molecules to lipid substrate, we have engineered the other end of DNA molecules with digoxigenin, which will form chemical links to antidigoxigenin antibody. In this case, one end of the DNA molecule is modified with biotin, to react with neutravidin; while the other end of DNA is modified with dig, to bind with anti-dig maintaining DNA extension without continuous flow. Modified DNA molecules now have two binding sites, instead of one in the case of DNA curtain technique. The two binding sites make it possible for DNA extension without continuous flow, under the precondition that the distance between the two binding site can be controlled precisely. This can be realized by engineering another barrier away from the original barrier, with the distance between the two barriers being roughly the stretched length of target DNA molecules.

The metallic gold barriers are treated with thiol linking to the anti-dig, and can capture the dig end of the stretched DNA molecules.

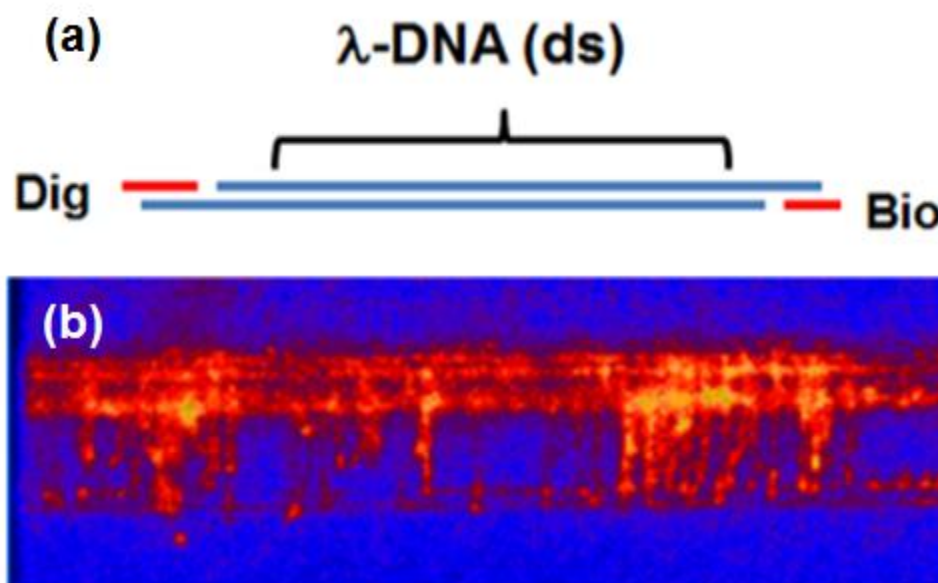


Figure 2-11. (a) Functionalization of duplex DNA molecules with one end modified with biontin, and the other end modified with digoxigenin. The biotin and digoxigenin will form chemical links with neutravidin and antidigoxigenin, respectively. (b) DNA molecules stretched with a modified DNA curtain design with two stop barriers. The dig end of DNA molecules will form chemical links to the second stop barrier which is treated with thiol-antidig. The DNA molecules can then be stretched even without continuous flow.

We firstly tested barrier design with just two nano-lines fabricated using electron beam lithography. The line width for both lines is $2\ \mu\text{m}$, and the distance between them is $12\ \mu\text{m}$ calculated as $\sim 75\%$ extension for λ -phage DNA molecules of $\sim 15\ \mu\text{m}$ in length. As expected, DNA molecules stopped at the first barrier experienced hydrodynamic force as in the case of DNA curtains, the dig ends of stretched DNA molecules reaching the other barrier treated with anti-dig have a very good chance forming dig-antidig bindings that anchor the dig sides of DNA molecules to the nano-barriers. After the binding was active, extended DNA molecules maintained their stretched length even without any hydrodynamic forces from flow.

Stretched DNA molecules in this case is much like the case of DNA molecules stretched by “DNA curtains”, with the advantage of preventing disturbances caused by continuous flow and amplified at the interface between fluids and the reaction surface. However, the accumulation of multiple DNA molecules at a same capturing site was not much improved, forming DNA curtains consisting of excessive number of molecules that is difficult to differentiate for single-molecule studies.

In order to isolate individual DNA molecules for better observations, we have modified our design of nano-barriers. The first capturing barriers have been modified with a “zigzag” structure from the line barriers, which helps to direct captured DNA molecules to designated positions for stretching and observation. On the other side of the zigzag barrier, we positioned distributed pentagons to capture stretched DNA molecules modified with dig antibodies, like the cases of dual barriers discussed above. A schematic of this design and our experiment results are shown in Fig. 2-12. Free DNA molecules travelling at the interface of fluids and lipid surface in this case will still be stopped by the zigzag nano barrier; however, because the biotin-netravidin binding of DNA molecules is on the interface rather than on the zigzag nano barrier, they will keep moving along the profile of the zigzag shape to the very edge of the zigzag tips before they are stopped. In this case, we are able to control the position of DNA molecules as desired, at the same time isolate them at different stretching sites to reduce the overwhelming signals observed in DNA curtains. It can be seen that DNA stretching using proposed design without flow assist is also possible. Stretched DNA molecules are aligned in parallel flowing designed shapes of zigzag structures and metallic pentagon capturing sites, and maintaining their stretched status even with continuous flow stopped.

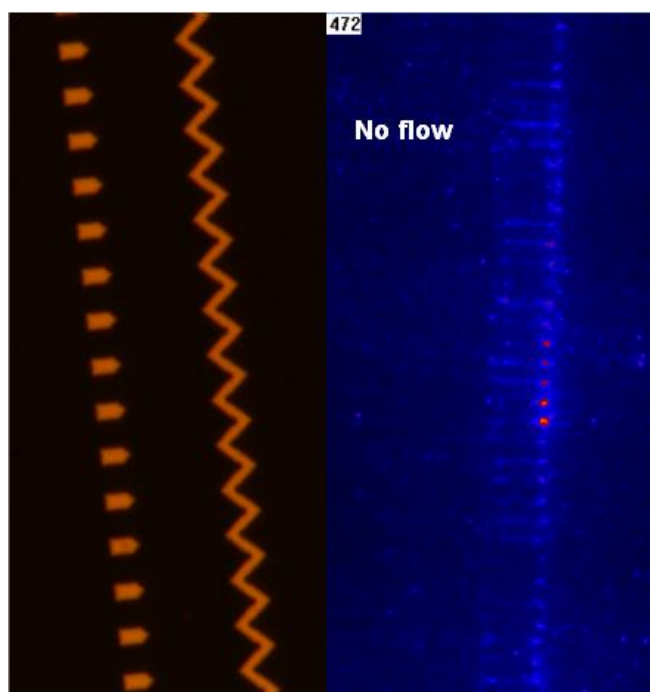


Figure 2-12. The design and optical image of “zigzag” nanostructure to stop, stretch, and isolate DNA molecules flowing the contour of the zigzag shape. The EMCCD results confirmed the structure can be used to stretch and isolate DNA molecules. The DNA molecules are stretched without any hydrodynamic forces.

2.5.3. Towards Engineering DNA Racks: Capturing Single DNA Molecule using Distributed Metallic Arrows and Metallic Pentagons

Both DNA curtains and zigzag nano barriers have been proved effective in capturing DNA molecules and stretching them out from their original coiled status for single-molecule experiment. However, one issue that challenges both designs is the capability of capturing and isolating single DNA molecules, instead of the accumulated DNA strands with complicated single-molecule signals that are difficult to understand. Both DNA curtains and zigzag nano barriers are continuous nanostructures that stop all DNA molecules within the capturing region, and inevitably lead to excessive accumulations of DNA molecules as time goes even under low

sample concentrations. This has been the last obstacle for us to apply this stretching technique for single-molecule study.

We solved this issue with a smart design that breaks the continuity of zigzag lines, keeping only the arrow edges that can capture DNA molecules while removing the rest part of the line. Noting that we choose to modify on zigzag nano barrier instead of straight lines due to the reason that the DNA is stopped by the geometrical structures and arrow shape is more likely to capture the DNA molecules than distributed straight lines. In addition, the first stops are aligned with gold pentagons and arrow structure can direct DNA molecules to be better aligned and captured by the pentagon capturing sites. The schematic and an optical image of fabricated distributed metallic arrows and pentagons for capturing and stretching single DNA molecules are shown in Fig. 2-13.

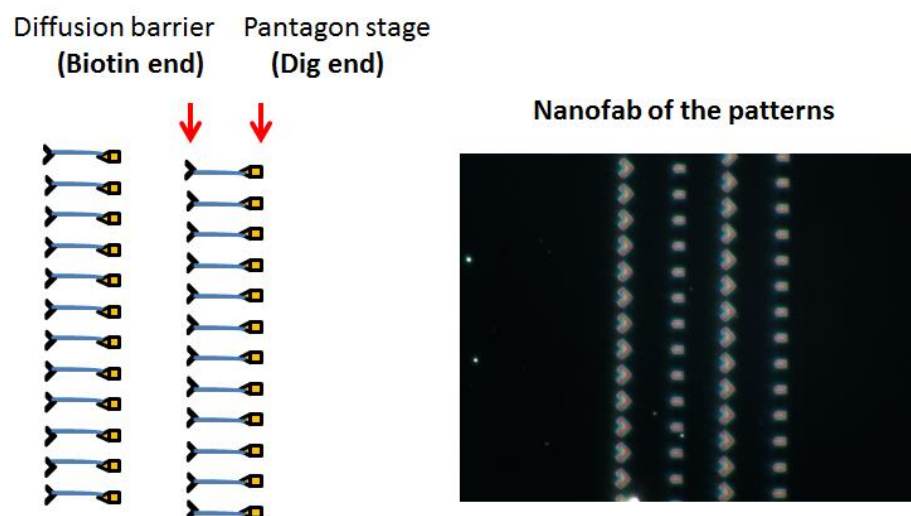


Figure 2-13. The design and optical image of distributed metallic nano arrows and pentagons that can capture and stretch on single DNA molecules. The break on the continuity of the original zigzag nanostructure design has significantly reduced the accumulation of a large number of DNA molecules at one capturing spot, offering better single-molecule signals and more single-molecule event numbers as compared with the original design.

Because we broke the continuous design originally proposed, we now allow DNA molecules to move pass the capturing region if they don't meet a capturing site on their way out.

As such, we can have multiple capturing regions following the first capturing region, with slightly shifted capturing sites to increase the possibility of DNA molecules being captured as they flow through. The accumulation of multiple DNA molecules at a single site has been much reduced, and we observed the increase on the event number of single DNA molecules being captured. The experiment results shown in Fig. 2-14 confirm on the single-molecule events with uniformed fluorescence intensity from labeled DNA molecules. As a comparison, the EMCCD images from both DNA curtains and zigzag capturing barriers present varying fluorescence intensities indicating the accumulation of multiple DNA molecules at one site.

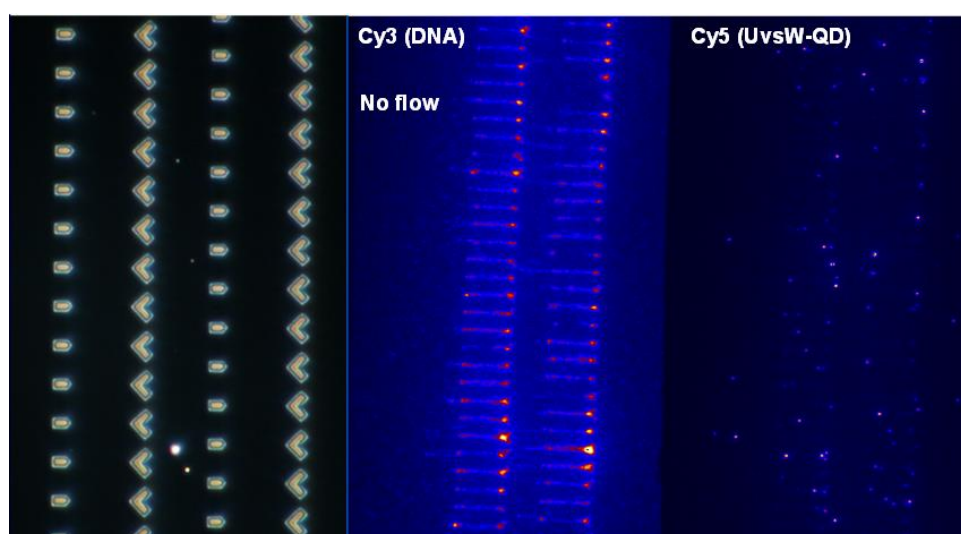


Figure 2-14. EMCCD images of distributed metallic arrows and pentagons for single DNA molecule capturing and stretching. The Cy3 channel shows the fluorescence labeled DNA molecules that are captured and stretched at different arrow-pentagon sites. The uniformity of the fluorescence signals confirm many single-molecule events in one observation regions. The Cy5 channel indicate the quantum dot signals that are correlated to the positions of T4 replisome proteins.

2.5.4. DNA Racks Studying Kinetics of UvsW Proteins Sliding along Stretched DNA Substrate

To test the functionality of our engineered DNA racks for single-molecule studies, we have designed experiment of tracking DNA replication protein kinetics on stretched DNA substrate obtained from our distributed metallic arrows and pentagons. We choose UvsW labeled with quantum dots as targets to observe their interactions with stretched DNA substrate under ATP hydrolysis. UvsW as an important helicase protein will bind to the DNA substrates to initiate fork regression as a DNA repair pathway. Even without a complete replication fork, it was proposed that it is capable of traveling along the duplexed DNA substrates with ATP providing the energy to drive it to move. As a proof-of-concept experiment, we want to see the kinetics of this UvsW proteins interacting with stretched DNA molecules through tracing their movements on the DNA substrates.

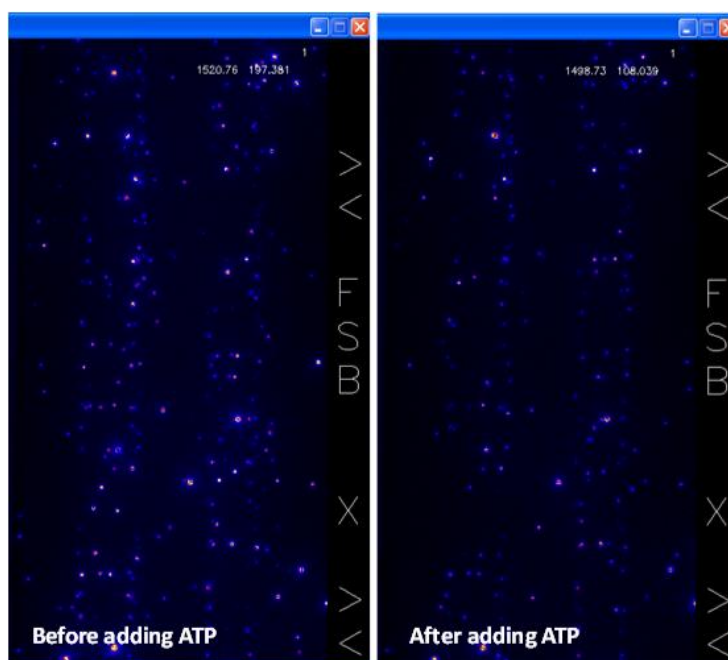


Figure 2-15. The EMCCD images of the same observing region before and after adding ATP. Because quantum dots don't photobleach, the missing quantum dots signals after adding ATP are likely caused by the movements, and possible sliding off, of the UvsW protein labeled with those quantum dots.

Our first conceptual experiment confirmed the binding and dissociation of UvsW-QDs interacting with stretched DNA substrate. With Fig. 2-15 showing the result of initial bindings of QD signals in the ATP solution in Cy5 channel, and the results of the same region observed using the same channel after 10 mins. It is quite obvious that the QD signals reduced significantly after 10 min of reaction. Unlike organic fluorescence dye that will photobleach after certain exposure time, QD signals are much stable with some intensity variations. The missing of much QD signals is strong evidence that UvsW proteins that originally bind to the stretched DNA substrates slide away during time elapse, indicating one type of interactions between UvsW proteins with the DNA molecules. Fig. 2-16 shows enlarged images confirming the movement of one single quantum dot labeled UvsW protein molecule.

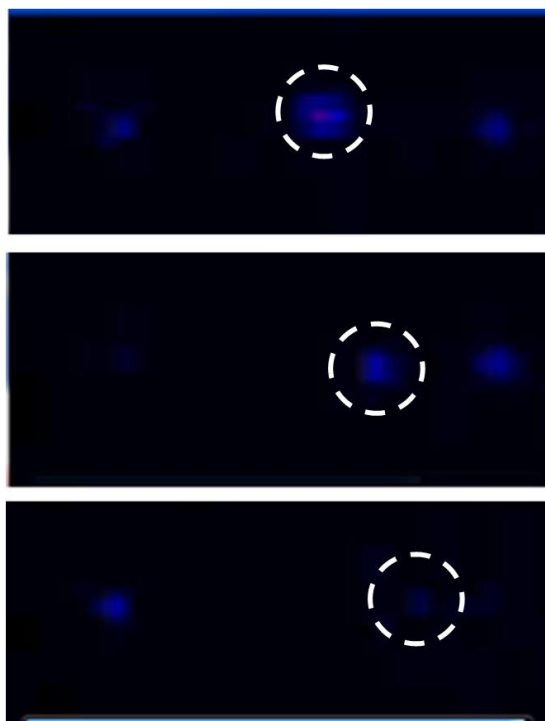


Figure 2-16. The trace of UvsW movement confirmed by the changes on captured signals from one quantum dots.

To further explore the details concerning the interactions between UvsW and DNA molecules, we need to resort to analyzing toolkit that could provide high tracking precisions to track the slight movement of protein processivity on stretched DNA molecules. We use a commercial software package of Nikon NIS to produce kymographs of protein activities over time elapse. We firstly recorded a video containing all the information during the experiment, and then export this video to Nikon NIS for image analysis. As shown in Fig. 2-17, we pick one region we are interested from the video, and the software to stitch all the frames recording the same region together and plot them against duration of the whole video. In such ways, we were able to track the movement of the QD signals through comparing their positions among all the frames. The results can be correlated to the movement of UvsW proteins on stretched DNA molecules over time. Noting that there are some signals missing in the kymographs, which is due to the intrinsic blinking the QDs. Because the blinking of the QDs is quite fast, it won't affect the tracking of QD signals which has much larger tempo-resolution, but will introduce background disturbance during the statistical analysis.

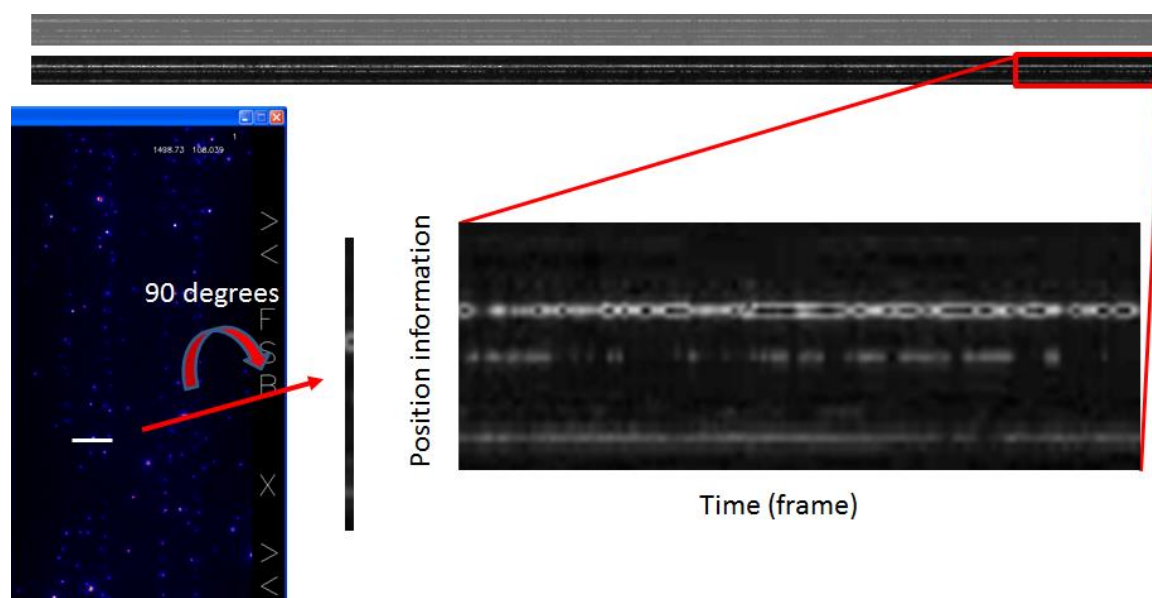


Figure 2-17. Kymography analysis on sliding of UvsW proteins along stretched lambda DNAs using Nikon NIS software.

Fig. 2-17 are the experiment results on tracking the movements of UvsW proteins over time. No movement can be observed for UvsW-QDs on stretched DNA molecules over time without ATP and flow. When we introduce 1mM ATP to the chamber with other conditions unchanged, the sliding of the proteins can be clearly observed. The back and forth sliding observed from the experiment results could possibly indicate the strand switching during the protein movements, while the continuous processing was also observed showing an overall preference of some individual protein activities. Additional experiments also revealed protein activities such as pausing, dissociation, etc, that are tied to the unique protein dynamics while interacting with DNA molecules during the DNA replication process.

To confirm the critical role of ATP hydrolysis during the UvsW sliding experiment, our last kymograph captured protein activities before and after introducing ATP solution. It is clear that initial movement started only after introducing the ATP solution, confirming the critical role of ATP in the process of UvsW translocation on duplex DNA, as well as ruling out the random diffusion or artificial factors that might also lead to protein sliding along stretched DNA molecules.

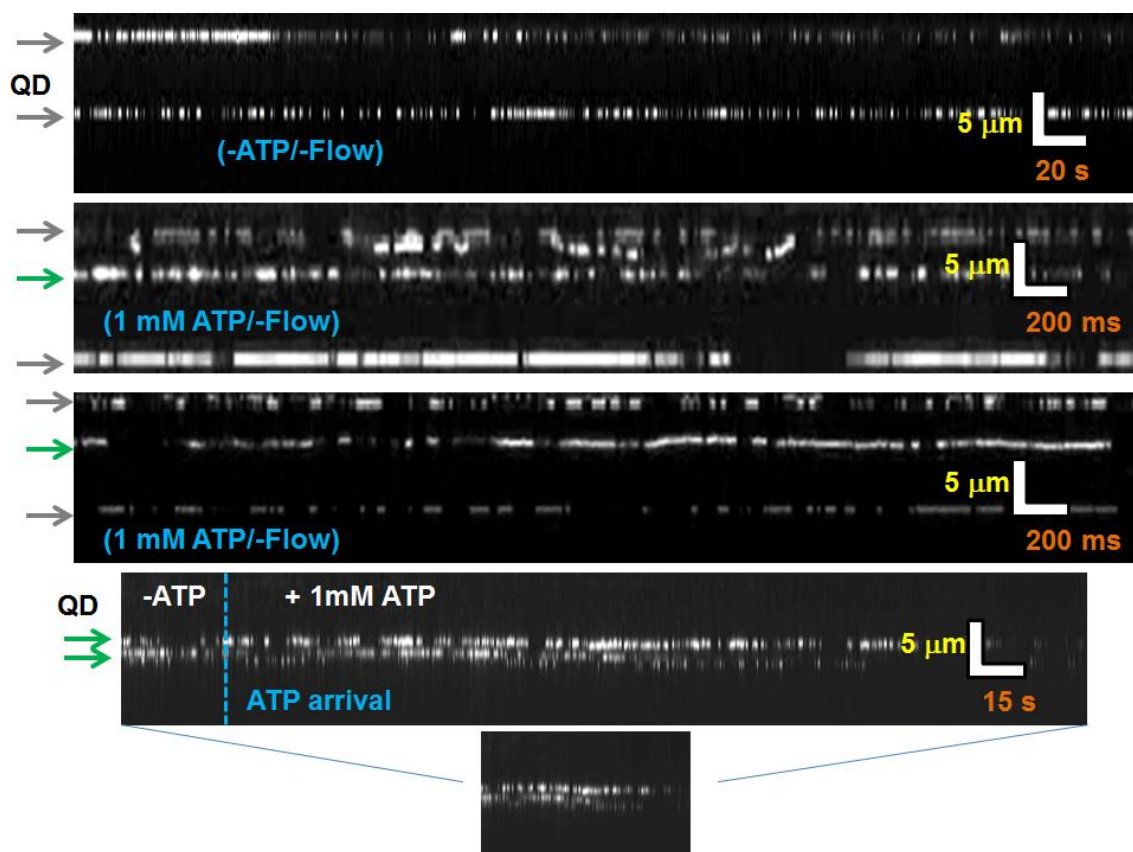


Figure 2-18. Tracking results of quantum dots signal movements recorded as kymographs using Nikon NIS. The control experiment with and without ATP confirmed sliding of UvsW protein under ATP hydrolysis. The dynamics of UvsW have been confirmed as back and forth sliding behaviors, as well as preferable sliding directions towards certain ends of stretched DNA molecules.

2.6. Summary

In this chapter, I reported two single-molecule technique developments focusing on single-molecule detection and single-molecule manipulation, respectively. In specific, I have addressed the constraint of the microscope configuration associated with the Al/ZMW nanostructures for single-molecule fluorescence imaging. With the advantages of simple optical deployment and effective suppression of the background fluorescence and noise levels by spatially separating the light path of the fluorescence emissions from the reflected excitation

beam, the conical lens based dark-field fluorescence microscope we employed has allowed single-molecule fluorescence measurements with high S/N ratios. We also showed that this microscopy setup in combination with the ZMW/microfluidic chip enabled smFRET studies on the weak interaction between a DNA primer (Cy3) and gp59(Cy5) at up to micromolar concentrations, and rare binding events between gp59(Cy3) and gp43(Cy5) on a short DNA primer. The engineered DNA racks consisting of distributed metallic arrows and pentagons have proved as a simple yet effective way in manipulating single DNA molecules for single-molecule studies. The metallic arrows and pentagons can be precisely positioned with engineering plasmonic approach, offering great adaptability of this technique for extensive single-molecule studies. A proof-of-concept experiment studying the protein activities of UvsW polymerase labeled with quantum dots is a strong evidence indicating this technique can provide reaction substrates of single DNA molecules for complicated molecular interactions.

Chapter 3

Engineering Plasmonics for Practical Applications: Solar Energy Harvest and Color Pixel Display

Other than the promising potentials of the engineering plasmonic approaches on studying fundamental biological problems, this methodology has also been found effective and innovative in addressing practical issue and challenges. Built upon my in-depth understanding on plasmonic resonance theories, my researches targeted significant challenges in practical related applications of improving solar cell efficiency and constructing high-resolution display. Specifically, I have developed nanophotonic devices through engineering methods and demonstrated their superior capabilities of collecting solar energy effectively in the near infrared range, which consists of almost half of the total solar energy. The almost perfect absorption of infrared solar energy through an optical-thin layer structure can be an added-on to many existing solar energy products. Combining with proper optoelectronic circuits, such design allows the possibility to manufacture highly efficient solar cell devices, leading to reduced cost on utilizing solar energy at the same time increasing the profits for the industrial manufactures. In my efforts exploring the source-less color pixels, I have proposed and demonstrated plasmonic color filters that feature with ultra-small sizes, robust sustainability, and various working modes including transmissive, reflective, and rotation modes. The ultra-small plasmonic based color pixels will allow the current display industries to manufacture long-lasting high resolution display with ultra-density pixel densities for hand-held devices. Their applications on projection techniques will also provide the capability of controlling phase, enriching the functionalities of current Digital Micromirror Devices (DMD) and Digital Light Processing (DLP) devices.

This section consists of the information from my follow publications with necessary adaptions.

Polarization Independent Dual-Band Infrared Perfect Absorber Based on a Metal-Dielectric-Metal Elliptical Nanodisk Array, *Optics Express*, Vol. 19, pp. 15221–15228, 2011. [149]

Light-Driven Tunable Dual-Band Plasmonic Absorber using Liquid-Crystal-Coated Asymmetric Nanodisk Array, *Applied Physics Letters*, Vol. 100, pp. 053119, 2012. [150]

Reflective Plasmonic Color Filters Based on Lithographically Patterned Silver Nanorod Arrays, *Nanoscale*, Vol. 5, pp. 6243-6248, 2013. [151]

Annular Aperture Array Based Color Filter, *Applied Physics Letters*, Vol. 99, pp. 033105, 2011. [152]

3.1. Near Perfect Absorber Based on Engineering Plasmonic Nanostructures

Light absorption in plasmonic nanostructures has recently attracted significant interest in the research community for applications such as solar cells, [153-155] metamaterials, [156-159] photodetectors, [160, 161] sensors, [162-165] nanoimaging devices, [70, 166-168] and thermal emitters. [169, 170] Various nanostructures with enhanced absorption have been proposed utilizing state-of-the-art nanofabrication techniques. [171-174] Kravets et al investigated high-efficiency absorption in a plasmonic blackbody using a composite grating nanostructure. [175] Nearly complete absorption was observed in the structure at a wide-range of wavelengths and incident angles; however, the optical properties of the one-dimensional refractory metallic coatings were strongly polarization-dependent. Following this work, Kravets et al introduced another design consisting of embedded silver nanoparticles in an Al_2O_3 dielectric matrix; [176] the light scattered by the nanoparticles was trapped inside the dielectric matrix, demonstrating an

effective absorption near unity. Na et al extended the design concept from a single-layer structure to a multi-layer structure and proposed a design in the infrared range for sensing applications. [163] They demonstrated, both experimentally and computationally, nearly zero reflection in a metal-dielectric-metal structure working in the infrared wavelength regime. Although the aforementioned designs exhibit excellent absorption efficiencies, they are constrained with issues such as relatively narrow working ranges, lack of reconfigurability, or strong polarization dependence. One straightforward way to increase the working range of a plasmonic absorber is to introduce another absorption band into the spectrum by incorporating a functional layer into the structure. [177, 178] The complex design and fabrication, however, have thus far restricted the wide application of this approach.

3.1.1. Polarization-Independent Dual-Band Infrared Perfect Absorber Based on A Metal-Dielectric-Metal Elliptical Nanodisk Array

In this section, I will discuss the design and fabrication of a dual-band perfect plasmonic absorber with reconfigurable band positions. Our design exhibits multiple advantages over other plasmonic absorbers: a wide working range, incident angle insensitivity, simple reconfigurability, polarization independence, and easy fabrication process. We believe that such a design will enhance the functionality of plasmonic absorbers and be valuable in many applications such as sensors, solar cells, and metamaterials.

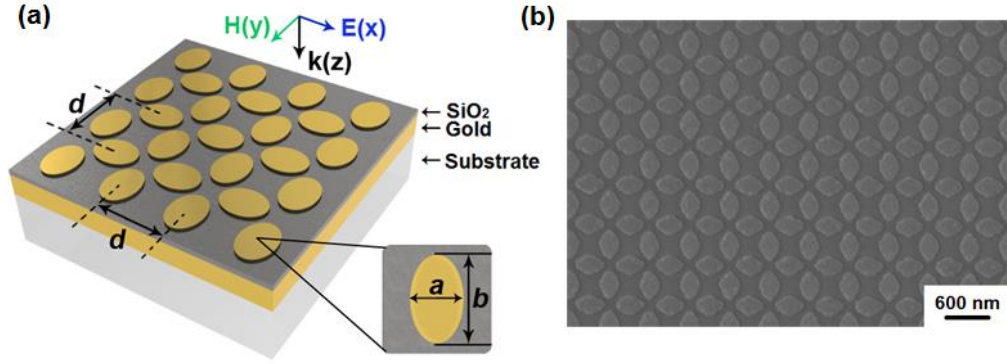


Figure 3-1. Schematic of the dual-band perfect absorber structure and the incident polarization configuration. (b) A SEM image of the designed structure.

Structure design

A schematic and SEM image of our dual-band absorber are shown in Fig. 3-1. The physical origin of near perfect absorption is the localization of electric and magnetic dipole resonances in the metal-dielectric-metal structure. The dual-band absorption was realized using elliptical nanodisks, which possess two resonance peaks associated with their major and minor axes. [20, 179] We eliminated the polarization affinity by carefully arranging the elliptical nanodisks in a two-dimensionally symmetric structure. As shown in Fig. 3-1, our structure consists of three functional layers comprised of a dielectric layer sandwiched between two metal layers. The top metal layer is a 20 nm thick elliptical gold nanodisk array, where a denotes the length of each nanodisk's minor elliptical axis, b represents the length of the nanodisk's major axis, and d corresponds to the period along both x and y directions. The design parameters (a , b , and d) can be selectively tuned to demonstrate control of the structure's optical properties. The center spacing layer provides a large impedance mismatch between the constituent material and the metal claddings. Here, dielectric materials with relatively low permittivity, such as SiO_2 , MgF_2 , or other polymer materials, are ideal candidates for high absorption. [180, 181] For the real fabrication process, we choose SiO_2 as the spacing layer to verify our design. Fig. 3-1(b) shows a

SEM image of our structure. We can see the pattern of the nanodisks shows a good uniformity along both the x and y directions. The thickness of the dielectric layer is crucial because it affects the dipole resonance; as thickness increases, the resonance effect is diminished and the overall absorption efficiency is reduced. We optimize the performance of the perfect absorber with a 30 nm thick SiO₂ layer and a 150 nm gold bottom functional layer. This thickness is larger than the penetration depth of electromagnetic waves in the infrared regime, and will block any incident light transmitted through the first two layers, leading to nearly zero transmission in the working range of the dual-band absorber. Another function of the thick gold mirror is to interact with the upper nanodisks to form electric and magnetic dipoles which couple the incident electromagnetic energy inside the structure. Therefore, near perfect absorption is obtained ($A = 1 - R - T$).

Nearly perfect dual-band absorption

To numerically investigate the performance of our design, we employed a commercial software package (Lumerical) utilizing Finite Difference Time Domain (FDTD) methods. In our simulation, the material property of gold was chosen from the software database (Gold (Johnson and Christy)) and the permittivity of MgF₂ was set to 1.9. Periodic boundary conditions were used for both x and y directions, and a perfect matching layer boundary condition was used for the z direction. The mesh size was 8 nm in both x and y directions and 2 nm in z direction. We used a long simulation time of 1000 fs with a step of 0.006 fs to provide reliable results. We set the auto-cutoff value to 1×10^{-6} in our simulation which can be further decreased to get results even closer to the ideal case. Fig. 3-2(a) shows the reflection and transmission spectra under normally incident electromagnetic plane waves with the fixed polarization state given in Fig. 3-1(a). In the simulation, the thickness of the top layer elliptical gold nanodisk array is 20 nm; the periods along both x and y directions are 600 nm; the minor and major axes of the elliptical gold

nanodisks are $a = 240$ nm and $b = 360$ nm, respectively; and the bottom gold layer is 150 nm. The SiO_2 dielectric spacer between the two metal layers is 30 nm thick. With these optimized design parameters, nearly zero transmission is obtained within the whole working range of the dual-band absorber, and two perfect absorption peaks are obtained at $\lambda_1 = 1247$ nm ($A_1 = 99.5\%$) and $\lambda_2 = 1697$ nm ($A_2 = 99\%$). To detail the overall incident wave absorption, the reflection and transmission spectra were also plotted in logarithmic (dB) scale in Fig. 3-2(b)

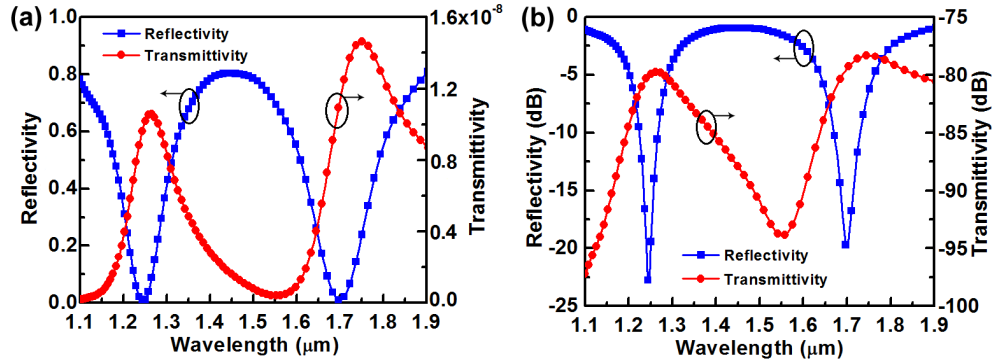


Figure 3-2. The reflection and transmission spectra under normally incident electromagnetic plane waves with the fixed polarization state given in Fig. 1(a). Results are shown in linear scale (a) and logarithmic (dB) scale (b), respectively.

We further investigate our dual-band absorber by changing the dimensions of the elliptical nanodisks which enables a repositioning of the absorption peaks while maintaining their dual-band characteristics. Figure 3-3(a) shows a tunable range of resonant frequency which was modeled up to 700 nm without optimizing the period of the nanodisk array. For $a = 240$ nm and $b = 360$ nm, nearly zero reflectance was achieved at the wavelengths $\lambda_1 = 1247$ nm and $\lambda_2 = 1697$ nm. More than 99% absorbance is obtained at both of the resonance frequencies. Increasing the size of nanodisks causes a red shift of the absorption peaks, which is due to the red shift of the plasmonic resonance in each particle with increasing size, in addition to the red shift associated with a decrease in space between particles. For $a = 270$ nm and $b = 390$ nm, the two resonance wavelengths shift to $\lambda_1 = 1372$ nm and $\lambda_2 = 1824$ nm, respectively. For larger nanoparticle sizes, a

$= 300$ nm and $b = 420$ nm, the two resonance wavelengths move further to $\lambda_1 = 1484$ nm and $\lambda_2 = 1954$ nm, respectively. We also investigated individual band control by changing the size of only one axis of the elliptical nanoparticle. The result in Fig. 3(b) shows that the two absorption bands could also be adjusted individually which indicates the great flexibility of our dual-band absorber over the near infrared regime.

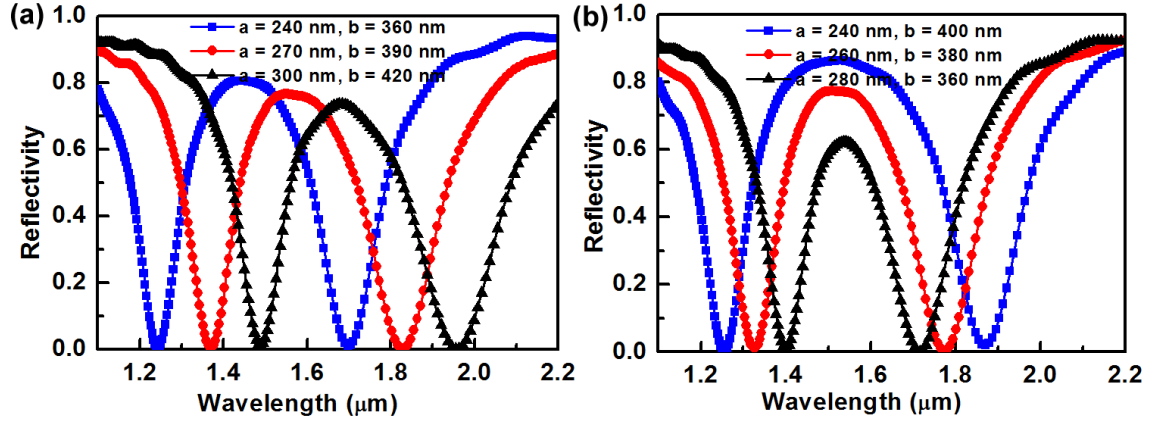


Figure 3-3. Simulated reflectance spectra of the designed absorber structure at normal incidence with different dimensions of the elliptical gold nanoparticles. A 700 nm tunable range can be conveniently achieved by engineering the sizes of the gold nanoparticles on the top layer. The two absorption peaks can be easily tuned both (a) in parallel and (b) independently.

We conducted additional simulations to investigate the angle dependence of our dual-band plasmonic absorber. For oblique incidence, because there will be a phase shift for the incident electromagnetic field between each period, we used Bloch boundary conditions in the x -direction (propagation direction) for both TE and TM polarization, while maintaining all other aforementioned parameters. Fig. 3-4 shows the absorptivity as a function of both wavelength and angle of incidence under TE and TM polarizations. The two red strips in the figure indicate the two angle-independent high absorption bands. Under both TE and TM polarizations, for incident angles (θ) up to 50 degrees, more than 95% absorption is still obtained for both of the two resonance peaks while maintaining the center frequencies. To detail the absorption peak value

degradation between normal incidence and large angle incidence, the absorption efficiencies of different angles for each peak under TE and TM polarization are listed in Table 3-1.

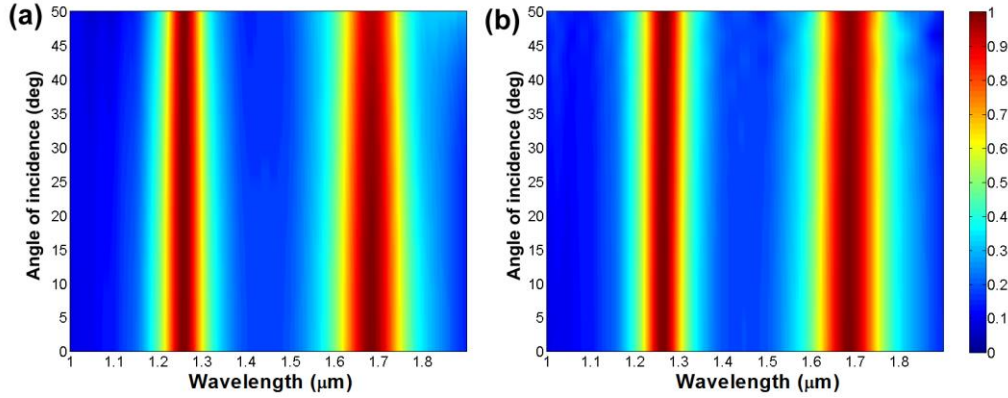


Figure 3-4. The simulated absorption efficiencies as a function of wavelength and angle of incidence under (a) TE and (b) TM polarization.

Table 3-1. Absorption efficiencies of different angles for each peak under TE and TM polarization.

	0°	10°	20°	30°	40°	50°
Peak 1 (TE)	99.5%	99.5%	99.4%	99.4%	99.2%	99.2%
Peak 1 (TM)	99.5%	99.5%	99.5%	99.4%	99.4%	99.4%
Peak 2 (TE)	99.0%	98.7%	98.5%	98.2%	96.6%	95.1%
Peak 2 (TM)	99.0%	98.8%	98.8%	98.7%	98.6%	98.5%

Nanofabrication and experimental measurement

The sample (Fig. 3-1(b)) was fabricated using standard lift-off electron-beam lithography. [174] First, a 150 nm thick gold mirror is thermally evaporated on a clean glass substrate, then a 30 nm thick SiO₂ film is deposited on the top of the bottom gold layer. Electron-beam lithography and a metal lift-off process are used to define the elliptical gold nanodisks on the top layer. The major and the minor axes of the gold elliptical nanodisks are approximately 360 nm and 240 nm, respectively. Also, 2 nm chromium layers are deposited between each gold/SiO₂ interface to promote adhesion. The reflectivity of the fabricated dual-band absorber at normal incidence is

measured with a Fourier transform IR (FTIR) spectrometer (Bruker IFS 66/S) equipped with a liquid nitrogen cooled, mercury cadmium telluride detector.

The measured and simulated results under TE and TM polarization are shown in Fig. 3-4(a-b), respectively. The experimental measurements match well with the simulations and the absorber shows excellent insensitivity to incident polarization. The absorption peaks maintain their position for both longer and shorter resonance wavelengths under different polarizations. For the longer wavelength absorption peak, under both polarizations, the measured results show a resonance wavelength at $\lambda_1 = 1703$ nm, matching well with simulations predicting 1679 nm, and the absorption efficiency is slightly reduced from the simulated 99% to 93.2%. For the shorter absorption peak, a 27 nm difference is observed between the simulations and experiments under both polarizations. The resonance wavelength moves from the simulated 1247 nm to the measured $\lambda_2 = 1274$ nm and the absorption efficiency decreases to 89.3%. We believe that the slight shift of the absorption peaks comes from the fabrication deviations of the sizes of the elliptical nanoparticles. As we discussed in Fig. 3-3, a larger gold nanoparticle size will cause a red shift of the absorption peak; thus it is likely that the size of the fabricated sample is a little bit larger than the simulated parameter. The reduction in absorption efficiency can be mainly attributed to the 2 nm thick chromium layer between the gold/SiO₂ interfaces. These layers affect the magnetic resonance between the top gold nanoparticles and the bottom gold layers. Consequently, reduced absorption efficiency is obtained. Also, the roughness of the fabricated nanoparticle may be another reason to the loss of absorption. The surface roughness will not only increase the scattering, but also affect the thickness of the top layer nanodisk array which is essential to the magnetic dipolar resonance between the nanoparticle and bottom gold film. In addition, the periodic boundary conditions approximate an infinite array in the simulation while the experiment was measured with limited periods; this discrepancy will also affect the results. We may improve the performance of our device by choosing other dielectric layers for real

fabrication, such as polymer materials, which have relative low permittivity and do not need adhesive layers. Although the measured absorption efficiency does not perfectly match simulations, high absorption is still obtained for both of the two resonances frequencies; validating the design experimentally.

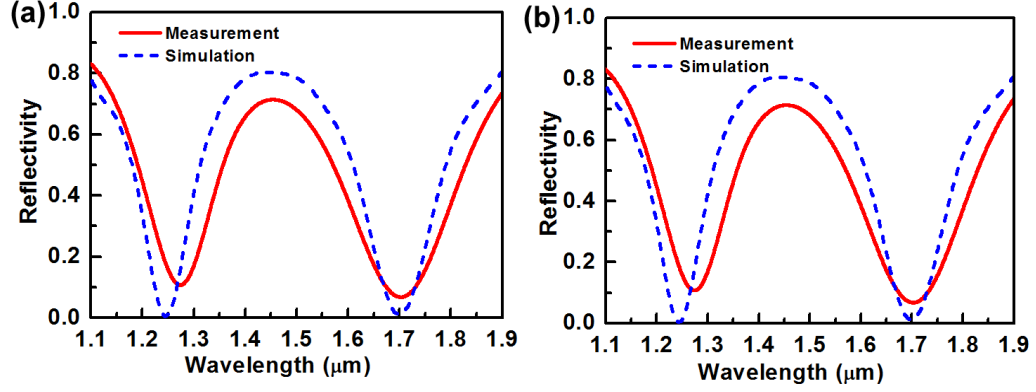


Figure 3-5. Measured and simulated reflection spectra of the dual-band absorber under (a) TE polarization and (b) TM polarization at normal incidence.

Mechanism of enhanced absorption

As stated above, the physical origin of the near perfect absorption in our structure is related to the electric dipolar resonance in the nanodisk array due to localized surface plasmon resonance and the magnetic dipolar resonance between the nanodisk array and gold film. To understand the nature of the magnetic and electric resonances, the charge distribution in multiple cross-sections of a single nanoparticle and the underlying structure were calculated at resonance wavelengths $\lambda_1 = 1697$ nm (cross section given along major axis) and $\lambda_2 = 1247$ nm (cross section given along minor axis). The results are given in Fig. 3-6(a) (λ_1) and Fig. 3-6(b) (λ_2). The charge distribution indicated that anti-parallel currents are formed in the elliptical gold nanodisk and the bottom gold layer creating circulating currents between the two metal layers. This circulating current is known as a magnetic resonance, which results in an artificial magnetic moment that

interacts strongly with the magnetic field of the incident light. [182] Therefore, strong enhancements of the localized electromagnetic fields are excited between the two metal layers at resonance frequencies. As a result, the incident electromagnetic energy can be efficiently confined to the intermediate dielectric spacer. In order to better understand the confined electromagnetic energy, the electric field distributions in the cross-sections along both major and minor axis of a single nanoparticle at the resonance wavelengths are showed in Fig. 3-6(c) and Fig. 3-6(d). In our absorber structure, the strongest electromagnetic interactions are obtained at these resonance wavelengths. The enhanced electric fields are confined between the top gold nanodisks and the bottom gold mirror and then transformed into heat. This effect leads to the nearly zero reflectance observed experimentally and computationally. Furthermore, we can confirm, from Fig. 3-5, that the two absorption wavelengths of our dual-band absorber originate from the interaction between the incident electromagnetic field and the elliptical gold nanoparticles along both the major and minor axes.

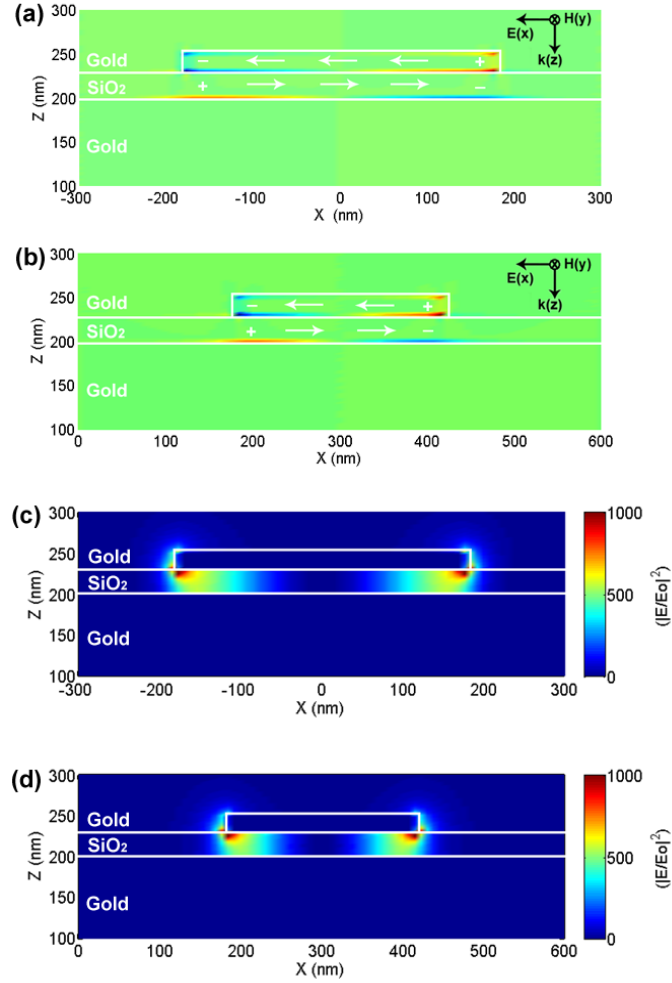


Figure 3-6. Calculated charge and field distribution at resonances (a) (c) $\lambda_1 = 1697$ nm (cross section given along major axis) and (b) (d) $\lambda_2 = 1247$ nm (cross section given along minor axis) where perfect absorbance occur. Anti-parallel currents are indicated by the charge distribution and the enhanced electric fields are confined between the top gold nanodisks and the bottom gold mirror.

Section Summary

In this subsection, I discussed my work on a dual-band perfect plasmonic absorber in the near-infrared frequency regime by utilizing a metal-dielectric-metal, three-layer nanostructure. Nearly 100% absorption peaks are obtained at the resonance frequencies with the device demonstrating nearly perfect polarization-independence at normal incidence, and maintaining

near-perfect absorption at incident angles up to 50° . Moreover, a tunable range of the resonant frequency was modeled up to 700 nm by tuning the dimensions of the nanostructures. Experimental measurements show a good match with the simulation results. With its excellent performance, our design can be valuable in many applications such as solar cells, metamaterials, and sensing. Also, we believe that perfect absorbers in the visible regime, multi-band or broad-band with simple designs are interesting directions to pursue in future work.

3.1.2. Light-Driven Tunable Dual Band Absorber with Liquid-Crystal Plasmonic Asymmetric Nanodisk Array

Recently, researchers have focused on developing plasmonic absorbers with extended working frequency ranges or multiple resonances. [149, 178, 183] The performance of the plasmonic absorber is determined by its engineered configuration, thus it is hard to reconfigure the device or tune the absorption bands without redesigning and repeating the entire fabrication process. Solar cells typically have a narrow absorption spectrum, and an actively tunable plasmonic absorber could be used to optimize the solar cells efficiency. In this section, we demonstrate a real time reconfigurable enhanced plasmonic absorber by incorporating a photosensitive nematic liquid crystal (PNLC) layer onto a asymmetric gold nanodisk array which we have previously shown to exhibit two near-perfect absorption bands. The photosensitivity of PNLC arises from the azo-dye dopants, which can change the refractive index of the liquid crystals through several mechanisms. [184] Compared to other tuning mechanisms such as electric fields [185] and acoustic waves, [186] optical tuning is preferable since no electrodes or other direct contact is needed. In this proof-of-concept study, the refractive index change is attributed to thermal effects caused by light absorption by the azo-dyes. Without optimization, we

have observed a tuning range of about 25 nm in the dual absorption bands of the plasmonic nano-disks array.

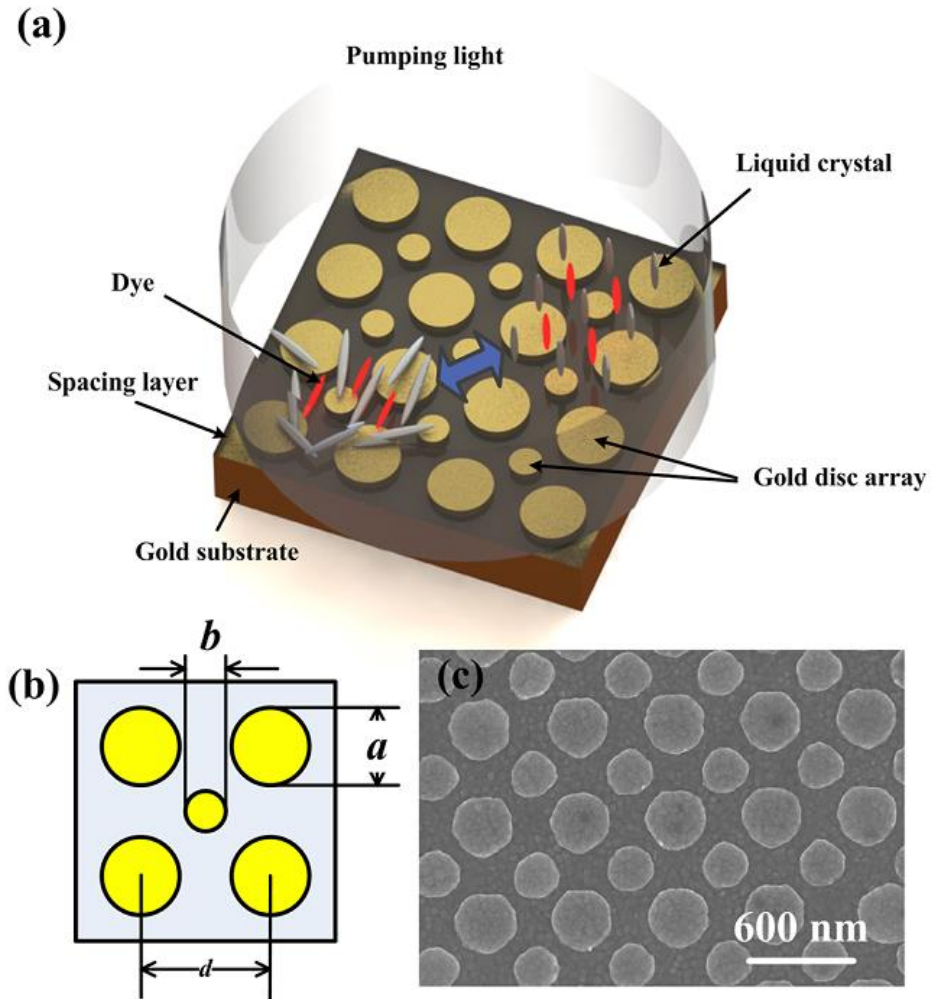


Figure 3-7. Schematic of light-driven tunable plasmonic absorber. Light sensitive liquid crystal mixture on top of the absorber can be modulated with light. (b) The top layer consists of two sets of alternatively arranged two dimensional nanodisks with the same period, followed up by a spacing layer of SiO_2 and a bottom gold layer. (c) SEM images of fabricated near perfect plasmonic absorber working at dual frequencies.

Structure Design

A schematic of the design is shown in Fig. 3-7(a). The near perfect plasmonic absorber comprises two different sizes of gold nanodisks which exhibit two localized surface plasmon resonances (LSPR). [179] These resonant frequencies are determined by the size of the metal nanodisks, as well as the inter-spacing between them. As discussed in Ref. [163] and Ref. [157], electric or magnetic dipole will form in a three layer structure; these dipole oscillations will completely convert a specific electromagnetic energy into displacement current between the two metal layers, thereby confining this part of energy inside the layered structure until it completely dissipates through the structure, indicating perfect absorption phenomenon at the specific frequency. Using two different sizes of gold nanodisks will therefore result in dual absorption bands.

Fig. 3-7(c) shows the SEM image of an exemplary near perfect plasmonic absorber fabricated in our laboratory. Our three-layer structure consists of a new configuration for the top gold pattern to achieve the dual-band near perfect plasmonic absorber and a 200 nm gold bottom layer that is thick enough to block any incident/transmitted light. We use Silicon Dioxide as the middle spacing layer. Two points needed to be considered when building this layer. First, it should be thin enough to ensure the coupling happen between the top and bottom metal layers, i.e. thin enough such that the surface plasmons generated in the top layer can reach the bottom layer. Secondly, a dielectric with relative high dielectric constant is preferred as high refractive index can support high-order wave components existing as propagating waves, thus enhancing its ability to confine more energy. The top layer consists of two nanodisk arrays arranged in a 2D pattern with the same period, as shown in Fig. 3-7(b). The two nanodisk arrays with different sizes are designed to have different plasmonic resonances interacting with incident light.

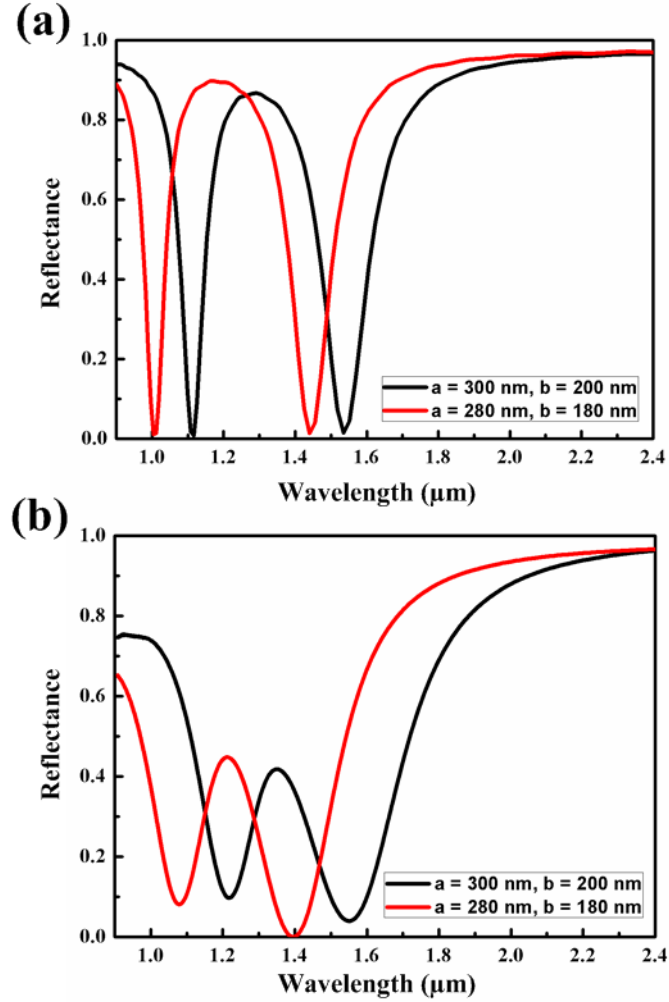


Figure 3-8. (a) Two design instances of the near-perfect plasmonic absorber (i) $a = 300$ nm, $b = 200$ nm, and (ii) $a = 280$ nm, $b = 180$ nm. FDTD simulations show that near perfect absorption can be achieved at selected wavelength ranges (b) Experiment results of the two designs Over 90% absorbing efficiencies can be achieved.

Numerical Simulations and Experiment Characterizations

We have performed several numerical modeling and experimental characterization of our plasmonic absorber; results of these studies are given in Fig. 3-8. The numerical modeling is performed by using commercial simulation software Lumerical FDTD with material parameters (Au and SiO₂) provided by the material library in the software. The incident electromagnetic

wavelengths range is from 0.9 μm to 2.4 μm with controllable polarizing angle and incident angle. The periodic boundary condition is applied on both directions of the two-dimensional array. The incident plane is located above the structure, and impinging on the structure from the top. An observation plane is put above the incident plane to collect the reflected light from the structure. The distance between the observation plane and the structure is 500 nm, which is close enough to collect any scattered electromagnetic waves. Another observation plane is located beneath the substrate to collect any transmitted electromagnetic waves. In our case, there is no transmitted light at all, since, as we mentioned above, the bottom gold layer is thick enough to block all the incident electromagnetic waves. The periods of both large and small nanodisk arrays here are set as 600 nm with thickness of 30 nm for a demonstration case. We provide two different designs with different combinations of large nanodisk and small nanodisk arrays with $a = 300$ nm, $b = 200$ nm; and $a = 280$ nm, $b = 180$ nm.

Fig. 3-8(a) depicts the corresponding simulated results. Near perfect absorption of the incident electromagnetic waves are represented as two near-zero reflection minima. By resizing two nanodisk arrays, large shifts in these absorption dips can be observed. Experimental confirmation using FTIR (Bruker FTIR, HYPERION 3000) is plotted in Fig. 3-8(b), with the exact parameters used in Fig. 3-8(a). The results match almost perfectly in terms of the position of the absorption peaks, with slightly reduced absorption as compared to the ideal case in simulations. The slight differences between the two cases are likely due to imperfections in the fabrication, and ideal boundary conditions used in the simulations (e.g. periodic boundary conditions for large area nanodisk array) whereas during the measurement, the measured area is limited by the instrument with limited view of field. Nevertheless, the measured value of over 90% absorption is arguably near-perfect.

As described in the previous section, the absorption bands of plasmonic absorber can be shifted by resizing the nano-disks and repeating the fabrication process. A less tedious approach

is to incorporate a tuning mechanism in the structure. Among the various methods and media that have been used to tune plasmonic resonances, [170, 187-193] nematic liquid crystals are attractive due to their large birefringence and easy susceptibilities to various applied fields. [184, 194-198] Among the recent demonstrations of such tuning capabilities using ac, acoustic or optical fields, the latter is most preferred as they do not require electrodes or other direct contacts with the structures. Furthermore, all-optical modulations of the liquid crystal birefringence can be effected at speeds several orders of magnitude faster than with electro- or acousto-optical. For example, laser induced thermal, density and order parameter changes induced by short pulsed lasers produce the required refractive index changes in microseconds to nanoseconds. [194-196]

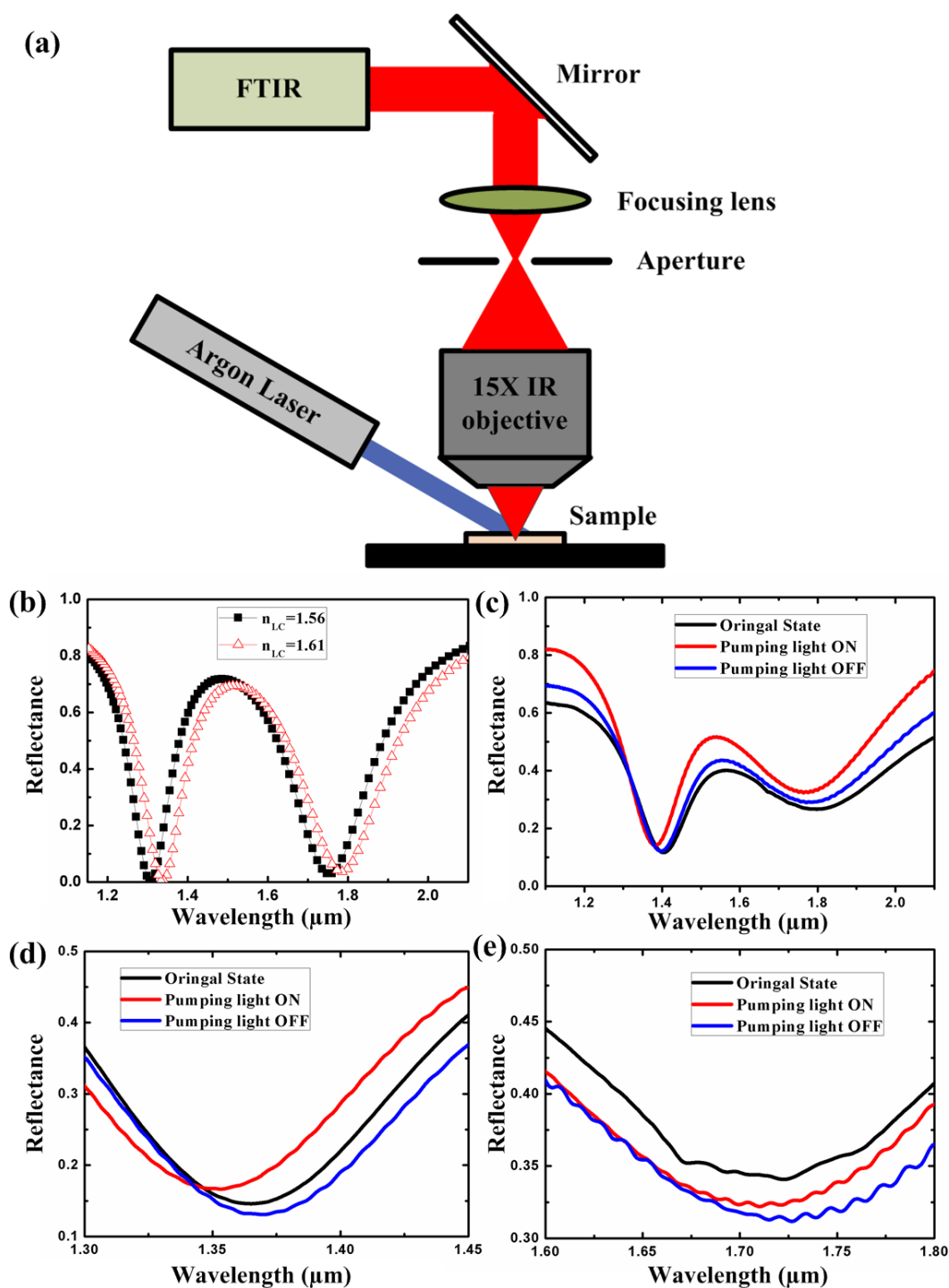


Figure 3-9. (a) Experimental setup for measuring optically tunable plasmonic absorber. (b) FDTD simulation results of the performance of the plasmonic absorber with an overlayer of liquid crystals. Around 30 nm shiftiness can be observed. (c) Measured absorption band shifts with the pumping light turned ON and OFF. The band shifting process is reversible and repeatable. (d)

Zoom in view of the first absorption dip. Around 25 nm shift can be observed. (e) Zoom in view of the second absorption dip. The shift is around 20 nm.

Light-Driven Dye Molecules Controlling Liquid Crystal Molecules to Reconfigure Plasmonic Absorbers

In this proof-of-concept study, we employ laser-induced birefringence change $[\Delta n]$ in azo-dye doped nematic liquid crystal. The active medium consists of the liquid crystal 5CB (pentyl-cyano-biphenyl) doped with ~4% of methyl-red dye dispersed onto the three-layered structure. Subsequent probing of the reflection property of the structure with s- and p-polarized light shows very small variation, indicating that the director axis of the liquid crystals are aligned homogeneously on the structure with director axis randomly distributed on the gold surfaces, i.e., the effective refractive index “seen” by the probing light is the isotropic value $n_{iso} \sim 1.61$ [Note: this value is for visible wavelength $\lambda = 0.5\mu\text{m}$, where $n_e = 1.742$ and $n_o = 1.547$; the refractive indices are lower in the near infrared regime $\lambda = 1\mu\text{m}$, [199] where $n_e \sim 1.63$ and $n_o \sim 1.50$ and $n_{iso} \sim 1.54$].

The experimental setup for optical tuning of the absorption dip is shown in Fig. 3-9(a), with an infrared microscope connecting to FTIR to collect the reflection spectrum at room temperature of 22 degrees. An argon laser ($\lambda = 514\text{nm}$) is used here as a pumping laser with its power tunable from 0 to 248 mW. The laser impinges obliquely on the sample so that its reflections are not collected by the microscope objective. When illuminated by the pumping light, several mechanisms could occur in the methyl-red doped nematic liquid crystal. [184] The most likely mechanism at work here is optically induced alignment of the methyl-red molecules [and therefore the liquid crystals molecules] towards the normal to the gold surface, i.e., the probe will “see” a lower refractive index value closer to the ordinary index value n_o . [200-202]

Fig. 3-9(b) shows the measurement of a sample with $a = 300$ nm and $b = 200$ nm. Note that with the liquid crystal overlayer, the two absorption dips are shifted by a considerable amount (from $1.11\ \mu\text{m}$ (in air) to $1.35\ \mu\text{m}$, and from $1.52\ \mu\text{m}$ (in air) to $1.7\ \mu\text{m}$, respectively). Because of the large index mismatch between the liquid crystal ($n_{iso} \sim 1.61$) and air ($n = 1.0$), the minima of the reflection bands are higher. When the refractive index of the liquid crystal is changed by an amount $\Delta n = -0.06$ [from 1.61 to 1.56], the simulation shows that a shift of around 30 nm. The corresponding experiment results are plotted in Fig. 3-9(c). We can clearly observe the change on absorption dips before and after the pumping light was applied, and the tuning is reversible and repeatable; in our experiment with low cw laser power illumination, the tuning speed is ~ 1 s. We also observe that the performance of plasmonic absorber has somewhat been compromised after introducing the liquid crystal and dye mixture, with one absorption dip giving 70% absorption compared to over 90% before the introduction of liquid crystals. Figures 3-9(d)

And 3(e) show a magnification of the two resonances from Fig. 3-9(c); the shifts are around 20–25 nm, which is in good agreement to the simulation results [shift of 30 nm]. By optimizing the geometry, or dye-concentration and utilizing other mechanism or liquid crystals to produce larger birefringence change, one could expect larger and faster tuning for the absorption dips.

Section Summary

I have demonstrated the feasibility of designing and constructing a light-driven reconfigurable dual-band plasmonic absorber comprised of gold nano-disks with an overlayer of photosensitive dye-doped liquid crystals. The tuning process is reversible and repeatable. Similar design concepts can be applied on other plasmonic devices where the tuning mechanism is light activated.

3.2. Transmissive and Reflective Ultra-Small Color Filters Based on Engineering Nanophotonic Nanostructures

Plasmonics provides the unique capability of manipulating light at sub-wavelength scales by using versatile nanostructures, such as cubes, [203-205] clusters, [206-208] shells, [209, 210] disks, [211-213] holes, [214, 215] rings, [216, 217] rods, [218-222] and particles with arbitrary shapes. [223-225] Many different kinds of plasmonic devices have been demonstrated so far, including modulators, [226] interferometers, [227] switches, [228, 229] polarizers, [230, 231] and absorbers. [150, 163, 232, 233] Color filters are an essential component in imaging sensors, color displays, digital cameras, and other related applications. Recently, interest in plasmon-assisted color filters has greatly increased due to their ultra-compact design, ultrahigh resolution, and convenient integration. So far, various plasmonic color filters, such as nanoslits with periodical grooves, [234] metal-insulator-metal stacks, [182, 235] and annular aperture arrays, [152, 236, 237] have been demonstrated. However, most efforts have been concentrated on transmission-mode color filters instead of reflection-mode ones. Very recently, researchers show that it is feasible to control colors using functional “intaglio/ bas-relief” [238] or nanodisks with backreflector [239] under reflection mode.

3.2.1. Reflective Plasmonic Color Filters Based on Lithographically Patterned Silver Nanorod Arrays

Metallic nanorod arrays with preferred alignment and periodicities are of particular importance for surface plasmon resonances and couplings, hence affecting photon flow accordingly. [240] However, it is very challenging to fabricate a dense nanorod array with ultra-small gaps and large aspect ratios using normal lift-off methods. In this Communication, we fabricate dense silver nanorod arrays with ultra-small gaps through the electron-beam lithography

(EBL) followed by ion milling. The effects of periodicity (p) and diameter/periodicity (d/p) ratio of the silver nanorod arrays on the plasmon resonance are investigated. By controlling their geometries, we show that such nanorod arrays are capable of tuning the plasmon resonance and further reflectively filtering out individual colors from a broadband light source. Hence, they can serve as reflective plasmonic color filters, which may find extensive applications ranging from color filtering to spectral imaging.

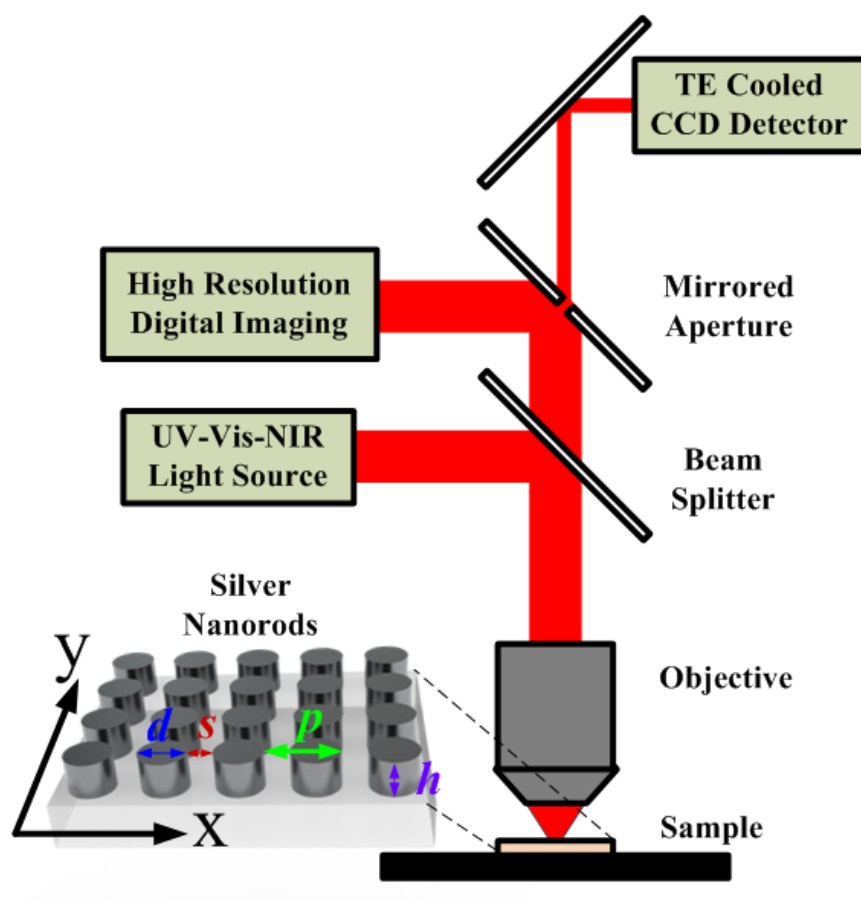


Figure 3-10. Schematic diagram of the color filter working under reflection mode.

Fabrication of Dense Silver Nanorod Arrays

An optically thick (180 nm) silver film was deposited on a quartz substrate with a 6 nm titanium adhesion layer by electron-beam evaporation. Prior to the film deposition, the substrate was cleaned with acetone followed by deionized water and blew dry with a nitrogen gun. To minimize the roughness introduced by deposition, a low evaporation rate was employed (less than 0.05 nm/s). Both titanium and silver films were deposited sequentially on the quartz substrate using an Edwards Auto 306 electron-beam evaporator at a base pressure of about 2×10^{-7} mbar. Negative resist NEB 22 with about 320 nm thickness was selected as the ion milling mask after EBL patterning and development. The area of each array was $\sim 8 \times 8 \mu\text{m}^2$. During ion milling (INTLVAC NANOQUEST), argon ions impinged upon the sample surface at an angle of 10° . The beam voltage was 300 V with 45 V accelerating voltage and 110 mA beam current. The total milling time was about 4 minutes with power stabilized around 156 W. Resist residue was removed by Microposit Remover 1165 after ion milling.

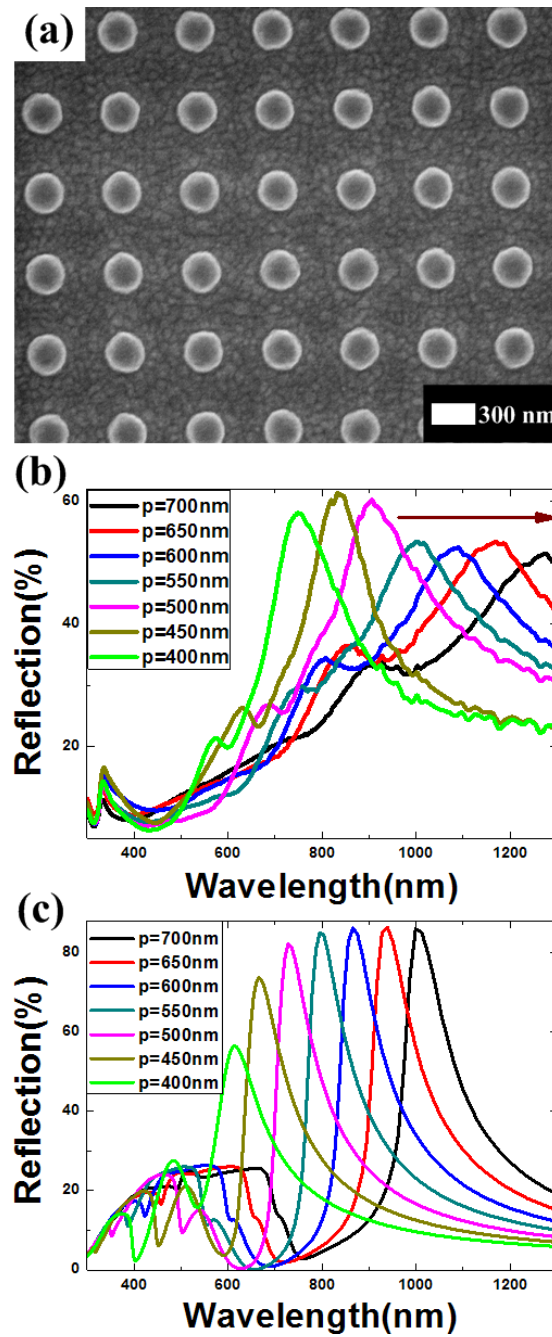


Figure 3-11. (a) SEM image showing the top view of a silver nanorod array with period $p = 550$ nm. (b) Measured and (c) calculated reflection spectra for nanorod arrays with periodicities from 400 nm to 700 nm. The arrow indicates increasing periodicities.

Optical Characterization

The optical response of the fabricated nanorods were measured using a UV-Vis-NIR microspectrometer (CRAIC QDI 2010TM) at normal incidence with a 75 W broadband xenon source. The incident light was focused onto the sample surface to have a detecting area of $7.1 \times 7.1 \mu\text{m}^2$ with a 36 \times objective lens. Reflection and transmission measurements were normalized with respect to an aluminum mirror and a bare quartz substrate, respectively.

FDTD Simulations

FDTD simulations were performed using Lumerical packages. The dispersion model of silver is based on Johnson and Christy [36] in the material library of the software. The simulation model was built based on the schematic shown in Fig. 3-10. One set of four silver nanorods was modeled with thickness ranging from 140 nm to 180 nm, providing a good agreement with experimental results. Note that a 6 nm titanium layer functioning as adhesion was applied on the quartz substrate. The dimension of the simulation area was set so as to allow two periods of the nanorod structure in the x-y plane and enough space for the light source and power monitors. Auto-nonuniform meshing with the finest meshes (0.25 nm minimum mesh step) was used to achieve the most accurate results. The auto-cutoff was set as 1×10^{-6} to ensure the convergence of the obtained results. Simulation time was set as 1000 μs with the step of 0.015 μs . The results usually converged before the simulation time ran out. The light source covered wavelengths ranging from 300 nm to 1300 nm with an increasing step of 2 nm. A power monitor was located 300 nm above the silver rods and 100 nm above the light source to collect reflected and scattered modes reaching the detecting region.

Results and Discussion

Fig. 3-10 illustrates the schematic view of the optical setup to characterize a reflective plasmonic color filter. Silver nanorod arrays with different periodicities were fabricated on a quartz substrate using standard EBL (Elionix ELS-7000) process followed by ion milling. Fig. 3-11(a) is the scanning electron microscope (SEM) image of a representative sample with the structural parameters: periodicity $p = 550$ nm in both x - and y -directions (see Fig. 3-10), rod diameter $d = 275$ nm ($d/p = 0.5$), and height $h = 180$ nm. Fig. 3-11(b) plots the measured reflection spectra of nanorod arrays with large inter-rod gaps ($s \geq 200$ nm) and varying periodicities from 400 nm ($d = 200$ nm) to 700 nm ($d = 350$ nm) in 50 nm increments (i.e., the d/p ratio was kept constant at 0.5). As can be seen from Fig. 2b, the reflection spectra can be tuned across the near infrared range with various array periodicities. A shift in resonance peaks from 750 nm to 1270 nm is observed when the periodicity is increased from 400 nm to 700 nm. The reflected intensity varies within 10% and the full-width at half-maximum (FWHM) decreases noticeably with smaller periodicities. The main resonance peaks become narrower in FWHM and higher in reflection with reduced periodicity, which could be attributed to stronger surface plasmon coupling in the cavities between adjacent nanorods. Fig. 3-11(c) plots the simulated reflection spectra based on the experimentally achieved structural data using the finite-difference time-domain (FDTD) method. There are slight differences in peak positions and intensities between measurements and simulations (see Fig. 3-11(b) and (c)), which could be caused by: (1) shape difference between the simulation model (perfect cylindrical rod) and the real sample (dome-like profile and non-circle shape); (2) surface oxidation of silver nanorods; (3) nonuniform silver materials properties caused by different grain sizes and distribution during metal deposition. Nevertheless, the simulation results show qualitative agreement with experiments and thus confirm our design concept.

To further investigate the impact of inter-rod gaps on the optical response of nanorods, we calculate the reflections in the visible range for nanorod arrays with constant periodicity $p = 400$ nm and varying inter-rod gaps and diameter sizes, as shown in Fig. 3-12. The peak intensity increases with larger d/p values, which is caused by the reduced distance between adjacent nanorods. As the gap size decreases down to several tens of nanometers, the converted surface plasmon waves from the incident light will not enter the structure because the ultrasmall gaps between nanorods allow nothing but zero plasmon modes, [79, 98] which cannot penetrate the nanorod layers of 180 nm. Most of the waves will only exist at the interface of air/rods and will be decoupled back into propagating electromagnetic waves as the reflection towards the incident direction. Apart from the intrinsic absorption and the damping loss of the surface plasmon waves, most of the input light energy reflects back as resonance peaks where the surface plasmon waves can be excited and the intensity will increase as the size of the gap decreases, which will be confirmed by the following experiments.

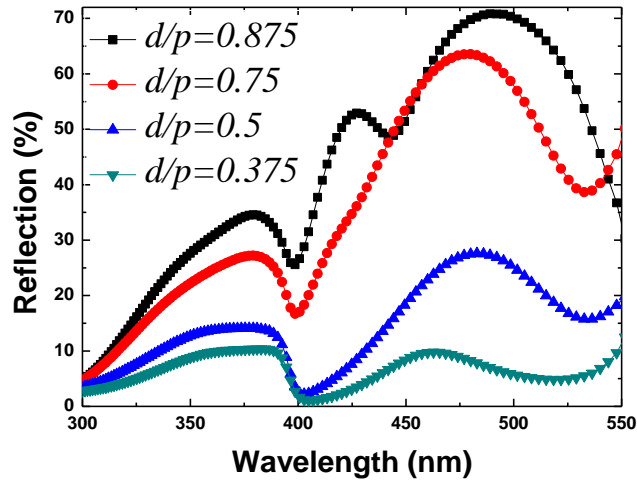


Fig. 3-12. Calculated reflection of nanorod arrays with constant periodicity $p = 400$ nm and varying inter-rod gaps and diameters corresponding to different d/p values ranging from 0.375 to 0.875.

To experimentally demonstrate the reflection-mode color filter, we fabricated plasmonic color filters according to the design with different d/p values and dramatically decreased inter-rod gaps. SEM images of nanorods with different inter-rod gaps are shown in Fig. 3-13. The silver rods have been milled through and very small (20-40 nm) inter-rod gaps can be clearly observed. Using nanorods with different periodicities from 540 nm (Fig. 3-13(a)) to 320 nm (Fig. 3-13(e)) in step size of 55 nm, we filtered individual colors out as shown in Fig. 3-14(a). From the top view of the rods (Fig. 3-13(f)), ultrasmall inter-rod gap size (~ 25 nm) can be clearly observed. The structural parameters of the arrays are summarized in Table 3-2. As expected, strong optical excitations in the visible band of the spectrum are observed. By changing the periodicity of the nanorod arrays, tuning of the resonance peak wavelengths between 480 nm (blue) to 630 nm (red) is achieved, as shown in Fig. 3-14(b). One can see that when the periodicity is 540 nm ($s = 40$ nm), a broad resonance is located at ~ 630 nm. When the periodicity is reduced to 485 nm ($s = 35$ nm), the resonance peak shifts to about 580 nm, exhibiting yellow color. Furthermore, when the periodicity is smaller than 430 nm, narrower resonance peaks are distinct and more reflected energies are observed due to stronger coupling in the small cavities, displaying as green, cyan and blue, respectively. Note that more intensity is reflected as the periodicity is decreased. The relatively large FWHM of the curve for the blue color compared to other spectra is due to fabrication imperfections. Some of the rods are touching each other (see Fig. 3-13(e)). Once the conductive contact between rods is established, the original surface charge distribution is broken and a different regime is formed. The conductive coupling between nanorods leads to redistribution of surface charges, resulting in the mergence of separate individual modes. Fig. 3-14(c) presents the measured transmission spectra which show relatively low intensities (less than 20% in the visible range), leading to a high efficiency reflective color filter.

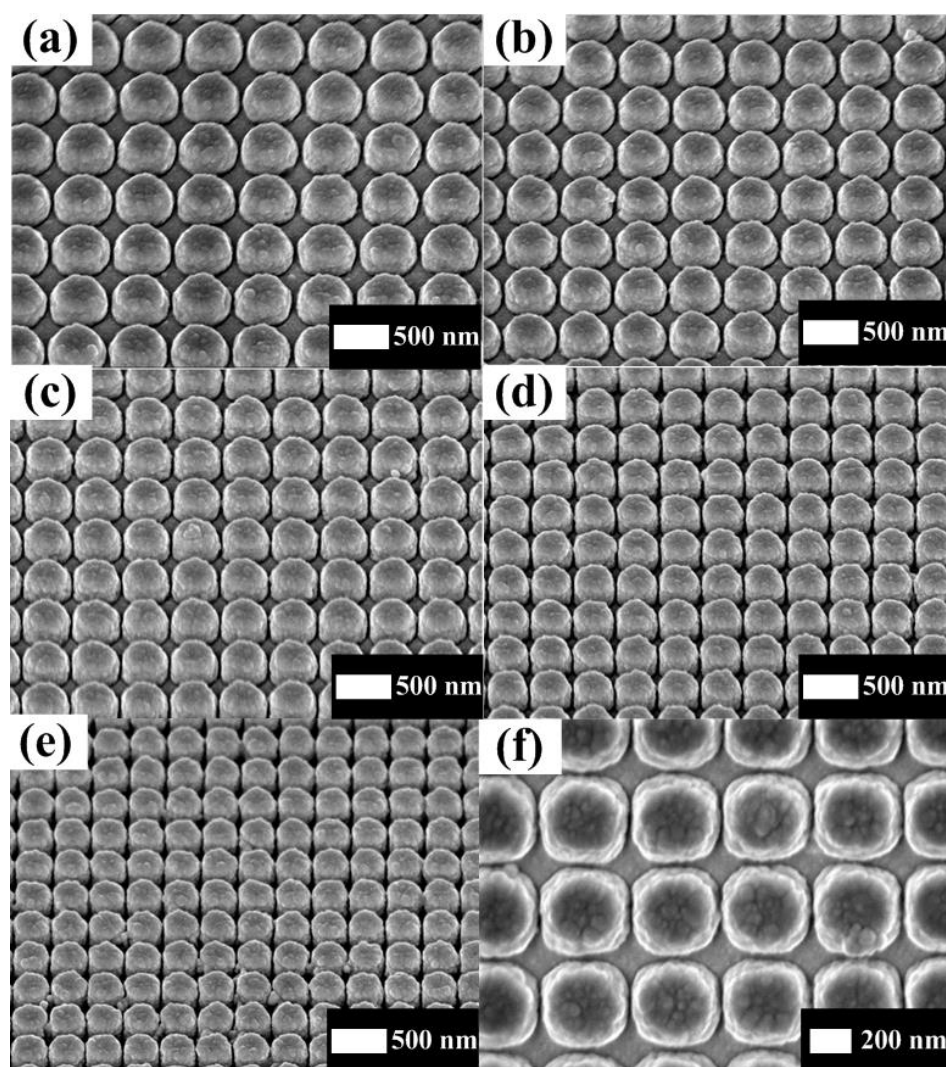


Figure 3-13. SEM images showing oblique views of dense nanorod arrays with different periodicities from (a) 540 nm to (e) 320 nm in step size of 55 nm. (f) Magnified top view of (d) with $p = 375$ nm and $d = 350$ nm.

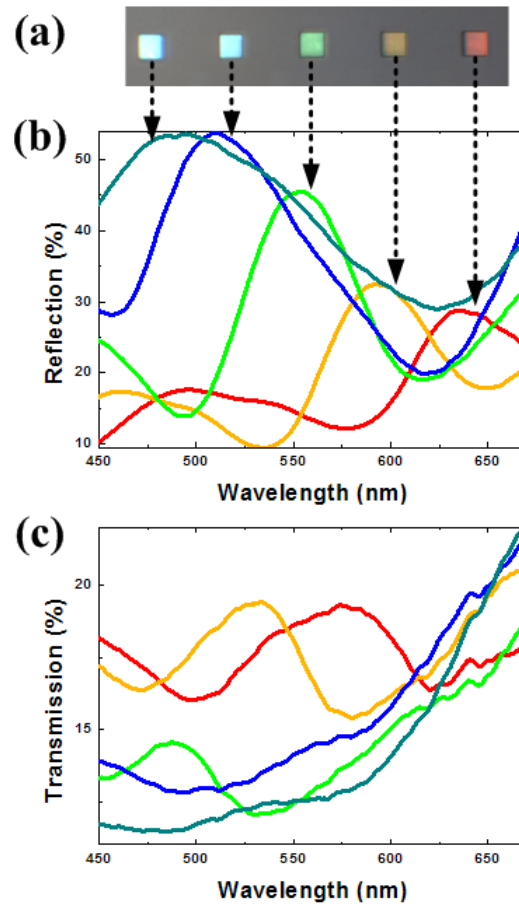


Figure 3-14. (a) Optical image showing the reflective colors from different silver nanorod arrays. Measured reflection (b) and transmission (c) spectra of the corresponding arrays as a function of wavelengths.

Table 3-2 Optimized parameters of the nanorod arrays and the corresponding reflected colors

Presented color	Periodicity(nm)	Rod diameter(nm)	Gap(nm)	d/p
Red	540	500	40	0.926
Yellow	485	450	35	0.928
Green	430	400	30	0.930
Cyan	375	350	25	0.933
Blue	320	300	20	0.938

Section Summary

I have demonstrated tuning of the plasmon resonance using dense plasmonic nanorod arrays. The optical response depends strongly on the periodicity of the arrays and the diameter/periodicity ratio. Effective tuning of surface plasmon resonance peaks is achieved across the near infrared range using plasmonic nanorod arrays with inter-rod gaps larger than 200 nm. The reflection peaks coincide with the plasmon resonance and nanorod arrays with different periodicities can act as color filters suitable for reflection measurement. Individual colors are demonstrated by using dense plasmonic nanorods with ultrasmall inter-rod gaps smaller than 40 nm and different array periodicities. A variety of applications such as sensing, imaging and displays can be readily realized by varying either the geometry or surrounding media of nanorods.

3.2.2. Annular Aperture Array Based Wavelength Selector in the Visible Range

In this section, we propose and experimentally demonstrate a wavelength selector based on the annular aperture geometry working in the visible range. The device is built with a configuration of coaxial aperture arrays in a gold film suitable for transmission measurement. We show effective and fine tuning of resonance peaks through precise geometric control of the aperture dimensions. Selective transmission through coaxial apertures of various sizes leads to continuous color tuning of transmitted electromagnetic waves, which may find great potential for application in high-definition displays, optical filters, ultrafast switching and bio-sensing.

Annular aperture arrays (AAAs) have generated extensive interest in the last decade because of their great potential as an important candidate for ultracompact optical devices since the extraordinary optical transmission (EOT) properties of such geometries were first reported by Baida and coworkers. [241] Early investigations of guiding light with wavelength much larger

than waveguide aperture using AAAs have shown several interesting phenomena and peculiar optical properties. [242-252] The influence of geometric and optical parameters on the EOT properties of AAAs has also been extensively studied. Compared with circular hole arrays, AAAs have shown additional functions related to the specific EOT characteristics. More importantly, the enhanced transmission observed in AAAs is due to the resonance of a guided mode through the apertures. Since the optical properties strongly depends on the structural parameters of the apertures, the cutoff wavelength of this guided mode can be effectively shifted to longer wavelengths when the outer and inner radii are approaching each other. [246] In addition, the small group velocity of the fundamental mode leads to important applications when the apertures are filled up with materials with high electro-optical coefficients (lithium niobate, for instance) in the AAA design. [253] Moreover, such coaxial structures can find application in composing single layer metamaterials in the visible range. [254-256]

Very high (up to 90%) transmission through AAAs has previously been achieved at visible frequencies (using AAAs fabricated in a silver film [257]) and this property, combined with the fact that the optical response of AAAs is also insensitive to the incident angle, [258, 259] makes the AAA structure a perfect candidate for high efficiency display and filtering devices. Here, we propose a simple yet effective method to filter individual colors using AAA-based geometries. Fabrication of apertures with features as small as 25 nm that show efficient color-filter functionality is demonstrated. An effective wavelength selecting function with AAAs that can be operated across the whole visible band and tuning of transmission resonance via structural control are also demonstrated. The optical response of the fabricated devices can be precisely tailored by shaping the aperture gap width, leading to opportunities for nanophotonics and optics.

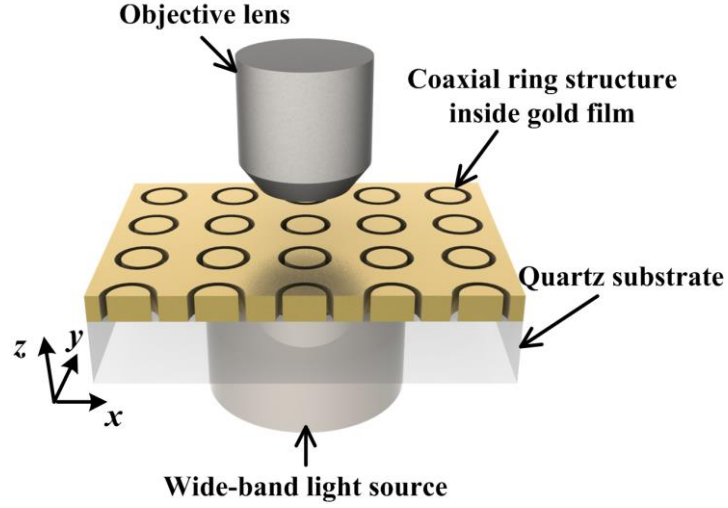


Figure 3-15. Schematic drawing of the proposed wavelength selector working under transmission measurement.

Plasmonic Resonance Peaks in Annular Aperture Arrays (AAAs)

A two dimensional AAA structure will have two transmission peaks, as demonstrated by different groups under different designs. [241-246, 250-252] The two transmission peaks are believed to be caused by cylindrical surface plasmons (CSP), and planar surface plasmons (PSP) [248, 250-252]. CSPs are affected by different geometrical design and the thickness of the metal film, while PSP is mainly related to the periods of the two dimensional gratings fabricated therein. The resonance peak is a direct result of Fabry-Perot resonance in a cylindrical resonance cavity formed by a metal film with finite thickness and two end-faces. For a finite metal film with thickness l , the design of desired the transmission peaks can be estimated by the following equation: [247]

$$l = \frac{m\pi - \varphi}{\beta} \quad (3-1)$$

Where l is the thickness of the metal film, m is the order of the Fabry-Perot resonance, φ and β represent phase of reflection and propagation constant, respectively. For the case where l is

constant, the propagation constant β varies with different annular aperture sizes and affects the reflection and transmission of the designed structure. Detailed discussion and analytical solutions of φ and β can be found in Ref. [247].

Design Principle

In our case, the target is to design a color filter which allows the transmission of a selected wavelength in the visible range for applications of true color or high-definition displays. Therefore, a metal film with fixed thickness is preferred. The periods of the two dimensional gratings also play an important role affecting the selective transmission. The enhanced transmission caused by two dimensional structures can be estimated as: [241]

$$\lambda = \frac{p_x p_y}{\sqrt{i^2 p_y^2 + j^2 p_x^2}} \sqrt{\frac{\epsilon_m \epsilon_d}{\epsilon_m + \epsilon_d}} \quad (3-2)$$

where p_x and p_y are periods along x and y direction, ϵ_m and ϵ_d represent the permittivities of metal and dielectrics, respectively. i and j are integers. The position of the transmission peaks caused by PSP is related to the periods of two dimensional gratings. Thus, it can be artificially tuned by changing the periods of the gratings. In our case, multiple transmission peaks within visible range will degrade the performance of the color selector. We try to minimize this effect by increasing the periods of the two-dimensional gratings so that the resonance peaks can be moved out of the visible range. With fixed metal thickness and grating periods, our color selector is achieved by tuning gaps of the gap of AAAs only.

Device Fabrication and Characterization

Figure 3-15 illustrates the schematic representation showing the fabricated elements and measurement system in this work. Using electron-beam evaporation, a 160 nm thick Au film over a 6 nm Ti adhesion layer was first deposited on a quartz substrate. Then the coaxial rings were milled using focused ion beam (FIB) etching. Each array comprises 9×9 rings occupying an area of $\sim 10 \times 10 \mu\text{m}^2$. The inner radii of the coaxial rings are fixed at 200 nm while the outer radii change from 230 nm to 290 nm in steps of 20 nm (corresponding to a 30-90 nm gap width). Measurements of the transmission properties of the fabricated nanostructures were carried out using a UV-Vis-NIR microspectrometer (CRAIC QDI 2010) at normal incidence. A 75 W broadband xenon lamp was used as the white light source with no polarization. Transmission measurements were normalized with respect to a bare quartz substrate. Figure 3-16(c) plots the measured transmission spectra of the four coaxial structures with gaps width of 30, 50, 70 and 90 nm. One can see that when the gap width is 90 nm, a broad resonance can be observed which is centered at ~ 580 nm. When the gap is narrowed to 70 nm, the peak position shifts to about 640 nm. Reducing the gap width to 50 and 30 nm, further red shifts can be realized and new resonance peaks are located at ~ 680 and 710 nm wavelengths, respectively. Note that the tuning of transmission peaks was realized via controlling the gap width of the ring apertures instead of the periodicity (fixed to 1200 nm) of the arrays. The transmission characteristics are mainly determined by the cylindrical surface plasmon (CSP) modes inside each gap cavity rather than by the periodicity.

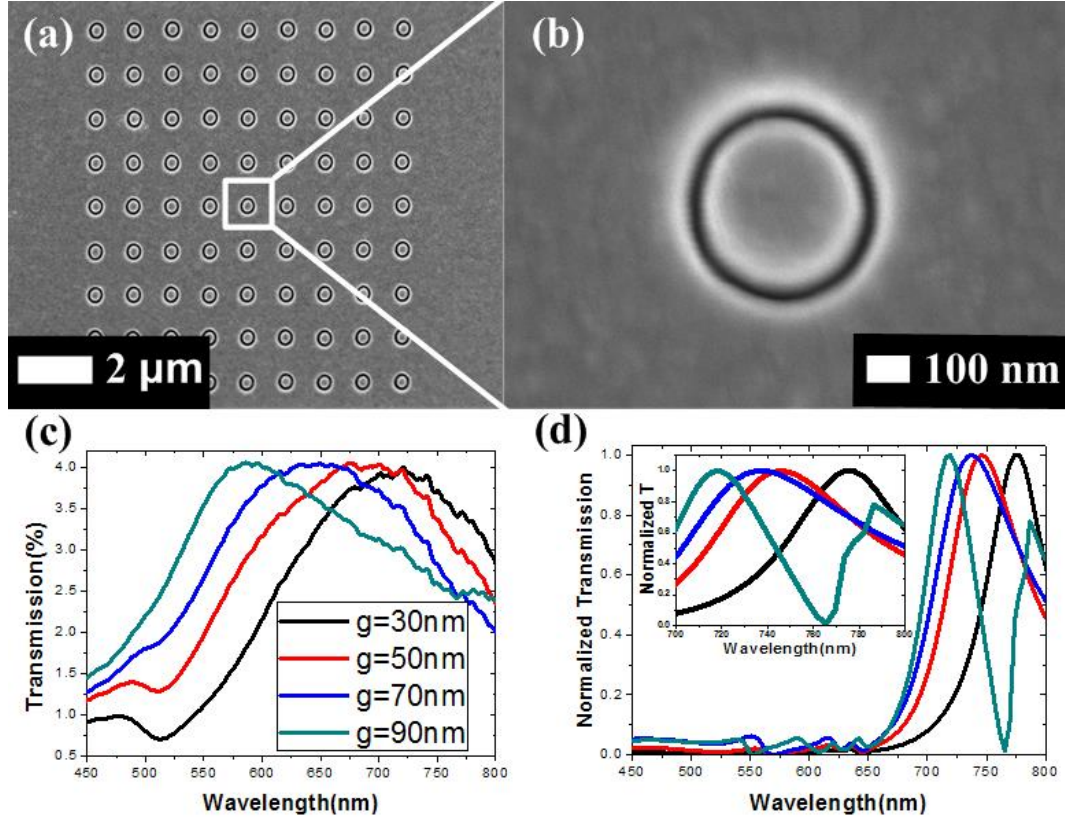


Figure 3-16. SEM images showing (a) overview of a fabricated 9 by 9 AAA and (b) magnified view of a single ring with 25 nm gap width. (c) Measured and (d) simulated transmission spectra of AAAs as a function of gap width. Simulated spectra are normalized for clarity. The apertures have fixed inner radius at 200 nm and varying outer radii from 225 nm to 270 nm in steps of 15 nm. The arrow in (c) indicates decreasing gap width. Inset of (d), magnified peak tops with 700-800 nm wavelength range to show the shift more clearly

Numerical Simulations

To further investigate the underlying physical principles related to the coaxial apertures, we carried out FDTD simulations to investigate the theoretical performance of the structures. The dispersion model of gold is based on Johnson and Christy model [36] in material library of the software. One set of four annular apertures are modeled inside a gold film with thickness of 160 nm, locating on top of a 6 nm Ti on the quartz substrate. The dimension of the simulation area is

2.4 $\mu\text{m} \times 2.4 \mu\text{m} \times 1 \mu\text{m}$, which allows two period of ring structure in x-y plane, and enough room for light sources and power monitors. We applied periodic boundary conditions for the x and y directions and perfectly matched layer (PML) boundary conditions for the z direction. Two polarized Gaussian beams with 90 degree phase difference were used to simulate the case of unpolarized light. The polarization directions are perpendicular to each other. The source covers wavelength range from 400 nm to 900 nm, with an increasing step of 2 nm. A power monitor was located 300 nm above the Au film to collect any transmission modes reaching the output region. The calculated transmission spectra are shown in Fig. 3-16(d). The position of the resonance peaks strongly depends on the diameter values, and similar results have been observed and discussed in Refs. [246] and Ref. [251]. Redshift of the resonance peaks can also be observed when decreasing the gap width. Note that the simulated transmission curves here are normalized to clearly show the shift trend of the transmission peaks. Compared to the measured spectra, the slightly smaller spectral width and red shift of the peak wavelength k_{max} observed in the simulations are due to the difference between the idealized features used in the simulations and imperfect structures of fabricated elements for testing, e.g., rough surfaces and tapered sidewalls caused by redeposition during FIB milling.

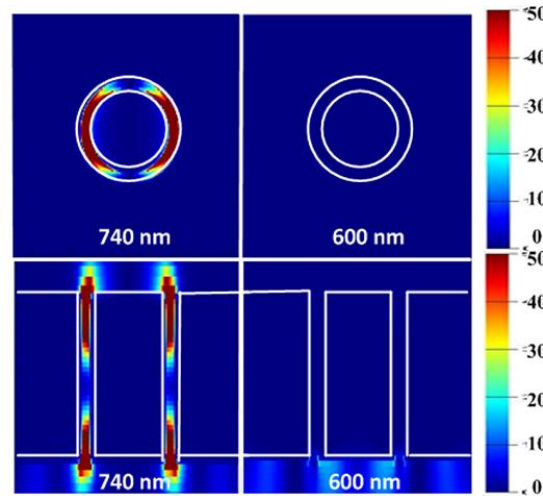


Figure 3-17. Top panel: top view; Bottom panel: cross sectional view of electric intensity distribution of a single ring with 55 nm gap width illuminated at 740 nm (λ_{\max}) and 600 nm (λ_{\min}), respectively.

The calculated electric field distributions are presented in Fig. 3-17. Strong confinement of light in the nanoring cavity is obvious, corresponding to the TE_{11} mode demonstrated in previous works. [244, 246] Top and cross-sectional views of the ring with 40 nm gap width at transmission maximum ($\lambda = 740$ nm) and transmission minimum ($\lambda = 600$ nm) confirm that the selective transmission is caused by the resonant ring cavities with various gap sizes.

In order to further tune the transmission response and finally filter individual colors out, the gap width was increased significantly. Scanning electron microscope (SEM) images of the fabricated structures are shown in Figs. 3-18(a) - (d). Using 40-, 80-, 120-, and 160-nm-wide ring apertures, colors of red, yellow, blue and cyan, respectively, are clearly observed in Fig. 3-18(e). As plotted in Fig. 3-18(f), resonances occur at different wavelengths when varying the gap width; peaks gradually shift to longer wavelengths as the rings are narrowed. Note that the resonance becomes broader due to a larger radiative damping in the nanoring cavities as the gap width is reduced. The relative weak intensity is mainly caused by high loss and attenuation over a long propagation distance (160 nm Au with 6 nm Ti in this work). For arrays with 160 nm and 120 nm gaps, the transmission peaks are located at about 480 nm and 500 nm, giving cyan and blue colors, respectively. When the gap aperture is narrowed down to 80 nm, the peak shifts to ~ 620 nm, exhibiting a yellow color. More light at around 690 nm is transmitted when the gap is further narrowed to only 40 nm, which results in a red color. A similar trend has been observed as in Fig. 3-16(c) that a blue shift of the transmission peaks occurs with the increasing the size of the annular aperture.

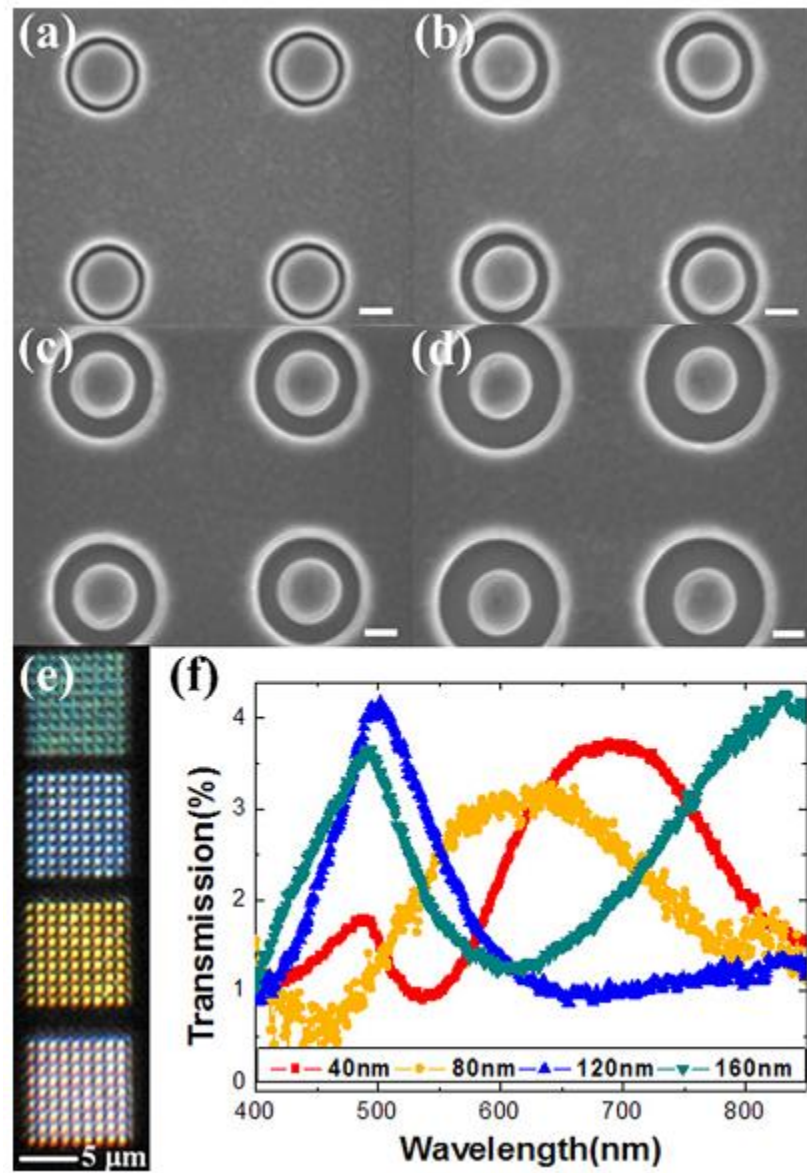


Figure 3-18. SEM images of the fabricated AAAs with (a) 40 nm, (b) 80 nm, (c) 120 nm, and (d) 160 nm gap width (outer radii equal to 240 nm, 280 nm, 320 nm, and 360 nm with 200 nm fixed inner radius). Scale bars are 200 nm. (e) Corresponding optical image presenting different colors. (f) Measured transmission spectra of the AAAs with different color outputs shown in (e).

Section Summary

I have demonstrated tuning of the plasmon resonance at visible frequencies using AAAs in a gold film. The optical response of a broadband light source through coaxial rings is

wavelength-selective and accurate control can be achieved to filter individual colors out. Owing to the structure's high symmetry, the device is polarization independent. FDTD calculations confirm the resonance dependence of selective transmission on gap width. Using coaxial apertures, fine tuning of plasmon modes through structural control and the color filtering function under transmission mode can be readily realized, opening up new opportunities for sensing and integrated optics.

3.3. Summary

In this section, I have discussed my works on designing and developing plasmonic absorbers and ultra-small plasmonic color pixels. We have our effort focused on expanding the working bands of the plasmonic absorber, allowing it to collect solar energy more effectively in near infrared range. With the help from the active medium of light switchable liquid crystal molecules, I have demonstrated dynamic tuning of the working range of the constructed plasmonic absorber. My works concerning the ultra-small plasmonic color pixel consist of two different designs targeting the applications under transmissive and reflective circumstances. The pixel size can be made down to less than 5 μm or even smaller. The passive plasmonic filter will work with any source to modulate broad band visible light to generate different colors.

Chapter 4

Engineering Plasmonics: Manipulating Light at Nanoscale using Active and Passive Plasmonic Devices

The researches on plasmonics revealed the many exciting and unique phenomena studying electromagnetic waves interacting with metal nanostructures. The knowledge acquired from those researches have laid foundations understanding the unique optical phenomena at nanoscale; more importantly, they provide us information and guidelines designing new types of plasmonic devices that utilize or alter the plasmonic responses to suit our needs for various applications, such as in optical networks and optical circuitries. My work of Engineering Plasmonics in this aspect, focused more on the designing and developing active and passive plasmonic device to actively modify the optical responses of constructed plasmonic devices, or passively control the light propagations at subwavelength scale. The light manipulation methods are based on existing knowledge on plasmonics and optical physics, with specific designing purposes and targeted applications on optical switches, optical transistors, optical router, etc. All the results will contribute to design a fully functional optical networks, and all the devices demonstrated are functional optical elements in this optical network for communications or computations.

This section consists of the information from my follow publications with necessary adaptations.

Mechanically Tuning the Localized Surface Plasmon Resonances of Gold Nanostructure Arrays, *ASME Journal of Nanotechnology in Engineering and Medicine*, Vol. 3, pp. 011007, 2012. [260]

High Contrast Modulation of Plasmonic Signals using Nanoscale Dual-Frequency Liquid Crystals, *Optics Express*, Vol. 19, pp. 15265-15274, 2011. [261]

Nanoscale Super-resolution Imaging via Metal-Dielectric Metamaterial Lens System, *Journal of Physics D: Applied Physics*, Vol. 44, pp. 41501, 2011. [262]

Beam Bending via Plasmonic Lenses, *Optics Express*, Vol. 18, pp. 23458-23465, 2010. [70]

4.1. Reconfigurable Plasmonic Devices via Active Mediums and Controlling Methods

Plasmonics integrates electromagnetic waves with metal nanostructures, allowing the manipulation of electromagnetic waves at the nanometer scale. [263] This provides the possibility for all-optical, ultra-high-speed computing or even the creation of networks and grids with much faster speeds and lower energy losses compared to current micro-electronic circuits. [70, 83, 152, 214, 264-267] It also provides a means to circumvent optical diffraction limits—which restrict the image resolution of the microscope—via the use of various metamaterials such as the superlens, [268, 269] hyperlens, [60, 270] and their derivatives. [262, 271] Active metamaterials consisting of both metal structures and an active medium such as liquid crystals [186, 191, 192, 213, 228, 261, 272, 273] or bi-stable molecules [187, 188, 190, 193, 274-279] have also been demonstrated as effective nano-scale optical modulators. Advanced fabrication techniques have equipped researchers with a powerful toolkit to make the active and passive photonic devices for optical network and circuitry experimentally possible. [174, 280-283]

Plasmonic device research has emerged aggressively as the need to combine electronic and photonic systems has become more acute [1-2]. Essential to future plasmonic circuits and systems is a means of reliable, scalable and energy efficient signal modulation. [70, 170, 284-286] Concepts for achieving modulation have focused on using an active material whose

properties can be changed by some form of stimulation. The speed of operation, energy consumption, modulation depth, device footprint, reliability, and cost are, in general, all determined by the choice of this material-stimulant combination. Static electric fields in combination with doped semiconducting thin films, [226] oxides, [227, 287] and photochromic molecules; [229] laser beams in combination with metal-semiconductor waveguides, [288] quantum dots, [289] and phase-changing materials; [290, 291] electric currents used for thermal activation of semiconductors; [292] and rotaxanes in combination with charged species [188] have all been demonstrated. As noted in [288], the limitations on modulator performance tend to result from the means of stimulation. For example, modulation by a static electric field is constrained by capacitance and thermal stimulation is constrained by thermal diffusivity.

4.1.1. Mechanically Tuning the Localized Surface Plasmon Resonances of Gold Nanostructure Arrays

Localized surface plasmon resonance (LSPR) [20, 179] is an important branch of plasmonics, linking metal nanoparticles with extraordinary optical responses. LSPR occurs when the oscillating frequency of incident light matches with the intrinsic electron resonance on the surface of a noble metal nanoparticle. Because absorbed light energy is used to drive the electron oscillations inside the metal nanostructure, LSPR is characterized by peaks in the absorption spectrum. The factors affecting LSPR include the size and shape of particles/holes, [293, 294] the distance between adjacent particles/holes, the thickness of the fabricated structures, and the environment surrounding the structures. [286, 295-300] Specific LSPR peaks can be obtained by engineering the metal nanostructures into different sizes and arrangements. [189] However, for each desired LSPR, a different corresponding geometry must be designed and fabricated. Active Plasmonics that can actively tune the LSPR after fabrication via flexible approaches utilizing

either mechanical stretching or thermal expansion to alter the nanostructure substrate, possesses a highly desirable feature preferred in plasmonic switches and bio-target identifiers. [170, 290, 301]

In the following discourse, we present two developments along this path. First, we describe a method to fabricate Au nanodisks onto an elastic polydimethylsiloxane (PDMS) substrate. Due to the weak bonding between Au and PDMS, the nanostructures must be fabricated onto an intermediate layer for sufficient adhesion. Second, by mechanically stretching the PDMS substrate, above which sit the Au-patterned nanostructures, we observed a real-time tuning of the plasmonic resonance due to the varying distance between adjacent nanodisks. Our design utilizes low-cost nanofabrication techniques and can find application in plasmonic sensing, [302] optical imaging, optical memory elements, and energy harvesting. [149]

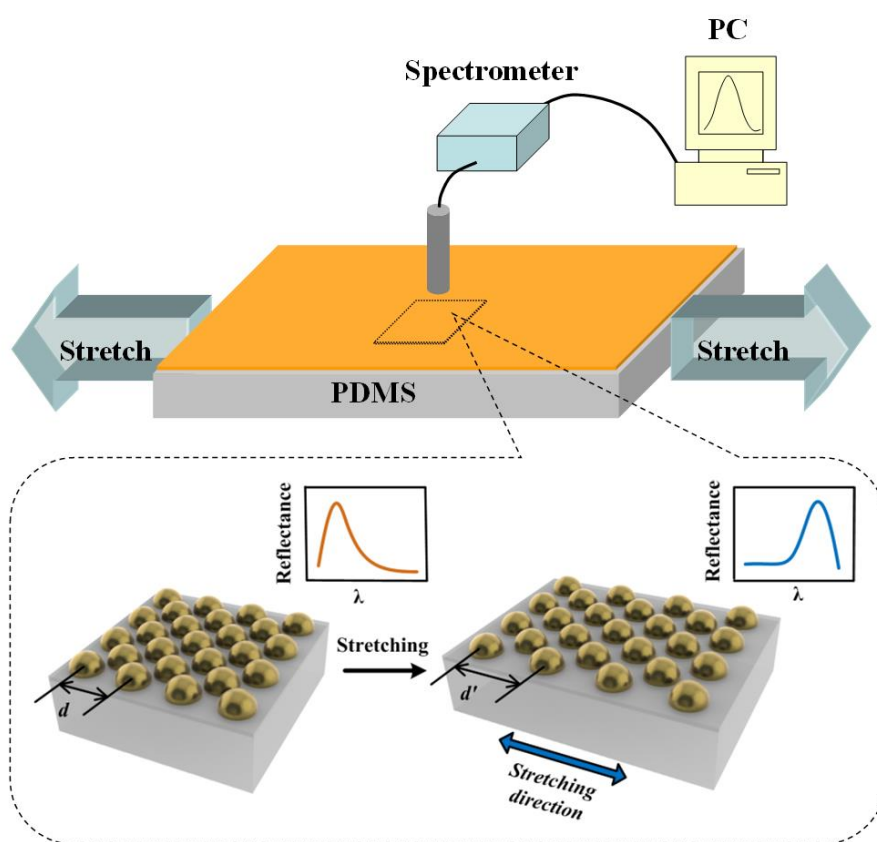


Figure 4-1. Schematic of the experimental setup. The active tuning of LSPR of the Au nanodisk arrays is achieved by mechanically stretching the sample.

Experimental details

A schematic of the working mechanism is shown in Fig. 4-1. In order to dynamically tune the LSPR of an Au nanostructure array, we fabricated the array on the resilient, mechanically limber substrate: PDMS. However, the deposition of Au directly on PDMS is not favorable as the two only weakly interact. To overcome this challenge, we used a monolayer self-assembly process based on a standard Langmuir-Blodgett [303] followed by standard etching and film deposition procedures.

The PDMS substrate was prepared as follows: First, a silicon wafer with smooth surfaces was cleaned and coated with 1H, 1H, 2H, 2H-perfluorooctyltrichlorosilane (Sigma-Aldrich) to reduce the surface energy. This treatment protects the PDMS from deformation during the detachment process and significantly reduces the surface roughness. Next, Sylgard® 184 Silicone Elastomer base and curing agent (Dow Corning, Midland, MI) was mixed in a 10:1 weight ratio and applied to the pretreated silicon wafer. The mixture was then cured at 70°C for 20 min. Once cured, it was cut and peeled away from the silicon wafer. Finally, a zapping process was initiated to create charges on the PDMS surfaces to increase the bonding between the PDMS and dielectric materials.

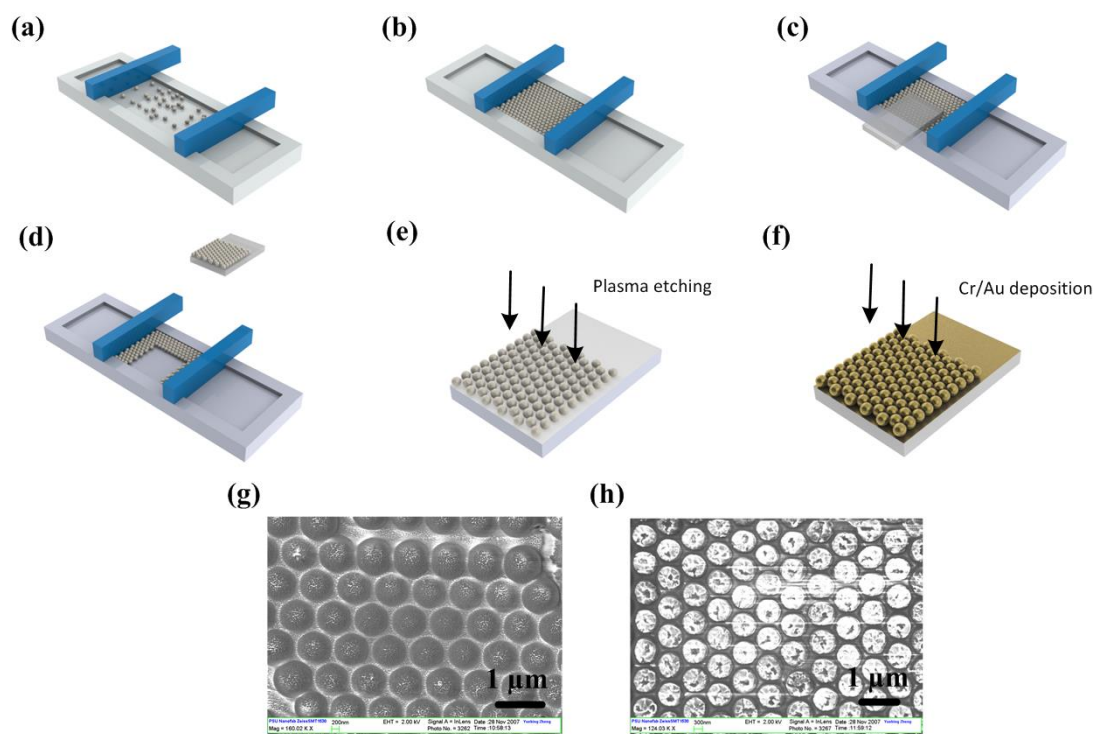


Figure 4-2. Procedures of fabricating Au nanostructure arrays on a PDMS substrate using the Langmuir-Blodgett technique, deposition, and etching: (a) Disperse PS nanospheres in DI water. (b) Compress the squeeze bars to form a compact monolayer of PS nanospheres. (c) Attach a smooth PDMS substrate to the monolayer of nanospheres. (d) The bonding force between PS nanospheres and PDMS substrate helps to transfer the nanosphere arrays onto the surface of PDMS substrate. (e) Reshape nanospheres using plasma etching. (f) Deposit Cr/Au on top of the nanosphere arrays. SEM images of the sample after step (e) and (f) are shown in (g) and (h), respectively.

Polystyrene (PS) nanospheres with a mean diameter of $1.05\ \mu\text{m}$ were obtained in solution (10 wt%; Bangs Laboratories, Inc.) and diluted to 1 wt% with ethanol. The diluted suspension was pulled into a pre-cleaned Langmuir-Blodgett deposition trough (KSV NIMA) filled with deionized water. Upon the addition of several microliters of sodium dodecyl sulfate, the PS nanospheres were dispersed on the water surface (Fig. 4-2(a)). The barriers of the trough were brought close together to form a monolayer of PS nanospheres (Fig. 4-2(b)). The PDMS slab was then placed onto the patterned monolayer to directly transfer the PS nanosphere array from the liquid surface to the pretreated PDMS surface (Fig. 4-2(c, d)). A plasma etching process was

applied to flatten and separate the transferred PS nanospheres. As shown in Fig. 4-2(g), the diameter of the PS nanospheres shrinks from 1.05 μm to 800 nm after etching, leaving the spacing between adjacent nanospheres around 250 nm. Finally, a 2-nm-thick adhesion layer of Cr and a 40-nm-thick layer of Au were sputtered onto the reshaped nanospheres to form the Au nanostructure arrays. Figure 4-2(h) shows the SEM image of the sample after Cr/Au deposition. The hexagonal array has a period of 1.05 μm and a spacing of ~ 165 nm. The observed structures are nanonipple-like rather than perfectly disk-shaped because the bead support did not provide a flat surface for the deposition after etching. However, this does not affect our concept of plasmonic tuning via PDMS substrate stretching, and the shape effect on plasmonic resonance is not the focus of the reported work. Thus, we made a subjective decision to approximate the nanonipples to nanodisks for the simplicity of simulation and analysis, and our approximations have been confirmed and supported in both simulation and experiment.

The experimental setup is schematically illustrated in Fig. 4-1. The dimensions of the sample that we used in the experiment are around 1 cm by 1 cm, cutting from a large sample area. The sample was affixed to a caliper with a stretching range of 0 to 2000 μm with a precision of 10 μm . An ultraviolet-visible-infrared spectrometer (Ocean Optics Co., HR4000) was operated in reflection mode to measure the reflectance spectrum of the Au nanostructure arrays. Both the source and detector optical fibers were mounted normal to the sample. The dynamic tuning of the LSPRs from the Au nanostructure arrays was then monitored over a spectral range of 400–900 nm, upon sample stretching.

Results and Discussion

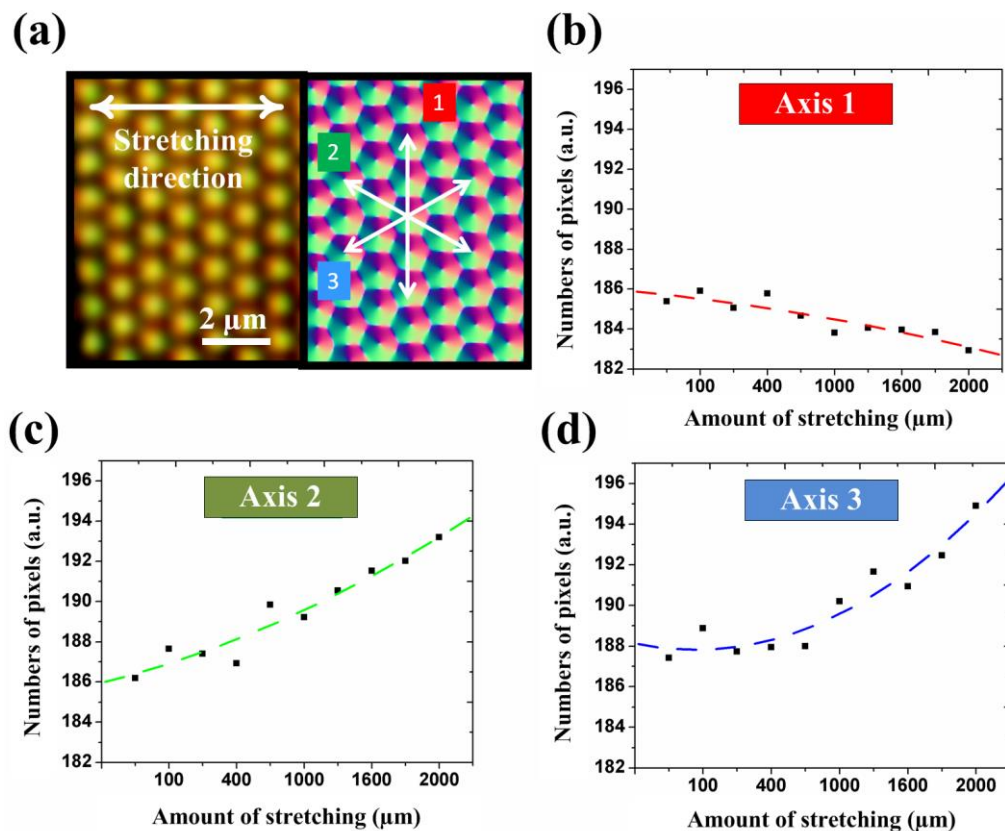


Figure 4-3. (a) Microscopic image of Au nanodisk array immobilized on a PDMS substrate. Three axes of the hexagonal array are marked for measuring the geometry change upon stretching. (b–d) The measured change in array period along three axes.

Fig. 4-3(a) shows original microscopic images of a relaxed Au nanodisk array, and a processed image to mark the lattice boundaries of adjacent nanodisks. The arrowed lines denote the three axes of the hexagonally arranged array, and the horizontal line indicates the stretch direction. The maximum stretch is 2000 μm , and the change in period along the three axes of the hexagonal array is plotted in Fig. 4-3(b–d), respectively. The change in period was measured from captured microscopic images and its value was averaged over several locations. One point that must be noted is that the distance between adjacent nanodisks changed during the stretching

process, yet the nanodisks maintained the same shape as in their relaxed state; this is caused by the intermediate PS sphere layer separating the gold nanostructures and the PDMS substrate. The gold nanostructures adhere to the PS spheres rather than attach to the PDMS layer directly, and thus the gold structures will not change their shapes unless the stretching force from the PDMS substrate is strong enough to tear the PS spheres, which is unlikely to happen in our case.

Upon being stretched, axes 2 and 3 are elongated, while axis 1 is condensed. It can be seen from figure 3 that the relation between the stretch amplitude and period shift is nearly linear along all axes. The maximum rate of change of the period along axes 2 and 3 is $\sim 4.3\%$, and -1.6% for axis 1. Poisson's ratio (ν) was calculated from the geometric relation between the axes (0.45), which accurately matches the intrinsic material property of PDMS ($\nu=0.5$). Finally, the angle between axes 1 and 2 increases from 60° to 62° upon maximum stretching, while the angle between axes 2 and 3 decreases to 56° .

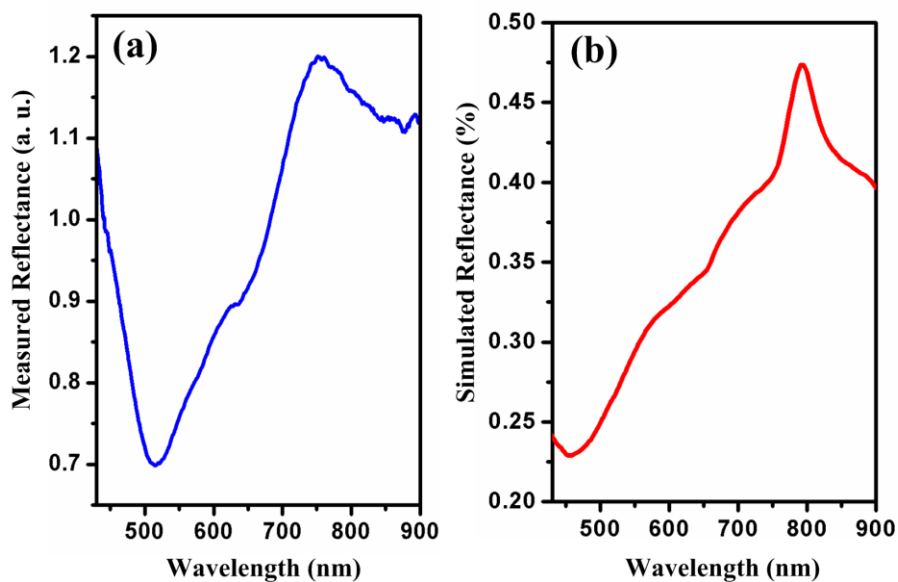


Figure 4-4. Measured (a) and FDTD-simulated (b) LSPR reflectance spectrum of the Au nanodisk arrays immobilized on a PDMS substrate in the relaxed state

The LSPR properties of the Au nanodisk arrays, which were immobilized onto the PDMS substrate, were studied by taking the arrays' reflectance spectrum. Figure 4-4(a) shows the measured reflectance spectrum of the relaxed Au nanodisk arrays. To further understand the spectrum, a numerical calculation was conducted using commercial software (Lumerical FDTD) to simulate a perfect hexagonal array of Au nanodisks standing on a dielectric substrate. The period, diameter, and thickness of the Au nanodisks were 1050 nm, 800 nm, and 40 nm, respectively. The dielectric constant of Au was obtained from a fit to the Johnson & Christy data. [36] An unpolarized, broadband light source was set normal to the substrate. The reflectance spectrum is shown in Fig. 4-4(b) (modeled without Cr adhesion layer).

The reflectance minimum is related to intrinsic absorption and transmission of the incident light by the Au, while the peak indicates minimal coupling between the incident light and the localized surface plasmons. The experiment result closely matched the simulation and confirmed that the tightly packed Au nanoparticle arrays have been formed as expected.

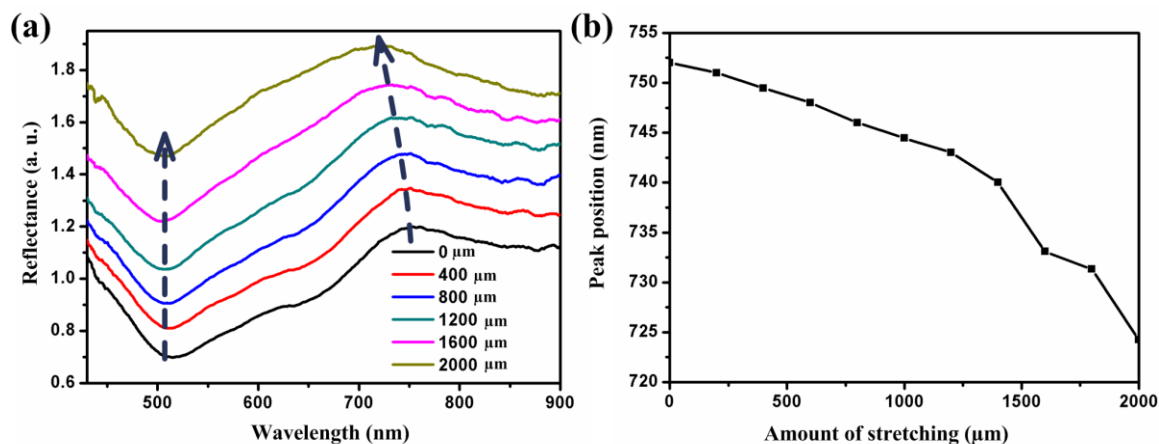


Figure 4-5. (a) Extinction spectra recorded from the Au nanodisk arrays immobilized on a PDMS substrate undergoing various levels of stretching. A blueshift of reflectance peak wavelength is observed. (b) Shift of reflectance peak wavelength as a function of amount of stretch. A tunable reflectance peak shift up to 30 nm is achieved.

Fig. 4-5(a) shows the reflectance spectra of Au nanodisk arrays immobilized on a PDMS substrate undergoing various levels of stretching. The stretching neither broadened nor decreased the intensity of the LSPR spectra. There is no obvious shift in the spectral dip since it represents the intrinsic transmission and absorption of Au and is not dependent on geometry. The reflectance peak, however, exhibits a clear blueshift proportional to the amount of stretch, which is consistent with the observation in Ref. [304]. The reflectance peak shift versus stretch magnitude is plotted in Fig. 4-5(b); the plot shows a maximum peak shift of 30 nm (from 752 nm in the relaxed state to 722 nm at maximum stretch). The peak shift is reversible, i.e., the peak wavelength moves back to 752 nm when the sample is released, and the tuning of the peak wavelength becomes uniform across the sample.

The blueshift of the reflectance peak wavelength is the result of the change in Au nanodisk array geometry. LSPR in nanoparticle arrays is highly dependent on coupling between adjacent particles, which in-turn, strongly depends on the inter-particle distance. The sample was stretched in only one direction, but due to Poisson's effect, the size in the relaxed direction was decreased while the period in the other two directions was increased. The spacing of the Au nanodisk arrays was not homogeneously changed; however, the effective inter-particle distance increased as the sample was stretched, leading to less influence from electron coupling between adjacent Au nanodisks as well as a blue-shift in the reflectance peak.

Section Summary

I developed a simple, inexpensive method to fabricate patterned Au nanostructures on a PDMS substrate: The plasmonic resonance of the Au nanostructures can be actively controlled by stretching the PDMS substrate. The stretching increases the distance between adjacent Au

nanostructures, leading to a shift in their plasmonic resonance. The shift is repeatable, reversible, and has potential applications in LSPR sensing, Raman sensing, and coupled resonance studies.

4.1.2. High-Contrast Modulation of Nanoplasmonic Signals using Nanoscale Dual-Frequency Liquid Crystals

Liquid crystals can serve as excellent active nanomaterials for plasmonic modulators, due to their large and controllable birefringence. In addition, they offer reliability, robustness, long lifetime, and low costs. [184, 272, 305-309] While the response time of liquid crystals is usually long, causing the efficiencies of modulators that employ liquid crystals to be low, the response time does decrease with cell thickness. Furthermore, new concepts, like polymer-stabilized liquid crystals, and flow effects in microfluidic structures, have been proposed to further decrease the response time. [310, 311] In this work, we demonstrate the feasibility of nanoscale, high contrast modulation of surface plasmon polaritons (SPP) propagating along an interface between silver and dual-frequency liquid crystals (DFLC). Our results indicate that the proposed DF-LC-based plasmonic modulation can achieve over 15 dB modulation depth with femtojoule activation energy. The ultimate speed of modulation is limited by the sub-micron thick nematic layer, which is on the order of 100 microseconds.

Principles and design

Figure 4-6 shows the schematic of the DF-LC-based nanoplasmonic modulator. Such DF-LCs can change the sign of dielectric anisotropy either from positive to negative, or from negative to positive, when the frequency of the applied field changes. A groove-slit geometry defines the basis of the design. The operating principles of our DF-LC-enabled nanoplasmonic modulator consist of (1) SPP excitation by diffraction through a slit on silver film; (2) phase

modulation of SPP signal by electro-optic DFLC; and (3) interference of SPP signal produced by input beam with optical pump beam at the slit. In other words, the input optical beam at the groove excites a SPP that propagates over a region embedded with DFLC. Then, the pump beam interferes with the SPP at the slit and the output intensity is measured at an observation point. Contrast between output signals is achieved by varying the dielectric anisotropy of the DFLC, which is accomplished through an applied voltage. Our investigation is focused on measuring the output as a function of groove-slit separation distance.

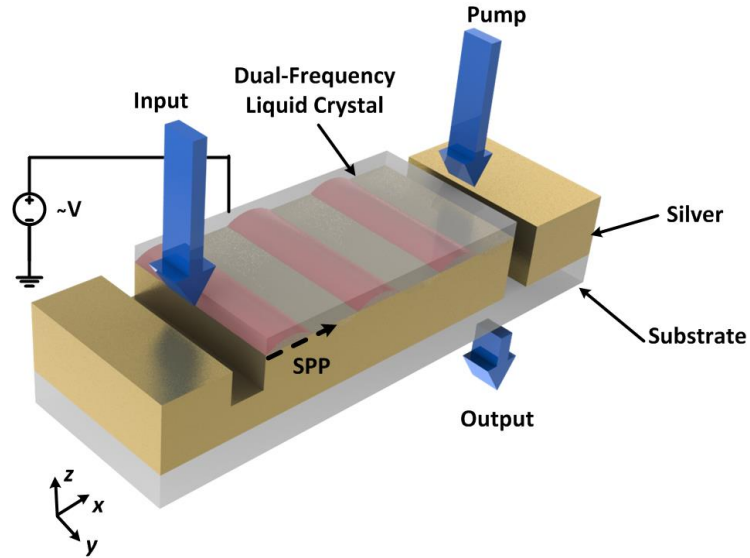


Figure 4-6. Schematic of the DFLC-based nanoplasmonic modulator. An SPP is excited through diffraction-mediated transfer of momentum from the input. The SPP wave (shown here in pink) then propagates through the DFLCs, which exhibits either an ordinary or extraordinary refractive index, depending on the frequency of an applied voltage. Thus, the signal enters the interference stage at a phase that is dependent on the path length traveled and refractive index of the DFLC. Finally, a pump beam creates an interference pattern with the plasmonic signal, which is read as output information.

The conversion of propagating electromagnetic (EM) waves into SPP waves is achieved through the matching of the momentum of the two waves. In our case, we use a groove with sharp edges to diffract the incident EM waves to generate SPP waves. The wave vector of the generated SPP modes is determined by the permittivity of the metal and dielectric, following the equation

$$k_{spp} = k_0 \sqrt{\frac{\epsilon_m \epsilon_d}{\epsilon_m + \epsilon_d}} \quad (4-1)$$

where ϵ_m denotes the permittivity of the metal, ϵ_d represents the permittivity of the dielectric, and k_0 and k_{spp} are wave vectors of the incident EM and SPP waves, respectively. Based on Eq. (4-1) and the relation $n^2 = \epsilon$ for non-magnetic materials, where n is the refractive index, we can see that the SPP wave vector changes with the refractive index.

In this work, the dielectric material is DFLC. [198, 312-315] This DFLC material, such as MLC-2048(Merck) used in Ref. [228] has a positive sign of dielectric anisotropy $\Delta\epsilon = \epsilon_{\parallel} - \epsilon_{\perp} > 0$, for frequencies f of the applied electric field smaller than the crossover frequency f_c and has a negative sign, $\Delta\epsilon < 0$, when $f > f_c$. Here ϵ_{\parallel} and ϵ_{\perp} are the dielectric permittivities of the DFLCs in the directions parallel and perpendicular to the LC director, respectively. For LCs with $\Delta\epsilon > 0$, the director prefers to align toward the electric field direction, then the light wave travelling through LCs will see an ordinary refractive index denoted as n_o ; while for $\Delta\epsilon < 0$, LC realign perpendicularly to the field, and the light waves see an extraordinary refractive index, denoted as n_e .

If an SPP wave propagates through the LC with n_o , and a second wave excited by the same light source at a later time travels through the LC with n_e , the two waves will have a phase difference with respect to each other by an amount that depends on the SPP wavelength, the length of the LC cell, and $\Delta n (= n_e - n_o)$. Because the two waves have a phase difference, their interaction with a pump beam will generate two distinct transmission signals. The phase modulation of the DFLC can be designed such that the transmission signals achieve a desired contrast that can be observed in the output signals. For applications in logic or ON/OFF switching, an amplitude transmission contrast as high as possible is desired, with signal A

approximating an intensity equal to that of the input excitation source, and signal B approaching zero intensity. We call M , the modulation depth, defined as

$$M = 10 \log_{10} \left(\frac{I_A}{I_B} \right) = 10 \log_{10} \left(\frac{n_B^2 \frac{H_{y\,pk,A}^2}{H_{y\,pk,B}^2}}{n_A^2} \right) \quad (4-2)$$

where I is the irradiance, $H_{y\,pk}$ is the peak amplitude of the y-component of the H field, and the subscripts A and B refer to signals A and B, respectively. Given that we control the incident free-space wavelengths from the optical excitation and pump sources, the refractive indices of both states of the DFLC, and the optical path lengths through the entire system, we can select these parameters to achieve a useful modulation depth, M .

The phases corresponding to the SPP modes propagating along the LC-silver interface are

$$\phi_o = 2\pi \left(\frac{z_1}{\lambda_0} + \frac{z_2 n_o}{\lambda_0} + \frac{D}{\lambda_{spp,o}} \right) + C_{1,o} + C_{2,o} \quad (4-3)$$

$$\phi_e = 2\pi \left(\frac{z_1}{\lambda_0} + \frac{z_2 n_e}{\lambda_0} + \frac{D}{\lambda_{spp,e}} \right) + C_{1,e} + C_{2,e} \quad (4-4)$$

where the indices o and e denote the SPP travelling through LC of n_o , LC of n_e , respectively; z_1 is the distance between the input source and LC-air interface, and z_2 is the distance between the LC-air interface and the LC-silver interface. The two last terms in Eq. (4-3, 4-4) represent the phase changes that occur through the light-SPP coupling and SPP-light decoupling.

The phase corresponding to the pump beam can be considered a slit mode, as described in Ref. [316]. Interference between the SPP modes propagating along the LC-silver interface and the pump mode will occur prior to the excitation of the slit mode. Therefore, for the phase of the pump at the plane of interference, we have

$$\phi_p = \frac{2\pi}{\lambda_0} (z_1 + z_2) \quad (4-5)$$

Phase changes that occur at the entrance interface, $\Delta\phi_1$, and exit interface, $\Delta\phi_2$, of the slit are

$$\Delta\phi_1 = \arg \left[\frac{n_1 - \frac{\beta}{k_0}}{n_1 + \frac{\beta}{k_0}} \right] \quad (4-6)$$

$$\Delta\phi_2 = \arg \left[\frac{\frac{\beta}{k_0} - n_2}{\frac{\beta}{k_0} + n_2} \right] \quad (4-7)$$

where n_1 and n_2 are the refractive indices of the medium at entrance and exit to the slit, respectively, and β is the complex-valued propagation constant of the slit mode. Replacing β with the complex valued SPP wave vector, k_{spp} , we can relate the coupling and decoupling constants of Eq. (4-3, 4-4) to Eq. (4-6, 4-7) by the relation

$$|C_1 - C_2| = |\Delta\phi_1 - \Delta\phi_2| \quad (4-8)$$

For the case of trivial losses, $\text{Im}[k_{spp}] \rightarrow 0$, and $\Delta\phi_{1,2} \rightarrow \frac{\pi}{2}$. Thus $|C_1 - C_2| \rightarrow 0$.

Finally, we consider the interference of the SPP modes propagating along the LC-silver interface with the pump mode just before the entrance to the slit and define the phase differences at the slit entrance as

$$\Delta\phi_o = |\phi_o - \phi_p| \quad (4-9)$$

$$\Delta\phi_e = |\phi_e - \phi_p| \quad (4-10)$$

Simulation and discussion

To better investigate the working mechanism and performance of our DFLC-based nanoplasmonic modulator, here we provide simulation results from a commercial software package that uses the finite-difference time domain method (Opti-FDTD). We used the built-in Drude approximation for the parameters of silver and assigned the refractive indices of DFLC manually. Gaussian beams of incident wavelength 514 nm, half width of 250 nm, and field

amplitude of 1 A m^{-1} were used for both the input and pump sources. Perfectly matched layer boundary conditions were used with a mesh size of $x = y = 5 \text{ nm}$ and $1.0\text{e}5$ time-steps of $\sim 1.11\text{e}^{-17}$ s.

The geometry of our nanoplasmonic modulator is detailed in Fig. 4-7(a). Both the groove and slit are 100 nm wide, while their separation distance, D , is on the order of hundreds of nanometers. A 200 nm thick layer of DFLC spans the separation distance. The thickness of the silver layer is 360 nm . The refractive indices of the DFLC were chosen as $n_o = 1.49$ and $n_e = 1.75$. The input excitation and pump sources were directed upon the center points of the groove and slit, respectively. Due to the significant difference between slit width and incident wavelength, SPP waves are excited at the sharp edges of the slit and propagate along the metal-dielectric interface of the silver and LC. For simplicity, the propagation loss of SPP waves over D is set to zero. After the SPP waves reach the slit, they interfere with the pump beam. The pump beam excites SPP slit modes, as described in [316]. The modulation is a direct result of constructive and destructive interference of two SPP modes with the pump beam slit modes. Figures 4-7(b) and 4-7(c) show the nanoplasmonic modulator during its ON and OFF states, respectively, indicated by the transmitted light signal and near-zero transmission at the outlet of the slit.

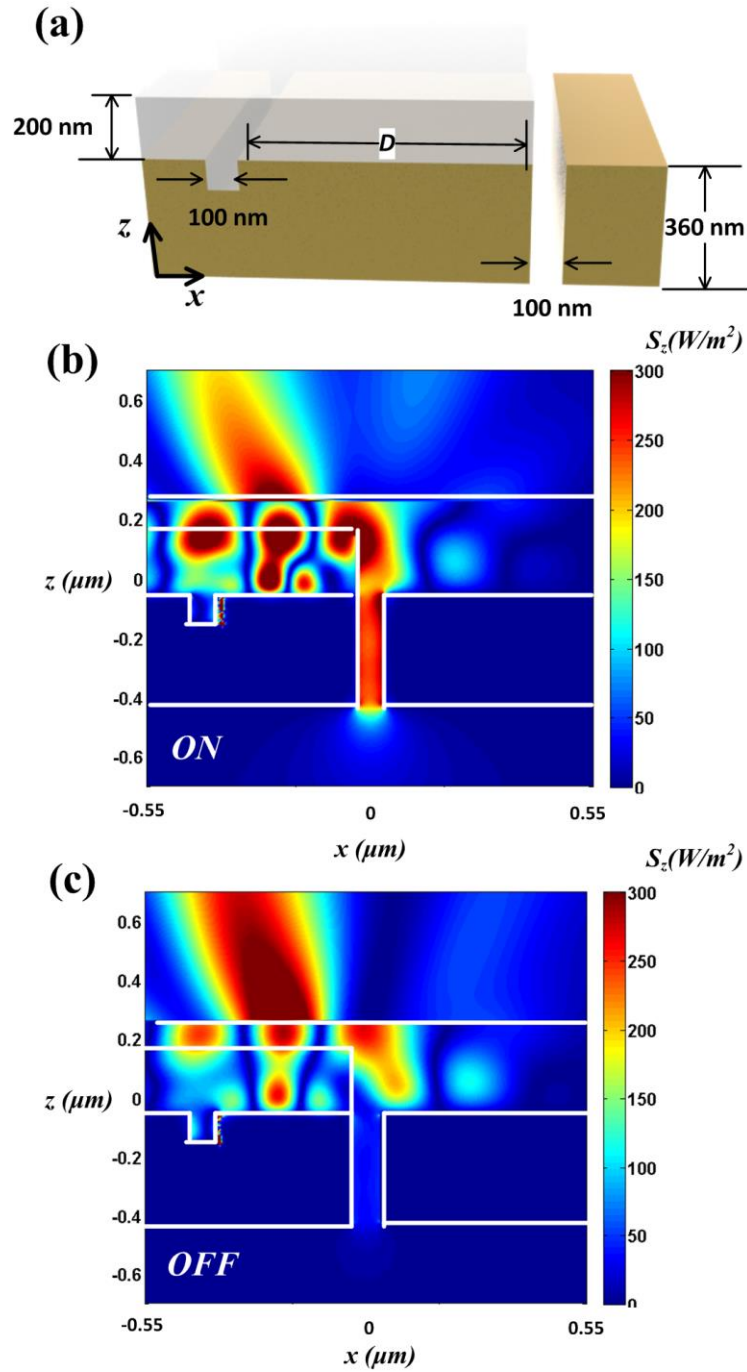


Figure 4-7. (a) Detailed geometry of the DFLC-enabled plasmonic modulator. The groove-slit separation distance is denoted as D , and is used as a parameter to find a usable modulation depth, while maintaining nanoscopic dimensions. The 200 nm gray layer represents the DFLC, whereas the tan structure is silver, modeled according to the Drude approximation. The entire structure is surrounded by air. (b) Field intensity plots for 1-groove, 1-slit device in the (b) ON state and (c)

OFF state. The relative magnitude of the Poynting vector is shown against the two-dimensional geometry of the device.

The groove-slit separation distance D is vital because it determines the phase difference achievable between two plasmonic modes under different states of DFLC, thus determining the contrast or modulation depth. The amplitude of the output for the two refractive index states is plotted against D in Fig. 4-8. Under impinged light of 514 nm, the permittivity of silver is $\epsilon_m = -9.242 + i0.7924$. Using, Eq. (4-1), the SPP wavelength existing at the interface between silver and DFLC with n_o of $\lambda_{\text{spp},o} \sim 300$ nm, while the SPP wavelength for the case of DFLC with n_e is $\lambda_{\text{spp},e} \sim 240$ nm.

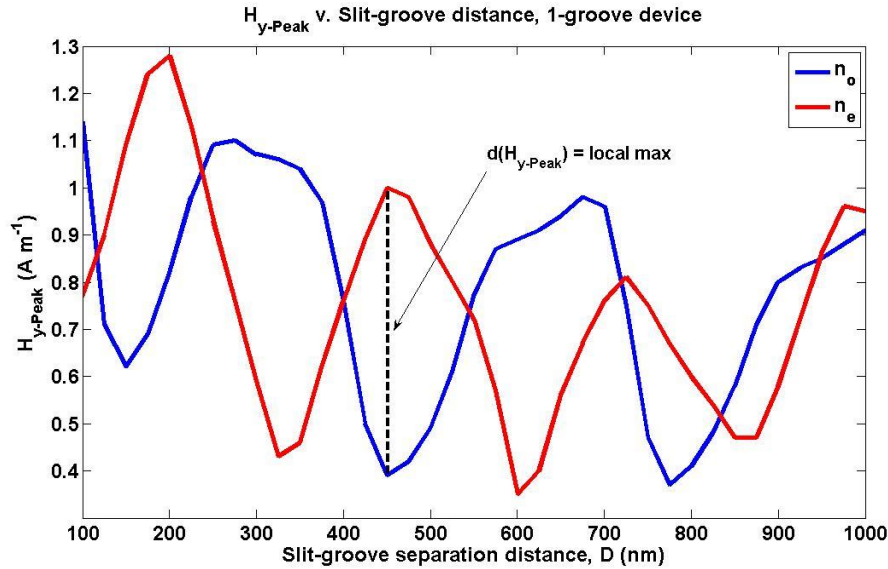


Figure 4-8. Amplitude contrast for single-groove device. Measurements were conducted at 25 nm intervals over the given range of groove-slit separation distances. The distance at which the phase difference between the SPP waves is greatest is marked for clarity. This distance corresponds to $D = 450$ nm, at which a modulation depth of ~ 8 dB was exhibited. Notably, the magnitude of contrast at $D = 325$ nm and $D = 600$ nm is comparable to that at $D = 450$ nm.

Using $z_1 = 100$ nm, $z_2 = 200$ nm, and $D = 450$ nm and after subtracting the periodic multiples, Eq. 3-10 yield $\Delta\phi_o = 1.3813\pi$ and $\Delta\phi_e = 0.3337\pi$. Taking the cosine of these phase angles, as suggested by the relation: $I = I_1 + I_2 + \sqrt{I_1 I_2} \cos(\Delta\phi)$, it can be seen that $\Delta\phi_o$ will lead to an output intensity less than the sum of the inputs whereas $\Delta\phi_e$ will lead to an output

greater than the sum of the inputs, in agreement with the simulated results of Fig. 4-8. Setting $\Delta\phi_e = 0$, we can solve for the ideal distances, which are integer multiples of ~ 70 nm. The nearest ideal distance to our simulated results is thus 420 nm, at which $\Delta\phi_o = 1.1813\pi$ and $\Delta\phi_e = 0\pi$. We can reconcile the difference between the simulated contrast and that predicted by Eq. (4-3)-(4-10) by the fact that we have assumed negligible losses for the propagating modes at the LC-silver interface.

After the initial device geometry was simulated, a second device, shown in Fig. 4-9(a), consisting of two grooves and a single slit was designed and tested via simulation. The dimensions of the second arm of this two-groove interferometer were identical to those of the earlier proposed design. The form of this device was conceived as a basis for exploring increased modulation depth. Fig. 4-9(b) and (c) show the Poynting vector plotted against the geometry of the two-groove device. For both arms the groove-slit distance, D , is 450 nm. The ON/OFF states indicate a high contrast, which is compared to the contrast of the single-groove device in Fig. 4-10. Observation points and planes were placed at the output of the slit for both device structures to determine the amplitude of the transmitted signals with greater detail. As indicated in Fig. 4-10, by using a double-groove single-slit geometry, a higher ON/OFF contrast could be obtained over the single-groove single-slit geometry.

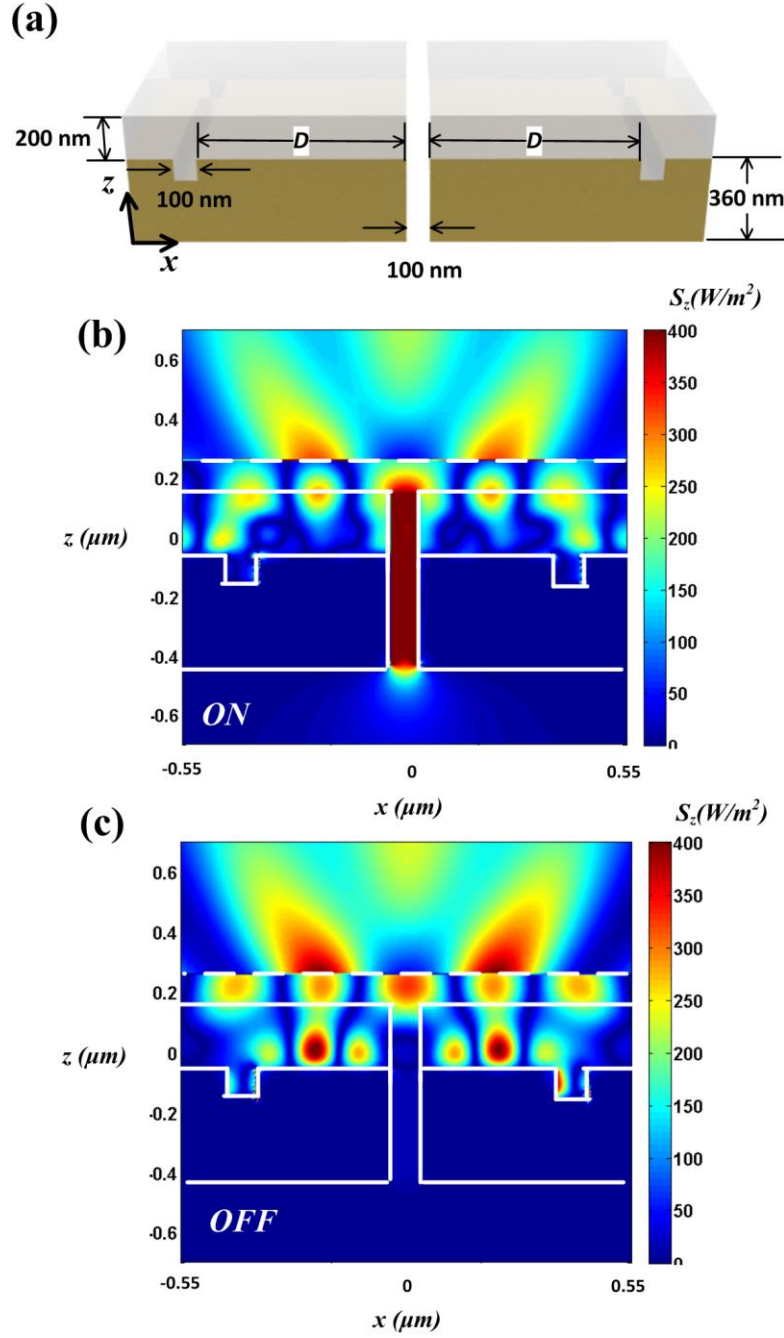


Figure 4-9 (a) Detailed geometry of the double-groove single-slit DFLC-enabled nanoplasmonic modulator. Field intensity plots for the (b) ON state ($n = n_o$) and (c) OFF state ($n = n_e$). The relative magnitude of the Poynting vector is shown against the two-dimensional geometry of the device.

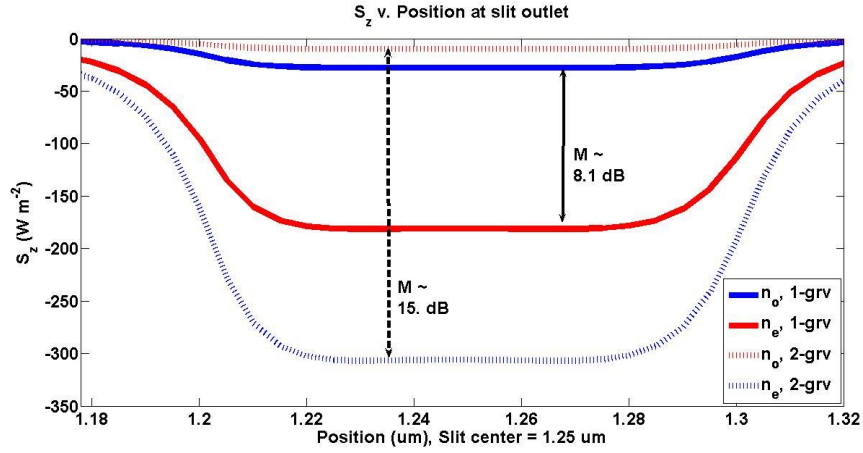


Figure 4-10. Intensity contrast for 1-groove and 2-groove devices. The contrast of the 2-groove device is ~ 15 dB whereas the 1-groove device exhibits contrast of ~ 8.1 dB.

The contrast, given by Eq. (2), exhibited by our devices is approximately 8.1 dB and 15 dB for the single-groove and double-groove designs, respectively. Taking into account our input excitation and pump sources were simulated with 1 A m^{-1} power densities and the size of the groove and slits, we have a first approximation for the optical part of the switching power of 9.42 pW per operation. The duration of the excitation and pump pulses depends on the type of source. Given that the simulations lasted ~ 120 fs, the optical energy involved per operation is trivial compared to the electrical part of the switching energy. Based on previous works, [184, 198] we gather that the average switching voltage of the DFLCs is 25 V. To calculate electrical switching energy and time, we define an average dielectric function of the DFLC, ϵ , as

$$\epsilon = \frac{2n_o^2 + n_e^2}{3} \approx 2.501. \text{ The cross-sectional area of our cell is approximated by assuming a device}$$

with a depth equal to the cell length of 450 nm. With these parameters, we compute the cell capacitances for the double-groove device, $C \sim 2.24 \times 10^{-17} \text{ F}$. The capacitance can be used to compute the switching energy, E , by the relation $E = CV^2$. [226] Therefore, the approximate switching energy is $E \sim 14 \text{ fJ}$ per operation. Even if the switching voltage is doubled, the switching energy remains in the femtojoule range at $\sim 56 \text{ fJ}$ per operation. The switching energy for the single-groove device is simply one half that of the double-groove device.

For the response time τ , we must look into the optical path length of the plasmonic signal, the RC delay imposed by the electrical part of our device, and the rotation time of the DFLC. In the optical limiting case where the device is in the OFF state and $n = n_e$, the transit time of the plasmonic signal is computed with the assumption that the distances between the excitation and the silver-air interface, as well as the slit outlet and a hypothetical detector or adjacent device, are both $1 \mu\text{m}$. We find that $\tau_{\text{transit}} = 10.9 \text{ fs}$. For the electrical part of the response time, we impose the assumption that our function generator voltage source has an internal impedance of 50Ω , and compute $\tau_{\text{RC}} = 1.12 \text{ fs}$. Both transit times are much shorter than the limitation imposed by the response time of the LC, which depends on the thickness and applied field strength; for sub-micron thick nematic, the response time is on the order of 100 microseconds. [308, 309]

The dependence of the contrast on the location of the field monitors was also explored. Fig. 4-11 shows the contrast between the powers measured for the two DFLC states for three different observation planes. The planes are located 20 nm, 120 nm, and 220 nm from the bottom slit edge. Using Eq. (4-2) for all three data sets verifies that the contrast between the SPP propagating through n_o and n_e remains constant regardless of the location of the measurement plane.

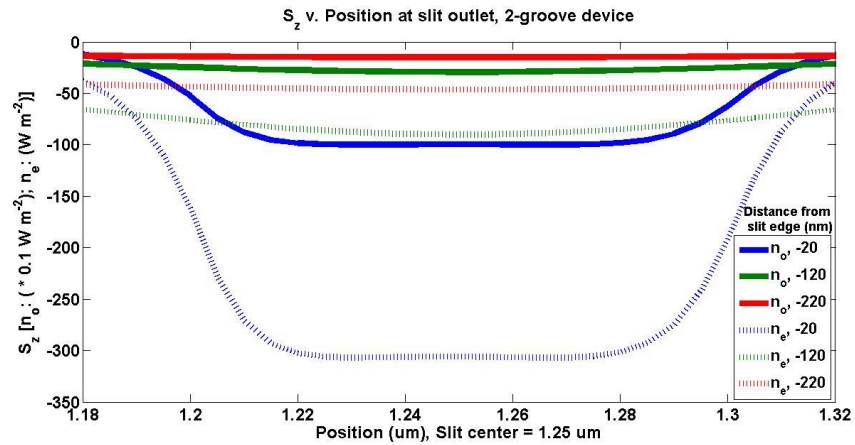


Figure 4-11. Intensity contrast for 2-groove device with three different observation planes. The contrast measured at each plane is $\sim 15 \text{ dB}$, verifying that, while the power of the signal decreases

with distance from the lower slit edge, the contrast between corresponding n_o and n_e signals remains constant.

Section Summary

To fabricate our proposed devices, focused ion beam can be used to cut the grooves and slits on the silver film with precision control of the width and cutting depth. The processing of DFLC is challenging because we are using a relatively thin film during the simulation. However, with in-plane-designed devices, such as the optical superlens, [317] impregnation of the liquid crystals is achievable. Future work will consist of fabricating devices in accordance with both the single-groove single-slit and double-groove single-slit geometries. Experiments will be conducted to determine the response time of the liquid crystal switching mechanism for amplitude modulation, the energy required for modulation, and the magnitude of modulation depth.

4.2. Light Routing and Re-directing via Passive Plasmonic Nanostructures.

4.2.1. Nanoscale Super-Resolution Imaging via Metal-Dielectric Metamaterial Lens System

In optics, the diffraction limit has always been an obstacle that prevents many optical components from being integrated within micro/nano systems. Super-resolution imaging can provide a method to circumvent this limit and has been a prominent research focus in optics since J. B. Pendry proposed the idea of a perfect lens in 2002. [318] By introducing a material with a negative refractive index, all the Fourier components including the propagating and evanescent waves, can be transmitted through such a material, yielding perfect images without resolution limitations and aberration. Exciting though it is, the realization of a material with negative refractive index poses formidable challenges with current fabrication techniques. Feasible

solutions have been reported using quasi-static approximations of the electromagnetic field, which deal with permittivity and permeability separately at the nano scale. [254, 255, 319-322] Compared with perfect imaging, super-resolution imaging is easier to obtain because the fabrication requirements are less stringent. It has been established that super-resolution imaging is possible in materials with negative dielectric permittivity, due to the decoupling of the electric and magnetic fields in the static approximation. [268, 269, 323-326] This simplified perfect lens, called a super lens, has been extensively investigated because of its relatively simple fabrication and practical application. Another way to achieve perfect/super resolution imaging is to use metamaterials designed by transformation optics [264, 327, 328] or conformal mapping; [265] these methods have been applied to design many novel optical devices such as optical cloaks, [329-332] energy harvesters, [163, 175, 176] energy concentrators, [327, 333] and phase transformers. [328] The optical hyperlens consisting of a multi-layer metamaterial demonstrated imaging resolution beyond diffraction limit. [60, 271, 334] A two-dimensional imaging system based on a multilayer metamaterial structure has also been reported. [335] Both superlens and hyperlens rely on the almost perfect matching condition built upon a permittivity match between the metal and dielectric used. Highly dispersive real metals will cause these designs to be valid only for a small range of frequencies. One viable solution to this dilemma is to use different thickness to compensate for the permittivity difference between two different materials, [336] and is further extended to use a wire medium to obtain super resolution imaging without the limitation of the material choices. [337-339] Optical bilayers, reported by Smith and colleague, open another door for imaging beyond diffraction limits by collecting and transmitting evanescent waves through a lens-like structure. Unfortunately, difficulties in realizing two layers without definite permittivity or permeability restrict the application of such imaging system. [340]

In this section, we have demonstrated super-resolution imaging in an optical multilayer imaging system using an interlayered structure of two different metamaterials. By introducing a

metamaterial into the design of the bilayer system, we have shown that super resolution can be achieved through simple structures with satisfied transmission loss. The initial design of the metamaterials lens was accomplished using the Effective Medium Theory (EMT). Our design was further confirmed with simulation results conducted with the commercial software COMSOL Multiphysics. Finally, the designed structure was optimized by applying the Transfer Matrix Method (TMM). [341] The realization of the proposed metamaterial lens system could find applications in areas such as nanolithography, optical storage, bio-sensing and nanoimaging.

The schematic of the proposed metamaterial lens system is shown in Figure 4-12, which gives details about the imaging process and construction of the metamaterial lenses. The design involves two groups of interlayered structures. Alternate layers of dielectric material 1 (green) and a thin metal film (yellow) form lens 1, while alternate layers of a different dielectric material 2 (blue) and a similar thin metal film (yellow) form lens 2. These two lenses constitute the diverging and the converging parts of the lens structure, respectively. These converging and diverging components allow object near the bottom of the structure to be imaged with resolution well below the diffraction limit.

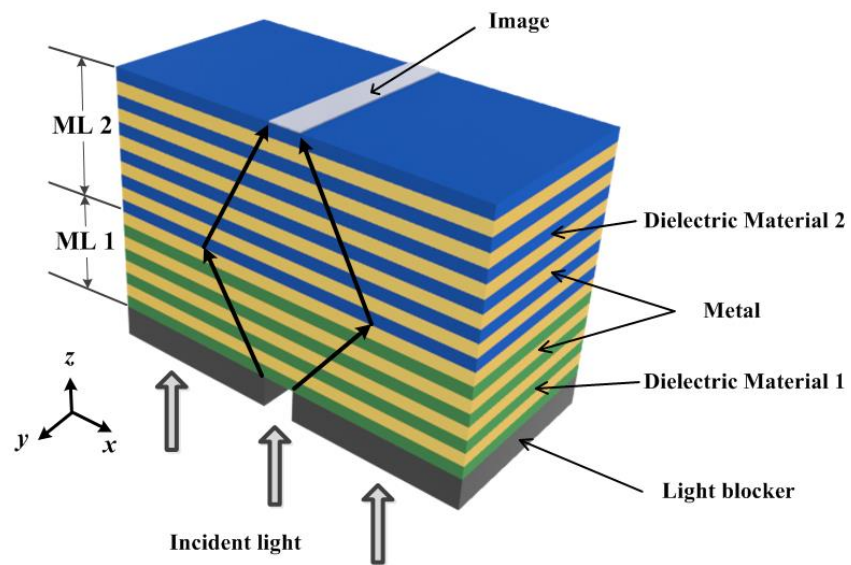


Figure 4-12. Schematic of the metamaterial lens system for imaging. Incident light passing through slit object will diverge in metamaterial lens 1 (ML1) and converge in metamaterial lens 2 (ML2), forming an image on the top surface of ML2.

The physical origin of the imaging effect arises from the unique optical properties of the two metamaterials, which are both comprised of anisotropic metallodielectric interlayered film structures. The performance of the two lenses is determined by parameters such as material properties, thickness of the films/layers, and the arrangement of the films. The behavior of these layered arrangements can be understood with EMT. As the thickness of each layer is less than one-tenth of the incident wavelength, the approximation made by EMT is accurate. According to the EMT approximation, the effective permittivity of the structure can then be related as

$$\begin{aligned}\varepsilon_x &= \varepsilon_y = \varepsilon_d f + \varepsilon_m (1 - f) \\ \varepsilon_z^{-1} &= \varepsilon_d^{-1} f + \varepsilon_m^{-1} (1 - f)\end{aligned}\quad (4-11)$$

where ε_d denotes the permittivity of dielectrics, ε_m represents the permittivity of the metal materials, f is the filling factor of the dielectric layers, and ε_x and ε_z are the effective permittivities along the transverse and normal directions, respectively. An appropriate filling factor yields combinations of ε_x and ε_z with opposite signs, implying hyperbolic forms of the dispersion relation for transverse magnetic (TM) polarized plane waves. Considering the symmetric relation of the film in the x and y directions, the problem can be simplified using a 2D approach by which the dispersion relation can be expressed as follows:

$$\frac{k_x^2}{\varepsilon_z} + \frac{k_z^2}{\varepsilon_x} = \left(\frac{\omega}{c}\right)^2 \quad (4-12)$$

where ω is frequency, c is the velocity of light in vacuum, and k_x and k_z represent the wave vectors in the transverse and normal directions, respectively. Two different combinations, $\varepsilon_x < 0$, $\varepsilon_z > 0$ and $\varepsilon_x > 0$, $\varepsilon_z < 0$ lead to different hyperbolic dispersion curves, which can be differentiated by checking the locations of their main axis. The illustration of the two hyperbolic dispersion curves is given in Figure 4-13(a).

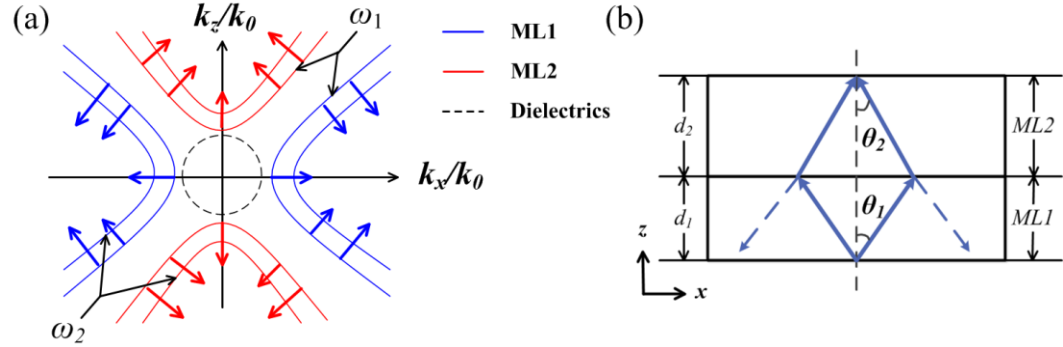


Figure 4-13. (a) Hyperbolic dispersion relations for $\epsilon_x < 0$, $\epsilon_z > 0$ (blue) and $\epsilon_x > 0$, $\epsilon_z < 0$ (red). The arrows indicate the direction of group velocity for two frequencies with $\omega_1 < \omega_2$. The dashed circle represents the dispersion curve for isotropic materials. (b) Schematic of imaging process by ML1 ($\epsilon_x < 0$ and $\epsilon_z > 0$, below) and ML2 ($\epsilon_x > 0$ and $\epsilon_z < 0$, above).

The group velocity $v_g = \nabla_k \omega(k)$ denotes the energy flow direction: normal to the dispersion curves of constant frequency. [342, 343] To further elucidate the direction of Poynting vector, arrows have been drawn on the dispersion curves in Figure 4-13(a) indicating its direction. [343] To distinguish between the two lens structures, the corresponding metallodielectric film structures are referred to as Metamaterial Lens 1 (ML1) and Metamaterial Lens 2 (ML2). For both lenses, the directional light propagation in the lens is caused by the asymptotic behavior of the hyperbolic dispersion function. As k_x becomes large, the light propagation direction can be defined by θ with respect to the normal direction

$$\tan \theta = \sqrt{-\frac{\epsilon_x}{\epsilon_z}} \quad (4-13)$$

The dispersion curves also indicate that the waves with large transversal wave vector ($k_x \geq k_0$), which are commonly evanescent waves in natural optical materials, can be transmitted.

We studied this system with an object near the bottom of the structure under normally incident light (z -direction). The light, after being scattered by the object, enters ML1 and diverges mainly along two symmetrical directions determined by Equation (4-13). At the interface of ML1 and ML2, the direction of light propagation will be bent inwards; the extent to which the light is

bent is determined by the energy flow direction normal to the intrinsic dispersion curves of ML2, shown as red arrows in Figure 4-13(a). This leads to the reconstruction of the image at the top surface of ML2, provided that the thickness d_1 of ML1 and that of ML2 d_2 roughly meet the following relation

$$\frac{d_1}{d_2} = \frac{\cot(\theta_1)}{\cot(\theta_2)} \quad (4-14)$$

with θ_1 and θ_2 obtained from Equation (4-13). As illustrated above, the object plane and image plane of the interlayered imaging structure are at the top and bottom of the structure, respectively. The working distance in this structure is determined by the total thickness of ML1 and ML2, which can be simply estimated as $d_1 + d_2$.

During the design process, we set the filling factor f for both MLs to be 0.5, making the dielectric and metal films equal thickness. Such an assumption restricts the permittivity of the metal to be larger than that of the dielectric material in ML1 and smaller for ML2. Given the relation $n^2 = \epsilon\mu$, where refractive index is given by n , permittivity by ϵ and permeability by μ , there is a limited choice of contrast between low and high refractive index dielectric materials. Moreover, the choice of metal (i.e., silver) as the interlayer is limited by its permittivity at the desired frequency, chosen for its popular use in applications such as nanofabrication. For simplicity, we have chosen same metal for both ML1 and ML2.

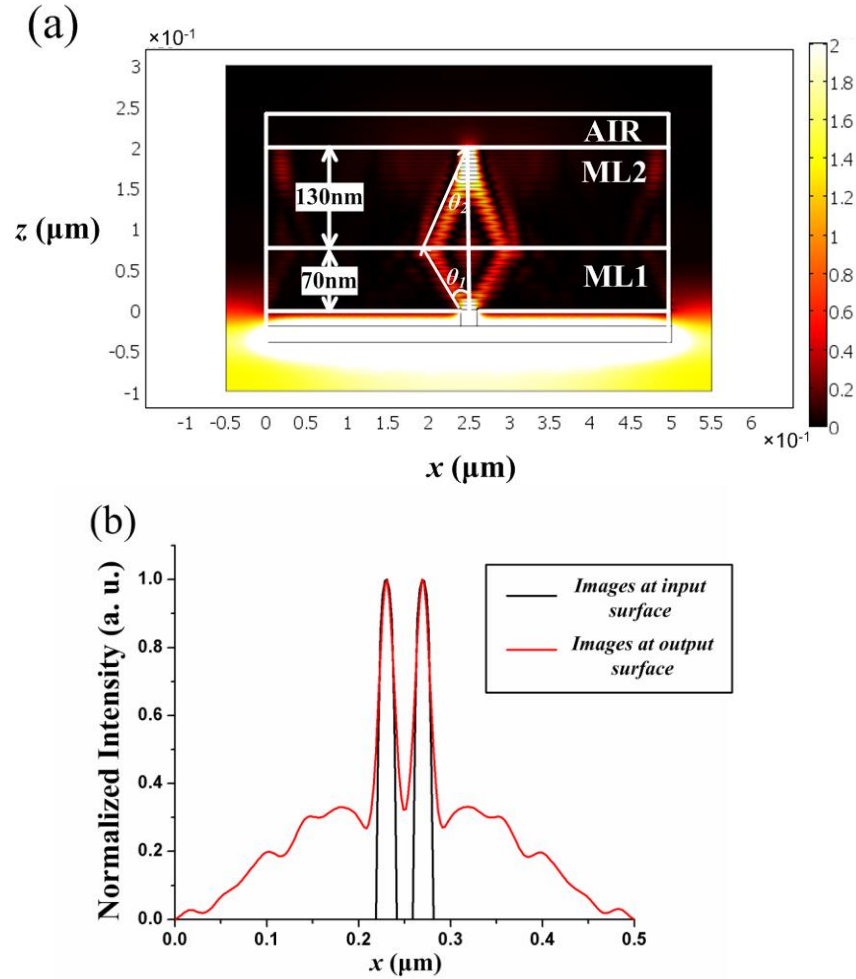


Figure 4-14. The simulation result of ML imaging, corresponding to the structure shown in Figure 4-12. (b) The normalized intensity of the images of two slit objects on the input and output planes. Two slit objects are 20 nm in width each and their center-to-center distance is 40 nm.

The simulation is conducted using the commercial software, COMSOL Mutiphysics. We use silver with permittivity of $-2.6+0.13i$ at 365 nm, as an ideal candidate for the metal interlayer in both lenses. The permittivities of the dielectric materials in ML1 and ML2 are selected as 1.0 and 4.84, respectively, corresponding to air and a polymer with a high refractive index. A chromium layer is used at the input surface to block all unwanted incident light, while a slit through the layer acts as an object for imaging. Chromium also has a permittivity of $-10+10.8i$, and strongly damps the unwanted propagating surface plasmons excited at its interface with ML1.

A chromium layer of 50 nm thickness is sufficient to provide the aforementioned features. The thickness of each alternating metal and dielectric layer is set to 5 nm initially to demonstrate imaging and is optimized later. The calculated effective permittivities are $\varepsilon_x = -0.80$ and $\varepsilon_z = 3.24$ for ML1 and $\varepsilon_x = 1.11$ and $\varepsilon_z = -11.27$ for ML2, corresponding to propagation directions with $\tan\theta_1 = 0.49$ and $\tan\theta_2 = 0.31$ according to Equation (4-13). The relation connecting the total thickness of ML1 and ML2 can be found in Equation (4-14), with known values of θ_1 and θ_2 . Here, we set the thickness for ML1 to be 70 nm and that for ML2 to be 130 nm, which approximately meets the criterion of Equation (4-14). The object is a slit of width 20 nm. The incident light takes the form of a plane wave impinging normal to the chromium layer as shown by the arrows in Figure 4-12. The simulation is conducted based on the finite element method, where sufficient meshes are needed to ensure a convergent result. The simulation area of 600 nm \times 400 nm is divided into approximately 200,000 meshes, determined by the smallest film thickness of 5 nm. Continuous boundary conditions are applied to the inside structure of the imaging system, while a perfect electric conductor condition is used for the outside boundaries enclosing the simulated area. Perfect magnetic conductor conditions are used at the interface of the chromium layer and ML1 to further filter the disturbance caused by both surface plasmons and scattered light. The simulation area is enclosed by perfectly matched layers to eliminate any reflection back into the structure, thus preventing interference.

The simulation results are shown in Figure 4-14(a). Light energy is transmitted symmetrically along two directions, changing its propagating direction at the interface of ML1 and ML2; the result is a focused image at the top surface of ML2. The image spot has a full width half maximum of about 25 nm, illustrating super-resolution imaging capability. Moreover, two closely positioned objects can be clearly resolved. Figure 4-14(b) illustrates a plot of the spatial distribution of two slit objects with center-to-center distance of 40 nm (black) and the corresponding images at the image plane (red). The resolving power is about 1/9 of the working

wavelength (365 nm). The background associated with the image in Figure 4-14(b) is believed to arise from the low k_x components, which do not follow the principle directional route in the structure, but decay exponentially and propagate in the direction normal to ML1 and ML2.

We use the Transfer Matrix Method (TMM), which is based on rigorous coupled wave analysis, to investigate the imaging structure designed by EMT. Figure 4-15(a) represents the dispersion curves for the presented imaging structure with EMT and TMM. The curves obtained by the two methods agree well for small k_x , but differ greatly with increasing transverse wave vector. An intuitive view of the imaging behavior is shown in Figure 4-15(b), which shows the energy flow direction for a variety of k_x , through the ray tracing method within the multi-lens structure. Clearly, the light does not converge to one ideal image point; rather, it converges to a region extended along both transverse and normal directions, indicating some aberration in the lens. The inset of Figure 4-15(b) shows the transverse shift of the converging image at a distance of 200 nm from the object. Noting that low k vectors cannot be transmitted effectively in this structure because of the band gap shown in Figure 4-13(a). As seen from Figure 4-15(b), a resolution of ~ 20 nm can be achieved, which is consistent with the results shown in Figure 4-14. As the film thickness increases, the extension of the focal region will be more obvious and the resolving power of the system will be reduced.

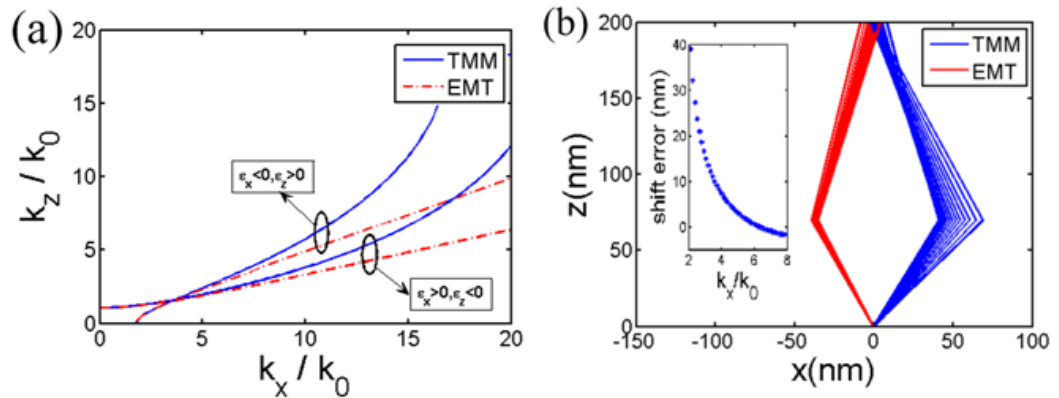


Figure 4-15. (a) The dispersion curves in first quadrant for a fixed frequency calculated by EMT and TMM with the same parameters. (b) The ray trace in the imaging structure, estimated using EMT and TMM, the inner plot shows the different shift errors corresponding to different k_x .

The film thickness is yet another factor influencing imaging quality that should be taken into account. Here we assume that the total number of layers in the two structures is fixed. Further simulation results (Figure 4-16) with thicker films show reduced imaging quality using the same object and mask. This phenomenon can be explained by the fact that the increased thickness of the layers diminishes the transmission of evanescent waves, essentially through the coupling of surface plasmon modes in metallodielectric films due to the layers' resemblance to surface plasmon waveguides. The plasmon coupling length increases as the layer thickness increases, so a broadening of the image point will be observed clearly in Figure 4-16(b) and Figure 4-16(c). The coupling of the propagating light to surface plasmons will be investigated in future work; here we will only analyze the imaging process employing the TMM. With the increase in film thickness, the dispersion curves calculated by the TMM are no longer hyperbolic, but rather show an exponential response with normalized k_z . The dispersion curves increase greatly within a small range of the normalized k_x , and result in a divergence of the energy flow, illustrated in Figure 4-16(b).

According to Figure 4-15(a), both diverging angle and converging angle increase as the film thickness increases. Thus, the expansion of the focal region can be accounted for by changing the ratio d_1/d_2 according to the ray-tracing analysis. Increasing the ML2 one unit cell (one pair of metal and dielectric layer) thickness while decreasing ML1 one unit cell thickness results in a much smaller focal region, as shown in Figure 4-16(d). Even if the thickness of each layer is increased up to 20 nm, super resolution can still be achieved with a little adjustment of the theoretical triangular relation. However, it can be seen from Figure 4-16 that the intensity has significantly decreased with the increment in film thickness. Another paradoxical factor is the absorption loss in metal films, which usually has a negative influence on imaging resolution; this

effect has already been seen in the superlens. Large absorption also leads to reduced performance and resolution when transferring the large k_x component. On the other hand, slight absorption helps eliminate the potential adverse effects of multiple reflections and refractions at the interface of two different structures.

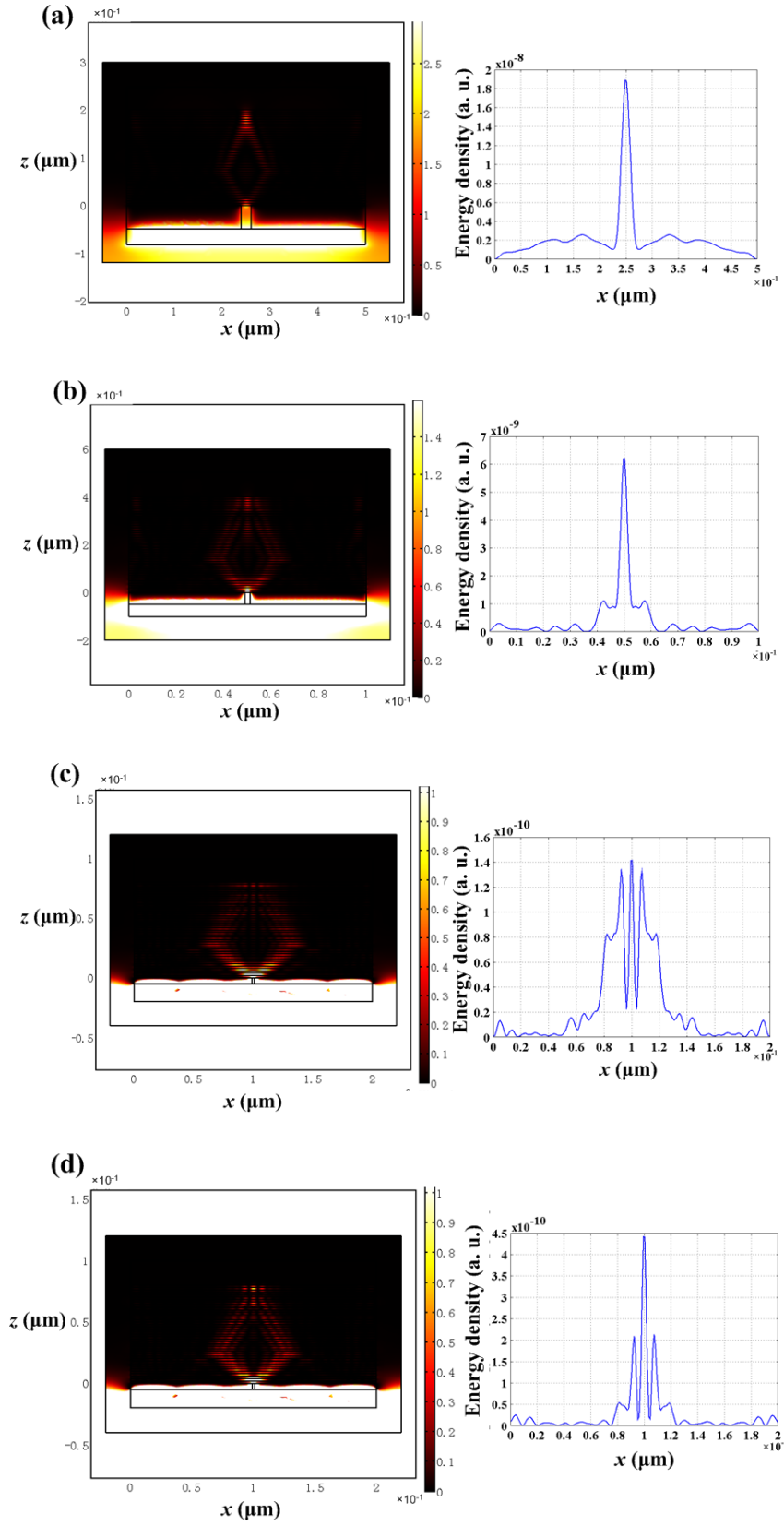


Figure 4-16. (a) Focus with full-width-half-maximum (FWHM) of 25 nm is achieved when the thickness is 5 nm for each layer and the total thickness of the imaging structure is 200 nm. (b) FWHM is ~35 nm when the layer thickness is increased to 10 nm and the total thickness of the structure is 400 nm. (c) The FWHM is ~400 nm when the thickness of each film is 20 nm and the total thickness of the structure is 800 nm. (d) Using the same structure in Figure 5(c) while changing the thickness ratio of ML1 and ML2 based on the ray trace analysis. The size of the focus reduced back to 40 nm.

Other than super resolution, our lens system has the advantage of lower transmission loss when compared to similar designs, such as the hyperlens. Figure 4-17 plots the cross section cut from the center of the slit for both our lens system and a hyperlens system with same number of layers and the same film thickness. Here we use the same metal (silver) in both cases to avoid the external loss caused by the metal itself, as metal is the major cause of propagating loss. For the demonstrated case in Figure 4-17(a), we can see that a comparable transmission efficiency is achieved by our lens system when compared to a hyperlens configuration with perfect match ($Re(\epsilon_m) = -\epsilon_d$). Almost no transmission can be observed from $z = 100$ nm to $z = 300$ nm, confirming our claim that the image is obtained through focusing rather than direct transmission of the input light. The transmission loss can be further reduced by designing a lens system with fewer layers, as plotted in Figure 4-17(b). By cutting the number of layers in half, much higher transmission efficiency can be achieved in our lens system than the hyperlens. Around 50% of incident energy is focused to the image point due to the directed transmission of almost all the large wave vector components in our metamaterial lenses system.

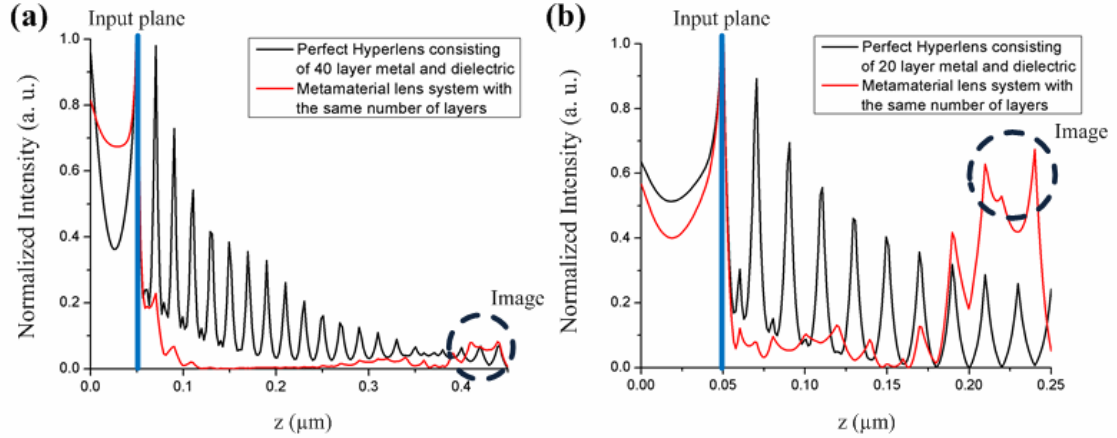


Figure 4-17. (a) The comparison of our lens system with a hyperlens configuration under the perfect matching condition ($Re(\epsilon_m) = -\epsilon_d$). Comparable transmission (around 10 %) can be observed in both systems. (b) Much higher transmission (50 %) can be achieved in our lens system (30 %) when the system is redesigned with fewer layers. All the results are obtained through a cross section cut from the center of slit through the center of the lens.

The metamaterial lens based super-resolution imaging structure proposed in this article can be fabricated by confining the imaging structure and process to a planar space on a substrate. Moreover, by using e-beam lithography, it is convenient to obtain the proposed hetero metallodielectric structure with the desired thickness and number of thin layers. Similar methods have also been utilized to demonstrate the imaging of a hyperlens on a substrate in the visible frequency range.

Section Summary

I have numerically demonstrated that super-resolution imaging can be realized in a hetero metamaterial structure consisting of two cascaded interlayered structures comprised of alternating dielectric and metal films. Utilizing EMT and TMM methods, we show that imaging with resolution nine times smaller than the light wavelength can be achieved by combining two lenses made of interlayered structures forming the metamaterial lens structure. We also show that the

imaging effect can be further optimized by changing the thickness of the lens for the unit cell with different thicknesses. With its high resolution and simple structure, the proposed imaging system can be valuable for applications such as nanolithography, optical storage, and bio-sensing.

4.2.2. Beam Bending via Plasmonic Lenses

With the advent of nanotechnology, the ever-increasing interest to explore the optical world at nanoscale has presented the demand to manipulate visible light in the subwavelength scale. Researchers have made significant efforts to decrease the size of optical lenses to micron and submicron scale for this very purpose; however, due to diffraction limit, their efforts are hindered when the size of a lens approaches the wavelength of the light. One possible method that enables the manipulation of visible light in the subwavelength scale uses surface plasmons; these surface plasmon-based lenses, or so-called plasmonic lenses, can achieve subwavelength-scale focal zones. [280, 344-348] Plasmonic lenses have proven to be useful in numerous applications such as nanofabrication, [280, 345, 346] nanophotonic circuits, [347, 349, 350] and circular polarizer analyzers. [351, 352] In these applications, plasmonic lenses have been used to focus light at subwavelength scale. However, to fully realize the potential of plasmonic lenses, it is necessary to not only focus light, but also to manipulate and precisely position it at small scales.

Positional modulation through a plasmonic lens was first numerically demonstrated in Shi's study, [316] where an axial tuning of the focal points was obtained by varying depths of grooves surrounding a central slit. Experimental demonstrations of the same concept have been reported by Verslegers *et al.* [353] and Lin *et al.* [354], independently. Meanwhile, little work has been done to achieve directional tuning (*i.e.*, bending) of light through a plasmonic lens. Kim *et al.* constructed an asymmetric metallic plasmonic lens with different materials to deflect normally incident light beams. [355] Liu *et al.* tuned the focal point off the optical axis simply by changing

the incident angle of the incident light beam; [356] however, in this approach, the tuning occurs only in the near field, which significantly restricts the working distance.

In this section, we aim to provide a more practical method (from the fabrication aspect) to achieve directional modulation with a plasmonic lens. We introduce a design principle for plasmonic lenses that can bend light along the direction transverse to the propagation direction. Light bending is achieved by constructing a carefully designed, curved phase front for the plasmonic lenses. The control of the phase front profile is achieved through two mechanisms: phase retardation caused by the width and shape of the individual slits in the lens, and the position of these slits. The proposed single-layered lenses can be fabricated using the Focused Ion Beam (FIB) technique and thus is considered much feasible than the existing counterparts, and far field intensity redistribution with acceptable energy loss is clearly observed from the simulation results.

Principles

To bend normally incident electromagnetic (EM) beams off the optical axis, we have designed three plasmonic lens structures. As depicted in Fig. 4-18, these designs (referred as Lens I, Lens II, and Lens III) are all composed of a linear array of air-filled rectangular or tapered slits in a gold or silver background. In Lens I, we use the dependence of phase change on slit width to our advantage. As shown in the design [Fig. 4-18(b)], the slit length d and spacing a are kept constant, while the slit width w along the transverse direction (y -axis) is varied. In Lens II [Fig. 4-18(c)], we design a slanted cut on the output side, which causes a linear variation of the slit length d from one end of the lens to another. The slit width (50 nm) and spacing are kept constant. In this case, although the transmission coefficient β is the same for all slits, different phase delays can be obtained by the dependency of phase change on slit length.

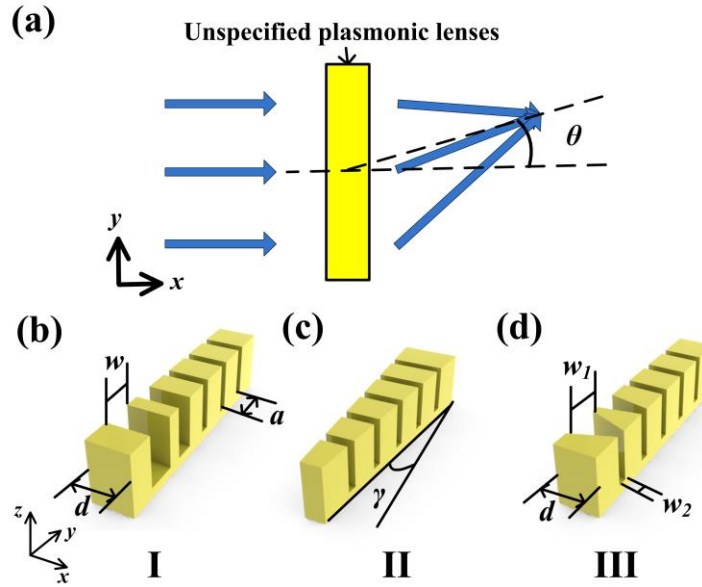


Figure 4-18. (a) Schematic of a plasmonic lens that can bend a light beam or focal point in transverse direction; (b), (c) and (d) are the isometric views of three proposed designs of the plasmonic lens, termed as Lens I, Lens II, and Lens III.

In Lens III [Fig. 4-18(d)], we employ tapered slits to form an asymmetric phase front for beam bending, as tapered structures have proven useful in the design of plasmonic waveguides. [357-359] The main advantage of a tapered waveguide over a rectangular one lies in its superior surface plasmon mode confinement; this is because the output aperture of a tapered waveguide is generally smaller than the incident wavelength. The second advantage of using tapered structures is that enhanced transmission can be obtained when the input aperture is larger than the output aperture. [360] In the design of Lens III, we keep the slit length d , spacing a , and output aperture w_2 constant; the input aperture w_1 is the only variable in the design. Compared with the planar lens structure (Lens I), the tapered structure (Lens III) is expected to perform better in confining plasmonic modes and enhancing optical transmission.

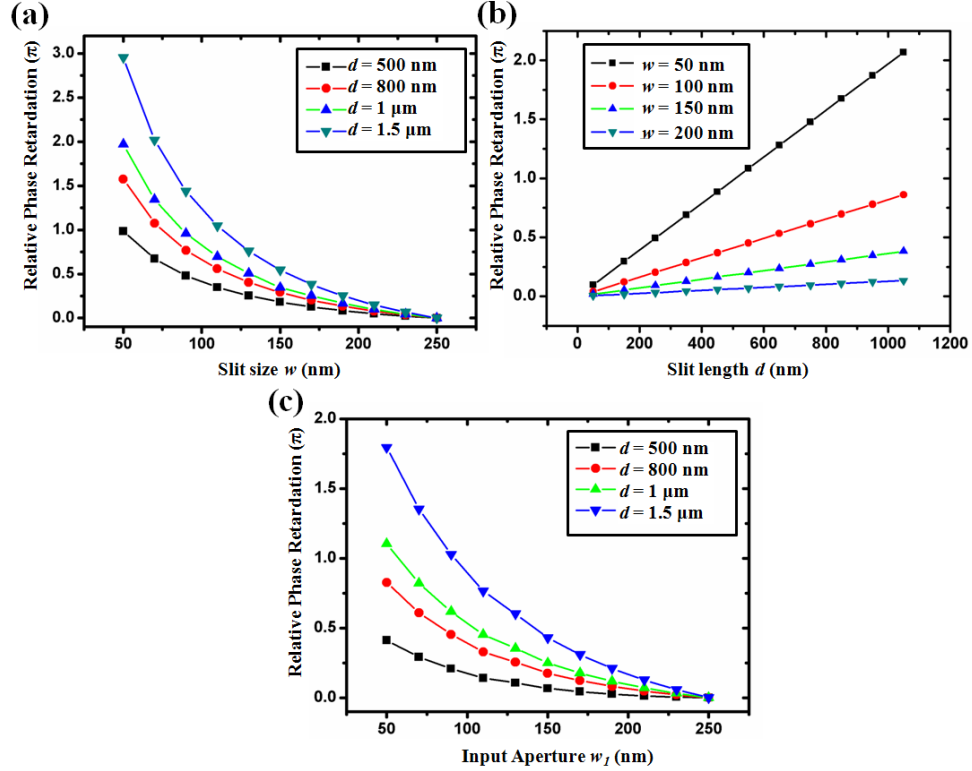


Figure 4-19. (a) Relative phase change caused by varying the width of a rectangular slit w . (b) Relative phase difference caused by varying the length of the slit d . (c) Relative phase difference of a tapered slit. The input aperture w_1 is varying, while the output aperture w_2 is fixed at 50 nm.

In all three lens designs, each individual slit is significantly smaller than the incident wavelength; thus it can be treated as a plasmonic waveguide. As an incident EM wave meets the slits, it will be converted into surface plasmons due to the end-fire effect, [361] transmitted in the form of surface plasmon modes along the waveguide, and then decoupled back to an EM mode with a phase delay upon exiting the slit. The transmission coefficient β , which is related to the phase change of the EM wave after it passes through the structure, can be expressed as: [362, 363]

$$\tanh(w\sqrt{\beta^2 - \varepsilon_d k_0^2}/2) = -\frac{\varepsilon_d \sqrt{\beta^2 - \varepsilon_m k_0^2}}{\varepsilon_m \sqrt{\beta^2 - \varepsilon_d k_0^2}} \quad (4-15)$$

where k_0 is the wave vector in vacuum, w is the aperture of the waveguide, and ε_d and ε_m are the

permittivities of the dielectric material and metal, respectively. In the case of a tapered waveguide, the slit width w varies with propagation distance, and the transmission coefficient β varies accordingly. Nevertheless, we can calculate the effective transmission coefficient β_{eff} by integrating each discrete β along the length axis (x -axis) of a tapered waveguide. As the phase change, ϕ , of a plasmonic waveguide is the product of its transmission coefficient β and length d , [353] its value can be controlled by varying β and d independently, which correspond to different channel lengths and widths respectively. Figure 4-19 illustrates the geometric dependencies of the phase change of a rectangular slit [Figs. 4-19(a) and (b)] and a tapered slit [Fig. 4-19(c)], calculated by using *Mathematica*. We observe that the relative phase change ϕ is proportional to slit length (d) and inverse of slit width ($1/w$). As shown in Fig. 4-19(a), a relative value up to 3π can be obtained for ϕ as w increases from 50 nm to 250 nm, while d is kept at 1.5 μm . In Fig. 4-19(b), as the slit length d increases from 50 nm to 1050 nm, a linear increase in ϕ up to 2π can be observed when width of the slit is set at 50 nm. In Fig. 4-19(c), the relative phase difference of a tapered slit is plotted against its input aperture w_1 , while the output aperture w_2 is fixed at 50 nm for all conditions. The maximum relative phase shift is 1.8π when $d = 1.5 \mu\text{m}$.

The positional and directional modulation functionalities of a plasmonic lens are determined by the relative phase difference between neighboring slits. By introducing a continuous change to the slit geometry along the transverse direction (x -axis) of a plasmonic lens, we can create a relative phase difference profile across the width of the lens (y -axis). The position of the constructive interferences of the decoupled EM waves depends strongly on the phase delay profile, and it is expressed as beam modulation effect. In this article we focus on beam bending; thus we will build an asymmetric phase front across the plasmonic lens to achieve directional modulation.

Another factor that leads to a phase difference between neighboring slits is the spacing between the particular optical elements. We denote it as center-to-center distance a (Fig. 4-18).

The center-to-center distance plays an important role in the design of Fresnel zone plates, in which focal points are located at the constructive interferences of the transmitted waves from circular slits. In a Fresnel zone plate, the phase difference between any two slits is $2n\pi$ and can be achieved by adjusting slit widths and inter-slit spacing. If we assume that the focal length of a zone plate is f , the phase difference between the center slit and a slit m units away can be expressed as: [353]

$$\varphi(m) = 2n\pi + \frac{2\pi f}{\lambda} - \frac{2\pi\sqrt{f^2 + m^2}}{\lambda}, \quad (4-16)$$

where λ is the incident wavelength and n is an integer. This design principle can be extended to the design of plasmonic lenses. [364] However, the radius of a plasmonic lens is merely several microns, so n cannot be large at all (at most 1 in our cases). Therefore, the phase difference caused by distances between slits will not play a dominant role in the design of the asymmetric plasmonic lens. In the approaches described in this article, we construct asymmetric phase front profiles by modulating the geometric parameters of slits, rather than adjusting inter-slit spacing.

Simulations and discussion

The EM wave propagation was simulated using commercial finite-difference time-domain (FDTD) software: Optiwave FDTD by Optiwave Systems Inc. An area of $5\ \mu\text{m} \times 14\ \mu\text{m}$ was chosen to study the effects of each proposed plasmonic lens structure. The boundary condition was set to the perfect electric condition (perfect matching layers) such that the transverse magnetic (TM) waves encountering these boundaries are totally absorbed. A mesh size of $5\ \text{nm} \times 5\ \text{nm}$ was used to ensure convergent results. TM mode waves were used because of excitation requirements of the surface plasmon waves. The incident wavelength used was 633 nm, with the corresponding permittivity of metals at this wavelength calculated based on the

Drude model. [36] For silver, the permittivity used was $-17.2355 + 0.4982i$. The center-to-center distance, a , of all the slits was set at 500 nm. It is worth noting that the distance between any two slits is much larger than the skin depth of surface plasmon inside the silver, which is of the order of tens of nanometers; hence, no surface plasmon cross-talk will occur between adjacent slits. The length of the slit, or in other words, the thickness of the structure is another important parameter that, when increased, will cause a larger relative phase difference and corresponding modulating power. The trade-off of a thick structure is its low transmission due to high reflection at the interface and absorption inside the slit.

We first demonstrate beam deflection using the design of Lens I [Fig. 4-20(a)]. The structure used in our simulation consists of an 800 nm thick silver slab with seven slits whose width ranges from 50 nm to 200 nm (50 nm, 50 nm, 50 nm, 50 nm, 100 nm, 150 nm, 200 nm, from one side to the other), corresponding to a maximum phase difference of 1.5π . The phase front is presented by dashed lines in Fig. 4-20(a). Under normal incident wavelength of 633 nm, two high intensity regions are observed: the farther one with a smaller off-axis deflection angle refers to the main beam, and the closer one with a higher deflection angle refers to the strongest sidelobe. A main beam deflection of $\sim 8^\circ$ can be observed from the simulation due to the constructive interference of the phase-delayed, transmitted waves from the rectangular slits of Lens I [Fig. 4-20 (b)]. The position of focus and the bending angle is determined by using the free image processing software ImageJ to capture the area with the highest intensity inside the main beam. The locations of sidelobes are determined by the constructive interference condition, however, all sidelobes (including the strongest one) focus EM waves at near field and do not contribute significantly to the plasmonic communication applications. We also show that Lens II with $\gamma=3^\circ$ can be used to deflect the light beam. In this design, the widths of all seven slits remain at 50 nm. In this slanted lens design, the slit length is varied linearly from 226 nm to 374 nm, corresponding to a phase difference of 0.96π . As illustrated in Fig. 4-20(d), the deflection angle

of the main beam is observed to be around 3° and the intensity of the focused beam is relatively low comparing to Lens I. The last design [Lens III, Fig. 4-20(e)] involves tapered slit structures with different input apertures. The output aperture width is kept at 50 nm, which ensures the confinement of surface plasmon modes inside the tapered structure, regardless of the width of input aperture. The widths of the input apertures are set to be 50 nm for the first four slits, and 100 nm, 150 nm, 200 nm for the last three slits, respectively. A phase difference of 1.45π is achieved, and the asymmetric phase front causes the light beam to bend 5° off the center axis and the focused beam is observed to have higher intensity than Lens I [Fig. 4-20(f)].

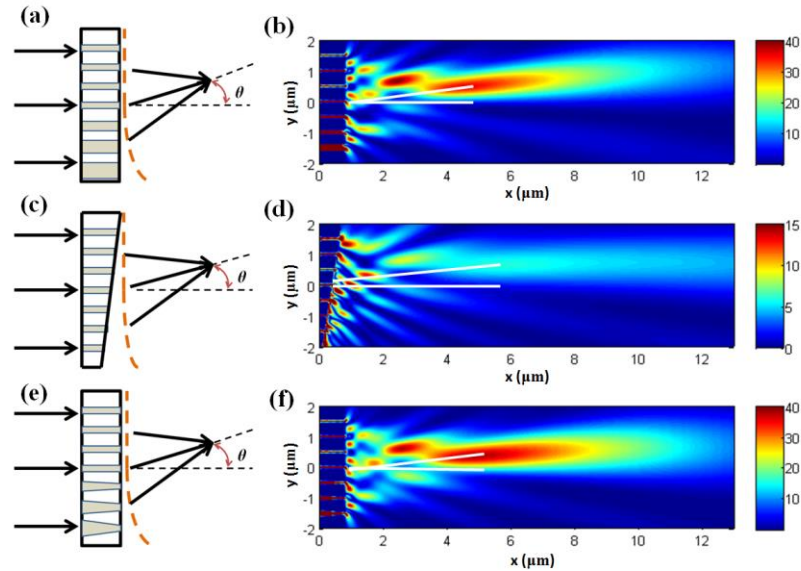


Figure 4-20. (a), (c) and (e) are three representative designs of plasmonic lenses (Lens I, Lens II, Lens III), corresponding to Fig. 1(b), (c) and (d). The constructed phase differences are 1.5π , 0.96π , and 1.45π , respectively. (b), (d) and (f) the corresponding simulation results. All the simulations show the bending of light off the optical axis.

As seen from Fig. 4-20, the three lens designs vary not only in bending angle, but also in light distribution and intensity. We measured the efficiency of the energy passing through the slits of the three lenses (T_1) as well as the efficiency of the energy reaching the region of interest (T_2) through calculating the magnetic field of the EM waves. Since there is only one magnetic component under the incident of TM waves, the EM wave intensity is quantitatively proportional

to the square of the amplitude of electric field, as well as the amplitude of magnetic field. For all proposed lenses, T_1 was calculated as the integral of the amplitude square of the magnetic component along the output side of the plasmonic lenses over the intensity of the incident wave. Given similarly, T_2 was the ratio of the focus intensity to the incident intensity. The measured efficiencies are listed in Table 4-3.

Table 4-3. Efficiency calculation of the proposed plasmonic lenses

	Lens I	Lens II	Lens III
Energy passing through the lenses (T_1)	62.16%	40.48%	72.27%
Efficiency of focusing (T_2)	19.36%	6.25%	20.25%

It is clear that T_1 is much higher than T_2 in all cases. The major reason is the inherited limitation from plasmonic waveguides that the decouple rate of plasmonic modes to propagating EM wave mode is low. Most of energy remains on the output surface of the lens in the form of propagating surface plasmon, which is the conversion of plasmonic modes when they circumvents the singularities at the sharp corners of the slits. The existing of those surface plasmon waves can be confirmed by observing the region between the slits near the output plane in Fig. 4-20. Thus, an intuitive approach to improve the efficiency of focusing is to increase the roughness of the output surface, which will cause more energy decouple into light and propagate to far field.

Although the bending angle of the focused beam by Lens III is a little smaller than that by Lens I, the design of tapered apertures in Lens III renders better efficiency of focusing. As reported previously [21], tapered structures with its ability on collecting input light and confining plasmonic modes, can produce extraordinary optical transmission. This observation matches well with our simulation results (see Table 4-3). We observe that Lens II produces weaker light

intensity [Fig. 4-20(d)] than those in Lens I [Fig. 4-20(b)] and Lens III [Fig. 4-20(f)]. This observation is likely caused by two factors: the smaller input apertures of Lens II, and the slanted output plane introducing additional phase changes [expressed in Eq. (4-16)], which could cause some destructive interference at the focal point decreasing the intensity.

In the simulation shown in Fig. 4-20, the incident light is normal to lens surface. We proceed to investigate the lens performance when the EM waves are incident at an angle to the optical axis (Fig. 4-21). In Fig. 4-21(a), light impinges on Lens III at an angle of -10° to the optical axis ($y=0$). Such a condition adds an extra planar phase front that interferes with the asymmetric phase front of the plasmonic lens, leading to a larger bending angle off the axial direction. Fig. 4-21(b) shows that the bending angle increases from 5° to 17° . In this case, the beam can be shifted nearly $1\ \mu\text{m}$ in the y -direction, which is large enough for applications such in plasmonic communications and nanofabrication. Our simulation results also indicate that when the incident angle is 10° above the optical axis [Fig. 4-21(c)], the light beam is deflected toward the optical axis, but not enough to cross it. The deflection angle is observed to be -6° [Fig. 4-21(d)].

The slits used in our three plasmonic lens designs are either rectangular or trapezoid. These plain geometries guarantee the simplicity in fabrication using the FIB technique. One can imagine a plasmonic lens with continuous varying tapered slits would act differently and perhaps have better efficiency and larger bending effect than the proposed lenses. This tapered lens, however, brings complexity to fabrication and thus is not considered in this paper. In addition, the proposed lenses may be further optimized by fine-tuning the geometrical parameters (such as width, length, and spacing of the slits) but that is purely engineering and is beyond the scope of this paper.

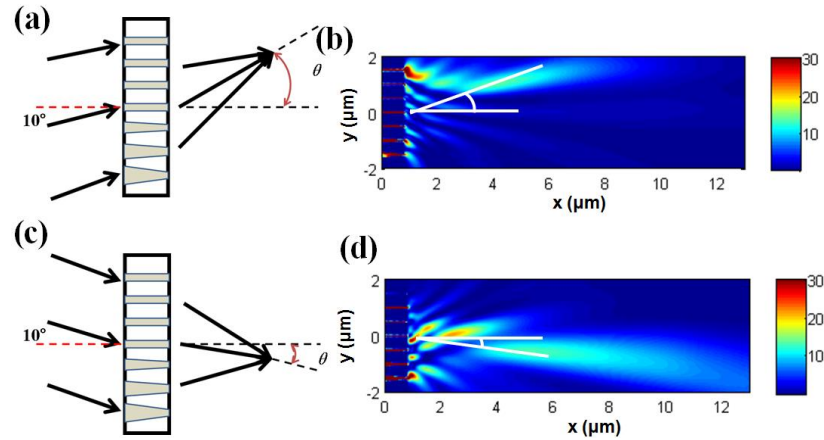


Figure 4-21. Influence of different incident angles on the bending effects of Lens III. The red dashed lines denote the phase front change caused by both incident light and plasmonic lenses. (a) Schematic of light incidence at an angle of -10° to the optical axis; (b) Simulation results corresponding to (a). (c) Schematic of light incidence at an angle of 10° to the optical axis. (d) Simulation results corresponding to (c).

Section Summary

I have designed three different plasmonic lens structures to achieve the directional tuning of light. Based on our FDTD simulation, when the incident light is normal to the lens surface, deflection angles of 8° , 3° , and 5° in the far field have been achieved in the three designs, respectively. We also show that with light incident at 10° below the optical axis, a deflection up to 17° in the far field can be achieved. Compared with existing plasmonic lenses [355, 356] that can bend light, proposed lens designs have advantages in bending range, ease of fabrication, and capability to perform in the far field. Proposed plasmonic lenses will be valuable in applications such as plasmonic circuits and photonic communication.

4.3. Summary

In this section, I have discussed my works on constructing active and passive plasmonic devices. Active plasmonic devices are achieved through mechanically stretching elastic substrate

that supports engineered plasmonic nanostructure, and with the help from active mediums such as liquid crystal molecules. The passive plasmonic devices such as plasmonic lenses and metamaterials will alter the light propagation at subwavelength scale under different configurations. Those knowledge are essential to understand the basics for constructions of engineering plasmonic devices.

Chapter 5

Summary and Perspective

The word “Plamomics” appeared in the past decade denotes a rapid developing field describing the novel optical physics concerning light and metal nanostructure interactions at nanoscale. As a very important research branch in nanophotonics and general optics, plasmonics has revealed lots of exciting discoveries on various novel optical phenomena and material properties at the nanometer scale or subwavelength scale. Those knowledge become the building foundations of the whole plasmonic research field, and provided important guidelines on developing novel plasmonic devices benefitting from the exciting discoveries. Although researchers vision the very promising future of plasmonics, the current major driven force pushing the field to advance still focuses on exploring new physics and barely touches the even fancy side of the application-based technology development. Part of the reason is that plasmonics itself is a broad field to explore, and there is little effort to be spared to seek interdisciplinary problems and solve them. With my peer researchers focusing on discovering fundamental plasmonic physics, I took a different route contributing this field by bridging it to another field of research or targeting to certain applications. In my efforts of past five years along this route, I was capable of demonstrating the start of a new research direction called “Engineering Plasmonics”. “Engineering Plasmonics” coined by myself is not a new research field different much from the current plasmonics, but emphasizing its application-oriented objective. The huge potentials of engineering plasmonics on solving interdisciplinary challenges are very encouraging, and engineering plasmonic method developed based on some of the existing plamonic knowledge

have been proven as very effective ways to solve suitable interdisciplinary challenges. However, it requires the researchers to acquire enough knowledge out of their fields, and be able to identify significant problems and provide effective solutions.

At the beginning of my Ph.D studies, I have been focusing on developing simple plasmonic devices based on fundamental plasmonic optical physics. The focus of my research was later shifted on addressing practical related applications such as solar energy harvesting and color display technology. During the past two years, I had the honor receiving guidance from world famous chemist Dr. Stephen Benkovic working on developing single-molecule techniques to discover fundamental biology concerning DNA replication process. As summarized reversely in this dissertation, it took a long path and many efforts to apply existing knowledge to solve interdisciplinary challenges; it is a fun process to learn and the results are rewarded. My research over the past five years has led to 36 journal publications on various peer reviewed journals, with the major research focus on three topics discussed in this dissertation: (1) Engineering Plasmonics for Single-Molecule Investigations: T4 DNA Replication Studies; (2) Engineering Plasmonics for Practical Applications: Solar Energy Harvest and Color Pixel Display; and (3) Engineering Plasmonics: Manipulating Light at Nanoscale using Active and Passive Plasmonic Devices.

As I states above, Engineering Plasmonics is not a whole new research field, but a research direction focusing on plasmonic based applications. It is attracting more attentions as researchers realize more and more on the huge potentials of plasmonic research on addressing challenges on energy deficiency, clinical diagnostics and therapeutics, etc. I will discuss some of my opinions and perspectives on the forth-coming opportunities and challenges in this direction in the following paragraphs.

Single-molecule techniques based on plasmonics and nanophotonics: Single-molecule techniques are recently developed to interrogate single-molecule dynamics, and are only possible accompanied with precise single-molecule manipulation techniques and single-molecule

detection techniques. Biomolecules with their sizes down to several nanometers or even less are extremely hard to manipulate and detect using conventional methods. Plasmonics has its uniqueness involving both nanoscale structures and light as the probing sources at the same time. In terms of scale, the solid state nanostructure has its scale mostly close to the dimensions of single molecules. As for probing light to detect fluorescence labeled molecule unites, the interaction between incident light and nanostructures serve as natural source during the detection. Successful single-molecule manipulation techniques such as optical tweezers and magnetic tweezers need to rely on inter-mediums such as beads to manipulate biomolecules indirectly, introducing new plasmonic techniques to assist single-molecule manipulations is one of the key problem need to be addressed. Nanofabricated DNA racks and DNA bridges are my first attempts to answer this challenge. The DNA racks capability of separating and stretching individual DNA molecules without flow impacts and disturbance have proven to be very effective ways of manipulating single-molecule at the first stage. While the issue of reaction surface affecting the single-molecule dynamics observation has not yet been relieved, our on-going project developing DNA bridge across separated quartz edges would be a perfect solution to elevate the DNA molecules away from the surface, thus eliminating the surface impacts during the single-molecule reactions. The future techniques enabled by plasmonics to manipulate single molecules directly without inter-mediums are expected and they may be the future towards high-precision single-molecule dynamic studies.

Label-free single-molecule studies is another significant topic that concerns single-molecule detections, current existing single-molecule detection techniques are mostly fluorescence based, and the single molecule targets are biomolecule-dye conjugates instead of the specific target molecules. Single-molecule surface enhanced raman scattering (SERS) allows to map the vibration signals from chemical bonds inside single molecules, but the process happens much slower than the time scale that single-molecule dynamics would occur. Although our work

of nanowell array based single-molecule detection method can much improve the single-molecule detection sensitivity based on fluorescent signals, the most significant challenge encountered is still the surface impact affecting the behavior of single molecules. However, label-free single-molecule detection without fluorescence label is a significant enough topic that will revolutionize the whole field of single-molecule studies.

Although we developed plasmonic absorbers to be used in solar energy collection that would reduce the cost and improve the efficiency of current solar cells, their applications can be easily extended to military research and biological research, assisting infrared or microwave coating on aircrafts or highly effective biological sensors based on optical absorptions. After our work demonstrating the effort of expanding the narrow absorption band in the first generation of plasmonic absorbers, following research works and activities have reported the possibility to further expand the working range of plasmonic absorbers to both the visible range and longer wavelength range. The current leading effort in this research direction is still in the process of improving the device performance; specifically targeting the energy storage methods to improved the energy storage efficiency. The challenges is to store and transfer the energy collected after they are absorbed but before they dissipate in the form of heat or other waste channels. How to incorporate such parts into the existing plasmonic absorbers is the immediate question we need to answer following the path of using plasmonic absorber for the manufacture of high efficiency solar cells.

While the color pixel techniques experienced a huge driven force by the rapid development of smartphones, plasmonic color filter techniques will take the challenges from many other peering techniques fighting for its spot on the market. As Apple pushed out its new product line of iPhone 6 and iPhone 6 Plus, that has further reduce the color pixel size to around 1 micrometer and termed the technique as “retina HD”. The increased pixel density demands much sophisticated driven circuits behind the display to make it function properly. Our plasmonic color

pixels can easily compete with “retina HD” in terms of the pixel size, but developing a complicated optical driven circuit to use our plasmonic pixels is still in the very early stage. In parallel, making use of the uniqueness of engineering plasmonics to allow new functions in one single color pixel unit shows very promising futures in the projection display techniques such as DLP and DMD.

Plasmonic physics and simple plasmonic device are the fundamentals of the whole plasmonic researches, and have enabled all the possibilities we discussed above. We see the co-existence of challenges and unprecedented opportunities at the same time. With the enormous knowledge base of current plasmonics and on-going research to explore in-depth along this direction, the most significant challenges lying before us is not inside this field itself, but how to utilize them for applications and address interdisciplinary challenges. I see the clear boundaries among different research fields fade along with the expanding knowledge and recognitions of each individual field. I envision the merging of the knowledge of several field and collaborative efforts on addressing the most challenging issues we faced together as human beings instead of individuals or individual research field, where engineering plasmonics will play its most significant role during the process.

References

1. Atwater, H.A., *The promise of plasmonics*. Scientific American, 2007. **296**(4): p. 56-63.
2. Catrysse, P.B., *Plasmonics - Beaming light into the nanoworld*. Nature Physics, 2007. **3**(12): p. 839-840.
3. Ozbay, E., *Plasmonics: Merging photonics and electronics at nanoscale dimensions*. Science, 2006. **311**(5758): p. 189-193.
4. Pile, D., et al., *Practical plasmonics*. Nature Photonics, 2009. **3**(4): p. 236-236.
5. Pile, D. and J. Krenn, *Perspective on plasmonics*. Nature Photonics, 2012. **6**(11): p. 714-715.
6. Visser, T.D., *Plasmonics - Surface plasmons at work?* Nature Physics, 2006. **2**(8): p. 509-510.
7. Chen, X.Z., et al., *Macroscopic invisibility cloaking of visible light*. Nature Communications, 2011. **2**.
8. Fridman, M., et al., *Demonstration of temporal cloaking*. Nature, 2012. **481**(7379): p. 62-65.
9. Jenkins, A., *Optical cloaking - A many-layered solution*. Nature Photonics, 2008. **2**(5): p. 270-270.
10. Schittny, R., et al., *Invisibility cloaking in a diffusive light scattering medium*. Science, 2014. **345**(6195): p. 427-429.
11. Smith, D.R., *A cloaking coating for murky media*. Science, 2014. **345**(6195): p. 384-385.
12. Gandra, N., et al., *Plasmonic Planet-Satellite Analogues: Hierarchical Self-Assembly of Gold Nanostructures*. Nano Letters, 2012. **12**(5): p. 2645-2651.
13. Sebba, D.S., et al., *Reconfigurable core-satellite nanoassemblies as molecularly-driven plasmonic switches*. Nano Letters, 2008. **8**(7): p. 1803-1808.
14. Yoon, J.H., J. Lim, and S. Yoon, *Controlled Assembly and Plasmonic Properties of Asymmetric Core-Satellite Nanoassemblies*. Acs Nano, 2012. **6**(8): p. 7199-7208.
15. Zheng, Y.H., et al., *DNA-Directed Self-Assembly of Core-Satellite Plasmonic Nanostructures: A Highly Sensitive and Reproducible Near-IR SERS Sensor*. Advanced Functional Materials, 2013. **23**(12): p. 1519-1526.
16. Liu, Y.M. and X. Zhang, *Metasurfaces for manipulating surface plasmons*. Applied Physics Letters, 2013. **103**(14).
17. Luo, Y., J.B. Pendry, and A. Aubry, *Surface Plasmons and Singularities*. Nano Letters, 2010. **10**(10): p. 4186-4191.
18. Zhang, J.X. and L.D. Zhang, *Nanostructures for surface plasmons*. Advances in Optics and Photonics, 2012. **4**(2): p. 157-321.
19. Raether, H., *Surface plasmons on smooth and rough surfaces and on gratings*. 1988: Springer.
20. Hutter, E. and J.H. Fendler, *Exploitation of Localized Surface Plasmon Resonance*. Advanced Materials, 2004. **16**(19): p. 1685-1706.
21. Szunerits, S. and R. Boukherroub, *Sensing using localised surface plasmon resonance sensors*. Chemical Communications, 2012. **48**(72): p. 8999-9010.
22. Zhang, X., et al., *Experimental and Theoretical Investigation of the Distance Dependence of Localized Surface Plasmon Coupled Forster Resonance Energy Transfer*. Acs Nano, 2014. **8**(2): p. 1273-1283.
23. Itoh, T. and R. Mittra, *Wood Anomalies in Diffraction from Strip Grating*. Ieee Transactions on Microwave Theory and Techniques, 1970. **Mt18**(1): p. 54-&.

24. Sarrazin, M., J.P. Vigneron, and J.M. Vigoureux, *Role of Wood anomalies in optical properties of thin metallic films with a bidimensional array of subwavelength holes*. Physical Review B, 2003. **67**(8).
25. Simon, J.M., M.C. Simon, and M.T. Garea, *Phase-Behavior in Wood Anomalies*. Applied Optics, 1986. **25**(12): p. 1872-1873.
26. Twersky, V., *On a Multiple Scattering Theory of the Grating and the Wood Anomalies*. Physical Review, 1952. **85**(4): p. 715-716.
27. Lee, K.L. and P.K. Wei, *Enhancing surface plasmon detection using ultrasmall nanoslits and a multispectral integration method*. Small, 2010. **6**(17): p. 1900-7.
28. Zou, S. and G.C. Schatz, *Theoretical studies of plasmon resonances in one-dimensional nanoparticle chains: narrow lineshapes with tunable widths*. Nanotechnology, 2006. **17**(11): p. 2813-2820.
29. Markel, V. and A. Sarychev, *Propagation of surface plasmons in ordered and disordered chains of metal nanospheres*. Physical Review B, 2007. **75**(8).
30. Augu  , B. and W. Barnes, *Collective Resonances in Gold Nanoparticle Arrays*. Physical Review Letters, 2008. **101**(14).
31. Zou, S., N. Janel, and G.C. Schatz, *Silver nanoparticle array structures that produce remarkably narrow plasmon lineshapes*. J Chem Phys, 2004. **120**(23): p. 10871-5.
32. Zou, S. and G.C. Schatz, *Response to "Comment on 'Silver nanoparticle array structures that produce remarkable narrow plasmon line shapes' "* [J. Chem. Phys. 120, 10871 (2004)]. The Journal of Chemical Physics, 2005. **122**(9): p. 097102.
33. Markel, V.A., *Divergence of dipole sums and the nature of non-Lorentzian exponentially narrow resonances in one-dimensional periodic arrays of nanospheres*. Journal of Physics B: Atomic, Molecular and Optical Physics, 2005. **38**(7): p. L115-L121.
34. Xie, X.S., et al., *Single-molecule approach to molecular biology in living bacterial cells*. Annu Rev Biophys, 2008. **37**: p. 417-44.
35. Zhao, Y., et al., *Dark-field illumination on zero-mode waveguide/microfluidic hybrid chip reveals T4 replisomal protein interactions*. Nano Lett, 2014. **14**(4): p. 1952-60.
36. Johnson, P.B. and R.W. Christy, *Optical Constants of the Noble Metals*. Physical Review B, 1972. **6**(12): p. 4370-4379.
37. Lu, H.P., L. Xun, and X.S. Xie, *Single-molecule enzymatic dynamics*. Science, 1998. **282**(5395): p. 1877-82.
38. van Oijen, A.M., *Single-molecule approaches to characterizing kinetics of biomolecular interactions*. Curr Opin Biotechnol, 2011. **22**(1): p. 75-80.
39. Forth, S., et al., *Torque measurement at the single-molecule level*. Annu Rev Biophys, 2013. **42**: p. 583-604.
40. Bai, L., T.J. Santangelo, and M.D. Wang, *Single-molecule analysis of RNA polymerase transcription*. Annu Rev Biophys Biomol Struct, 2006. **35**: p. 343-60.
41. Hilario, J. and S.C. Kowalczykowski, *Visualizing protein-DNA interactions at the single-molecule level*. Curr Opin Chem Biol, 2010. **14**(1): p. 15-22.
42. Joo, C., et al., *Advances in single-molecule fluorescence methods for molecular biology*. Annual Review of Biochemistry, 2008. **77**: p. 51-76.
43. Funatsu, T., et al., *Imaging of single fluorescent molecules and individual ATP turnovers by single myosin molecules in aqueous solution*. Nature, 1995. **374**(6522): p. 555-9.
44. Giepmans, B.N., et al., *The fluorescent toolbox for assessing protein location and function*. Science, 2006. **312**(5771): p. 217-24.
45. Zhuang, X., et al., *A single-molecule study of RNA catalysis and folding*. Science, 2000. **288**(5473): p. 2048-51.

46. Ha, T., *Single-molecule fluorescence resonance energy transfer*. Methods, 2001. **25**(1): p. 78-86.
47. Min, W., et al., *Fluctuating enzymes: lessons from single-molecule studies*. Acc Chem Res, 2005. **38**(12): p. 923-31.
48. Finkelstein, I.J. and E.C. Greene, *Molecular traffic jams on DNA*. Annu Rev Biophys, 2013. **42**: p. 241-63.
49. Finkelstein, I.J., M.L. Visnapuu, and E.C. Greene, *Single-molecule imaging reveals mechanisms of protein disruption by a DNA translocase*. Nature, 2010. **468**(7326): p. 983-7.
50. Gorman, J. and E.C. Greene, *Visualizing one-dimensional diffusion of proteins along DNA*. Nat Struct Mol Biol, 2008. **15**(8): p. 768-74.
51. Ha, T., *Single-molecule approaches embrace molecular cohorts*. Cell, 2013. **154**(4): p. 723-6.
52. Ha, T., A.G. Kozlov, and T.M. Lohman, *Single-molecule views of protein movement on single-stranded DNA*. Annu Rev Biophys, 2012. **41**: p. 295-319.
53. Ha, T. and P. Tinnefeld, *Photophysics of fluorescent probes for single-molecule biophysics and super-resolution imaging*. Annu Rev Phys Chem, 2012. **63**: p. 595-617.
54. Roy, R., S. Hohng, and T. Ha, *A practical guide to single-molecule FRET*. Nat Methods, 2008. **5**(6): p. 507-16.
55. Huang, B., M. Bates, and X. Zhuang, *Super-resolution fluorescence microscopy*. Annu Rev Biochem, 2009. **78**: p. 993-1016.
56. Fernandez-Suarez, M. and A.Y. Ting, *Fluorescent probes for super-resolution imaging in living cells*. Nat Rev Mol Cell Biol, 2008. **9**(12): p. 929-43.
57. Hell, S.W., M. Dyba, and S. Jakobs, *Concepts for nanoscale resolution in fluorescence microscopy*. Curr Opin Neurobiol, 2004. **14**(5): p. 599-609.
58. Klar, T.A. and S.W. Hell, *Subdiffraction resolution in far-field fluorescence microscopy*. Optics Letters, 1999. **24**(14): p. 954.
59. Zhang, X. and Z. Liu, *Superlenses to overcome the diffraction limit*. Nat Mater, 2008. **7**(6): p. 435-41.
60. Liu, Z., et al., *Far-field optical hyperlens magnifying sub-diffraction-limited objects*. Science, 2007. **315**(5819): p. 1686.
61. Lu, D. and Z. Liu, *Hyperlenses and metalenses for far-field super-resolution imaging*. Nat Commun, 2012. **3**: p. 1205.
62. Rho, J., et al., *Spherical hyperlens for two-dimensional sub-diffractional imaging at visible frequencies*. Nat Commun, 2010. **1**: p. 143.
63. Wei, F. and Z. Liu, *Plasmonic structured illumination microscopy*. Nano Lett, 2010. **10**(7): p. 2531-6.
64. Zhu, P. and H.G. Craighead, *Zero-mode waveguides for single-molecule analysis*. Annu Rev Biophys, 2012. **41**: p. 269-93.
65. Moran-Mirabal, J.M. and H.G. Craighead, *Zero-mode waveguides: sub-wavelength nanostructures for single molecule studies at high concentrations*. Methods, 2008. **46**(1): p. 11-7.
66. Huang, B., H. Babcock, and X. Zhuang, *Breaking the diffraction barrier: super-resolution imaging of cells*. Cell, 2010. **143**(7): p. 1047-58.
67. Huang, B., et al., *Three-dimensional super-resolution imaging by stochastic optical reconstruction microscopy*. Science, 2008. **319**(5864): p. 810-3.
68. Bates, M., B. Huang, and X. Zhuang, *Super-resolution microscopy by nanoscale localization of photo-switchable fluorescent probes*. Curr Opin Chem Biol, 2008. **12**(5): p. 505-14.

69. Betzig, E., et al., *Imaging intracellular fluorescent proteins at nanometer resolution*. Science, 2006. **313**(5793): p. 1642-5.
70. Zhao, Y., et al., *Beam bending via plasmonic lenses*. Opt Express, 2010. **18**(22): p. 23458-65.
71. Zhao, C., et al., *A reconfigurable plasmofluidic lens*. Nat Commun, 2013. **4**: p. 2305.
72. Tinnefeld, P., *Single-molecule detection: Breaking the concentration barrier*. Nat Nanotechnol, 2013. **8**(7): p. 480-2.
73. Loveland, A.B., et al., *A general approach to break the concentration barrier in single-molecule imaging*. Nat Methods, 2012. **9**(10): p. 987-92.
74. Patterson, G., et al., *Superresolution imaging using single-molecule localization*. Annu Rev Phys Chem, 2010. **61**: p. 345-67.
75. Rust, M.J., M. Bates, and X. Zhuang, *Sub-diffraction-limit imaging by stochastic optical reconstruction microscopy (STORM)*. Nat Methods, 2006. **3**(10): p. 793-5.
76. Ji, N., et al., *Advances in the speed and resolution of light microscopy*. Curr Opin Neurobiol, 2008. **18**(6): p. 605-16.
77. Hell, S.W. and J. Wichmann, *Breaking the diffraction resolution limit by stimulated emission: stimulated-emission-depletion fluorescence microscopy*. Optics Letters, 1994. **19**(11): p. 780.
78. Sahl, S.J. and W. Moerner, *Super-resolution fluorescence imaging with single molecules*. Curr Opin Struct Biol, 2013. **23**(5): p. 778-87.
79. Levene, M.J., et al., *Zero-mode waveguides for single-molecule analysis at high concentrations*. Science, 2003. **299**(5607): p. 682-6.
80. Ibach, J. and S. Brakmann, *Sequencing single DNA molecules in real time*. Angew Chem Int Ed Engl, 2009. **48**(26): p. 4683-5.
81. Eid, J., et al., *Real-time DNA sequencing from single polymerase molecules*. Science, 2009. **323**(5910): p. 133-8.
82. Wang, X., et al., *Single-crystal X-ray diffraction, isolated-molecule and cluster electronic structure calculations, and scanning electron microscopy in an organic solid: models for intramolecular motion in 4,4'-dimethoxybiphenyl*. Chemphyschem, 2012. **13**(8): p. 2082-9.
83. Zentgraf, T., et al., *Plasmonic Luneburg and Eaton lenses*. Nat Nanotechnol, 2011. **6**(3): p. 151-5.
84. Etchegoin, P.G. and E.C. Le Ru, *A perspective on single molecule SERS: current status and future challenges*. Phys Chem Chem Phys, 2008. **10**(40): p. 6079-89.
85. Le Ru, E.C. and P.G. Etchegoin, *Single-molecule surface-enhanced Raman spectroscopy*. Annu Rev Phys Chem, 2012. **63**: p. 65-87.
86. Nie, S., *Probing Single Molecules and Single Nanoparticles by Surface-Enhanced Raman Scattering*. Science, 1997. **275**(5303): p. 1102-1106.
87. Stranahan, S.M. and K.A. Willets, *Super-resolution optical imaging of single-molecule SERS hot spots*. Nano Lett, 2010. **10**(9): p. 3777-84.
88. Hess, S.T., T.P. Girirajan, and M.D. Mason, *Ultra-high resolution imaging by fluorescence photoactivation localization microscopy*. Biophys J, 2006. **91**(11): p. 4258-72.
89. Manosas, M., et al., *Collaborative coupling between polymerase and helicase for leading-strand synthesis*. Nucleic Acids Res, 2012. **40**(13): p. 6187-98.
90. Revyakin, A., et al., *Abortive initiation and productive initiation by RNA polymerase involve DNA scrunching*. Science, 2006. **314**(5802): p. 1139-43.
91. van Loenhout, M.T., M.V. de Grunt, and C. Dekker, *Dynamics of DNA supercoils*. Science, 2012. **338**(6103): p. 94-7.

92. Shergill, B., et al., *Optical tweezers studies on Notch: single-molecule interaction strength is independent of ligand endocytosis*. Dev Cell, 2012. **22**(6): p. 1313-20.
93. Capitanio, M. and F.S. Pavone, *Interrogating biology with force: single molecule high-resolution measurements with optical tweezers*. Biophys J, 2013. **105**(6): p. 1293-303.
94. Comstock, M.J., T. Ha, and Y.R. Chemla, *Ultrahigh-resolution optical trap with single-fluorophore sensitivity*. Nat Methods, 2011. **8**(4): p. 335-40.
95. Fazio, T., et al., *DNA curtains and nanoscale curtain rods: high-throughput tools for single molecule imaging*. Langmuir, 2008. **24**(18): p. 10524-31.
96. Graneli, A., et al., *Organized arrays of individual DNA molecules tethered to supported lipid bilayers*. Langmuir, 2006. **22**(1): p. 292-9.
97. Gorman, J., et al., *Single-molecule imaging reveals target-search mechanisms during DNA mismatch repair*. Proc Natl Acad Sci U S A, 2012. **109**(45): p. E3074-83.
98. Foquet, M., et al., *Improved fabrication of zero-mode waveguides for single-molecule detection*. Journal of Applied Physics, 2008. **103**(3): p. 034301.
99. Clarke, J., et al., *Continuous base identification for single-molecule nanopore DNA sequencing*. Nat Nanotechnol, 2009. **4**(4): p. 265-70.
100. Branton, D., et al., *The potential and challenges of nanopore sequencing*. Nat Biotechnol, 2008. **26**(10): p. 1146-53.
101. Wanunu, M., et al., *Rapid electronic detection of probe-specific microRNAs using thin nanopore sensors*. Nat Nanotechnol, 2010. **5**(11): p. 807-14.
102. Uemura, S., et al., *Real-time tRNA transit on single translating ribosomes at codon resolution*. Nature, 2010. **464**(7291): p. 1012-7.
103. Ibanescu, M., et al., *Microcavity confinement based on an anomalous zero group-velocity waveguide mode*. Optics Letters, 2005. **30**(5): p. 552-554.
104. Korlach, J., et al., *Selective aluminum passivation for targeted immobilization of single DNA polymerase molecules in zero-mode waveguide nanostructures*. Proceedings of the National Academy of Sciences of the United States of America, 2008. **105**(4): p. 1176-1181.
105. Lee, J., et al., *A dual-mode waveguide pseudoelliptic filter with zero-shifting properties*. Microwave and Optical Technology Letters, 2005. **47**(4): p. 357-359.
106. Miyake, T., et al., *Real-time imaging of single-molecule fluorescence with a zero-mode waveguide for the analysis of protein-protein interaction*. Analytical Chemistry, 2008. **80**(15): p. 6018-6022.
107. Richards, C.I., et al., *Live-Cell Imaging of Single Receptor Composition Using Zero-Mode Waveguide Nanostructures*. Nano Letters, 2012. **12**(7): p. 3690-3694.
108. Tanii, T., et al., *Improving zero-mode waveguide structure for enhancing signal-to-noise ratio of real-time single-molecule fluorescence imaging: A computational study*. Physical Review E, 2013. **88**(1).
109. Wada, J., et al., *Fabrication of Zero-Mode Waveguide by Ultraviolet Nanoimprint Lithography Lift-Off Process*. Japanese Journal of Applied Physics, 2011. **50**(6).
110. Zhao, J., S.P. Branagan, and P.W. Bohn, *Single-Molecule Enzyme Dynamics of Monomeric Sarcosine Oxidase in a Gold-Based Zero-Mode Waveguide*. Applied Spectroscopy, 2012. **66**(2): p. 163-169.
111. Samiee, K.T., et al., *Zero mode waveguides for single-molecule spectroscopy on lipid membranes*. Biophys J, 2006. **90**(9): p. 3288-99.
112. Edel, J.B., et al., *High spatial resolution observation of single-molecule dynamics in living cell membranes*. Biophys J, 2005. **88**(6): p. L43-5.

113. Korlach, J., et al., *Selective aluminum passivation for targeted immobilization of single DNA polymerase molecules in zero-mode waveguide nanostructures*. Proc Natl Acad Sci U S A, 2008. **105**(4): p. 1176-81.
114. Liao, D., et al., *Single molecule correlation spectroscopy in continuous flow mixers with zero-mode waveguides*. Optics Express, 2008. **16**(14): p. 10077.
115. Sameshima, T., et al., *Single-molecule study on the decay process of the football-shaped GroEL-GroES complex using zero-mode waveguides*. J Biol Chem, 2010. **285**(30): p. 23159-64.
116. Richards, C.I., et al., *Live-cell imaging of single receptor composition using zero-mode waveguide nanostructures*. Nano Lett, 2012. **12**(7): p. 3690-4.
117. Zhao, J., S.P. Branagan, and P.W. Bohn, *Single-molecule enzyme dynamics of monomeric sarcosine oxidase in a gold-based zero-mode waveguide*. Appl Spectrosc, 2012. **66**(2): p. 163-9.
118. Chen, J., et al., *Coordinated conformational and compositional dynamics drive ribosome translocation*. Nat Struct Mol Biol, 2013. **20**(6): p. 718-27.
119. Zhao, Y., et al., *Lab-on-a-chip technologies for single-molecule studies*. Lab Chip, 2013. **13**(12): p. 2183-98.
120. Miyake, T., et al., *Real-time imaging of single-molecule fluorescence with a zero-mode waveguide for the analysis of protein-protein interaction*. Anal Chem, 2008. **80**(15): p. 6018-22.
121. Teng, C.H., et al., *Fabrication of nanoscale zero-mode waveguides using microlithography for single molecule sensing*. Nanotechnology, 2012. **23**(45): p. 455301.
122. Kinz-Thompson, C.D., et al., *Robustly Passivated, Gold Nanoaperture Arrays for Single-Molecule Fluorescence Microscopy*. ACS Nano, 2013.
123. Lundquist, P.M., et al., *Parallel confocal detection of single molecules in real time*. Optics Letters, 2008. **33**(9): p. 1026.
124. Whitesides, G.M., *The origins and the future of microfluidics*. Nature, 2006. **442**(7101): p. 368-73.
125. Zhao, Y., et al., *Optofluidic imaging: now and beyond*. Lab Chip, 2013. **13**(1): p. 17-24.
126. Yang, S., et al., *Microfluidic synthesis of multifunctional Janus particles for biomedical applications*. Lab Chip, 2012. **12**(12): p. 2097-102.
127. Moerner, W.E. and D.P. Fromm, *Methods of single-molecule fluorescence spectroscopy and microscopy*. Review of Scientific Instruments, 2003. **74**(8): p. 3597.
128. Patterson, G.H. and D.W. Piston, *Photobleaching in Two-Photon Excitation Microscopy*. Biophysical Journal, 2000. **78**(4): p. 2159-2162.
129. Benkovic, S.J., A.M. Valentine, and F. Salinas, *Replisome-mediated DNA replication*. Annu Rev Biochem, 2001. **70**: p. 181-208.
130. Arumugam, S.R., T.H. Lee, and S.J. Benkovic, *Investigation of stoichiometry of T4 bacteriophage helicase loader protein (gp59)*. J Biol Chem, 2009. **284**(43): p. 29283-9.
131. Delagoutte, E. and P.H. von Hippel, *Mechanistic studies of the T4 DNA (gp41) replication helicase: functional interactions of the C-terminal Tails of the helicase subunits with the T4 (gp59) helicase loader protein*. J Mol Biol, 2005. **347**(2): p. 257-75.
132. Zhang, Z., et al., *Assembly of the bacteriophage T4 primosome: single-molecule and ensemble studies*. Proc Natl Acad Sci U S A, 2005. **102**(9): p. 3254-9.
133. Lefebvre, S.D. and S.W. Morrical, *Interactions of the bacteriophage T4 gene 59 protein with single-stranded polynucleotides: binding parameters and ion effects*. J Mol Biol, 1997. **272**(3): p. 312-26.
134. Spiering, M.M., S.W. Nelson, and S.J. Benkovic, *Repetitive lagging strand DNA synthesis by the bacteriophage T4 replisome*. Mol Biosyst, 2008. **4**(11): p. 1070-4.

135. Perumal, S.K., et al., *How a holoenzyme for DNA replication is formed*. Proc Natl Acad Sci U S A, 2013. **110**(1): p. 99-104.
136. Lee, W., et al., *A single-molecule view of the assembly pathway, subunit stoichiometry, and unwinding activity of the bacteriophage T4 primosome (helicase-primase) complex*. Biochemistry, 2013. **52**(18): p. 3157-70.
137. Perumal, S.K., et al., *Single-molecule studies of DNA replisome function*. Biochim Biophys Acta, 2010. **1804**(5): p. 1094-112.
138. Yang, J., et al., *The application of a minicircle substrate in the study of the coordinated T4 DNA replication*. J Biol Chem, 2003. **278**(50): p. 49828-38.
139. Xi, J., et al., *Interaction between the T4 helicase-loading protein (gp59) and the DNA polymerase (gp43): a locking mechanism to delay replication during replisome assembly*. Biochemistry, 2005. **44**(7): p. 2305-18.
140. Bleuit, J.S., et al., *Mediator proteins orchestrate enzyme-ssDNA assembly during T4 recombination-dependent DNA replication and repair*. Proc Natl Acad Sci U S A, 2001. **98**(15): p. 8298-305.
141. Hinerman, J.M., J.D. Dignam, and T.C. Mueser, *Models for the binary complex of bacteriophage T4 gp59 helicase loading protein: gp32 single-stranded DNA-BINDING protein and ternary complex with pseudo-Y junction DNA*. J Biol Chem, 2012. **287**(22): p. 18608-17.
142. Nelson, S.W., J. Yang, and S.J. Benkovic, *Site-directed mutations of T4 helicase loading protein (gp59) reveal multiple modes of DNA polymerase inhibition and the mechanism of unlocking by gp41 helicase*. J Biol Chem, 2006. **281**(13): p. 8697-706.
143. Ha, T., et al., *Probing the interaction between two single molecules: Fluorescence resonance energy transfer between a single donor and a single acceptor*. Proceedings of the National Academy of Sciences of the United States of America, 1996. **93**(13): p. 6264-6268.
144. Sternberg, S.H., et al., *DNA interrogation by the CRISPR RNA-guided endonuclease Cas9*. Nature, 2014. **507**(7490): p. 62-7.
145. Nelson, S.W. and S.J. Benkovic, *The T4 phage UvsW protein contains both DNA unwinding and strand annealing activities*. J Biol Chem, 2007. **282**(1): p. 407-16.
146. Carles-Kinch, K., J.W. George, and K.N. Kreuzer, *Bacteriophage T4 UvsW protein is a helicase involved in recombination, repair and the regulation of DNA replication origins*. EMBO J, 1997. **16**(13): p. 4142-51.
147. Manosas, M., et al., *RecG and UvsW catalyse robust DNA rewinding critical for stalled DNA replication fork rescue*. Nat Commun, 2013. **4**: p. 2368.
148. Perumal, S.K., S.W. Nelson, and S.J. Benkovic, *Interaction of T4 UvsW helicase and single-stranded DNA binding protein gp32 through its carboxy-terminal acidic tail*. J Mol Biol, 2013. **425**(16): p. 2823-39.
149. Zhang, B., et al., *Polarization-independent dual-band infrared perfect absorber based on a metal-dielectric-metal elliptical nanodisk array*. Opt Express, 2011. **19**(16): p. 15221-8.
150. Zhao, Y., et al., *Light-driven tunable dual-band plasmonic absorber using liquid-crystal-coated asymmetric nanodisk array*. Applied Physics Letters, 2012. **100**(5): p. 053119.
151. Si, G., et al., *Reflective plasmonic color filters based on lithographically patterned silver nanorod arrays*. Nanoscale, 2013. **5**(14): p. 6243-8.
152. Si, G., et al., *Annular aperture array based color filter*. Applied Physics Letters, 2011. **99**(3): p. 033105.
153. Catchpole, K.R. and A. Polman, *Plasmonic solar cells*. Optics Express, 2008. **16**(26): p. 21793.

154. Munday, J.N. and H.A. Atwater, *Large integrated absorption enhancement in plasmonic solar cells by combining metallic gratings and antireflection coatings*. Nano Lett, 2011. **11**(6): p. 2195-201.
155. Nakayama, K., K. Tanabe, and H.A. Atwater, *Plasmonic nanoparticle enhanced light absorption in GaAs solar cells*. Applied Physics Letters, 2008. **93**(12): p. 121904.
156. Yen, T.J., et al., *Terahertz magnetic response from artificial materials*. Science, 2004. **303**(5663): p. 1494-6.
157. Hao, J., et al., *High performance optical absorber based on a plasmonic metamaterial*. Applied Physics Letters, 2010. **96**(25): p. 251104.
158. Xiao, S., et al., *Tunable magnetic response of metamaterials*. Applied Physics Letters, 2009. **95**(3): p. 033115.
159. Lee, J.H., et al., *Direct visualization of optical frequency invisibility cloak based on silicon nanorod array*. Optics Express, 2009. **17**(15): p. 12922.
160. Yu, Z., et al., *Design of midinfrared photodetectors enhanced by surface plasmons on grating structures*. Applied Physics Letters, 2006. **89**(15): p. 151116.
161. Rosenberg, J., et al., *A multispectral and polarization-selective surface-plasmon resonant midinfrared detector*. Applied Physics Letters, 2009. **95**(16): p. 161101.
162. Zhu, S., et al., *A localized surface plasmon resonance nanosensor based on rhombic Ag nanoparticle array*. Sensors and Actuators B: Chemical, 2008. **134**(1): p. 193-198.
163. Liu, N., et al., *Infrared perfect absorber and its application as plasmonic sensor*. Nano Lett, 2010. **10**(7): p. 2342-8.
164. Liu, C.H., et al., *Bimetallic structure fabricated by laser interference lithography for tuning surface plasmon resonance*. Optics Express, 2008. **16**(14): p. 10701.
165. Hao, Q., et al., *Effects of Intrinsic Fano Interference on Surface Enhanced Raman Spectroscopy: Comparison between Platinum and Gold*. The Journal of Physical Chemistry C, 2010. **114**(42): p. 18059-18066.
166. Liu, Z., et al., *Experimental studies of far-field superlens for sub-diffractive optical imaging*. Optics Express, 2007. **15**(11): p. 6947.
167. Hu, H., C. Ma, and Z. Liu, *Plasmonic dark field microscopy*. Applied Physics Letters, 2010. **96**(11): p. 113107.
168. Tao, H., et al., *A metamaterial absorber for the terahertz regime: design, fabrication and characterization*. Optics Express, 2008. **16**(10): p. 7181.
169. Diem, M., T. Koschny, and C. Soukoulis, *Wide-angle perfect absorber/thermal emitter in the terahertz regime*. Physical Review B, 2009. **79**(3).
170. Zheng, Y.B., et al., *Thermal behavior of localized surface plasmon resonance of Au/TiO₂ core/shell nanoparticle arrays*. Applied Physics Letters, 2007. **90**(18): p. 183117.
171. Henzie, J., et al., *Nanofabrication of plasmonic structures*. Annu Rev Phys Chem, 2009. **60**: p. 147-65.
172. Chong, T.C., M.H. Hong, and L.P. Shi, *Laser precision engineering: from microfabrication to nanoprocessing*. Laser & Photonics Reviews, 2010. **4**(1): p. 123-143.
173. Wang, X., et al., *Large-size liftable inverted-nanobowl sheets as reusable masks for nanolithography*. Nano Lett, 2005. **5**(9): p. 1784-8.
174. Hao, Q., et al., *Characterization of complementary patterned metallic membranes produced simultaneously by a dual fabrication process*. Applied Physics Letters, 2010. **97**(19): p. 193101.
175. Kravets, V., F. Schedin, and A. Grigorenko, *Plasmonic blackbody: Almost complete absorption of light in nanostructured metallic coatings*. Physical Review B, 2008. **78**(20).

176. Kravets, V.G., et al., *Plasmonic blackbody: Strong absorption of light by metal nanoparticles embedded in a dielectric matrix*. Physical Review B, 2010. **81**(16).
177. Tang, Y., et al., *Single-layer metallodielectric nanostructures as dual-band midinfrared filters*. Applied Physics Letters, 2008. **92**(26): p. 263106.
178. Jiang, Z.H., et al., *Conformal dual-band near-perfectly absorbing mid-infrared metamaterial coating*. ACS Nano, 2011. **5**(6): p. 4641-7.
179. Willets, K.A. and R.P. Van Duyne, *Localized surface plasmon resonance spectroscopy and sensing*. Annu Rev Phys Chem, 2007. **58**: p. 267-97.
180. Dodge, M.J., *Refractive Properties of Magnesium Fluoride*. Applied Optics, 1984. **23**(12): p. 1980-1985.
181. Berini, P., *Plasmon polariton modes guided by a metal film of finite width*. Optics Letters, 1999. **24**(15): p. 1011.
182. Cai, W., et al., *Metamagnetics with rainbow colors*. Optics Express, 2007. **15**(6): p. 3333.
183. Hu, C., et al., *Realizing near-perfect absorption at visible frequencies*. Optics Express, 2009. **17**(13): p. 11039.
184. Khoo, I.C., *Nonlinear optics of liquid crystalline materials*. Physics Reports, 2009. **471**(5-6): p. 221-267.
185. Tabiryan, N.V. and C. Umeton, *Surface-activated photorefractivity and electro-optic phenomena in liquid crystals*. Journal of the Optical Society of America B, 1998. **15**(7): p. 1912.
186. Liu, Y.J., et al., *Surface acoustic wave driven light shutters using polymer-dispersed liquid crystals*. Adv Mater, 2011. **23**(14): p. 1656-9.
187. Zheng, Y.B., et al., *Dynamic tuning of plasmon-exciton coupling in arrays of nanodisk-J-aggregate complexes*. Adv Mater, 2010. **22**(32): p. 3603-7.
188. Zheng, Y.B., et al., *Active molecular plasmonics: controlling plasmon resonances with molecular switches*. Nano Lett, 2009. **9**(2): p. 819-25.
189. Zheng, Y.B., et al., *Systematic investigation of localized surface plasmon resonance of long-range ordered Au nanodisk arrays*. Journal of Applied Physics, 2008. **103**(1): p. 014308.
190. Ye, T., et al., *Changing stations in single bistable rotaxane molecules under electrochemical control*. ACS Nano, 2010. **4**(7): p. 3697-701.
191. Liu, Y.J., et al., *Optically switchable gratings based on azo-dye-doped, polymer-dispersed liquid crystals*. Optics Letters, 2009. **34**(15): p. 2351.
192. Liu, Y.J., et al., *Electrically switchable phase-type fractal zone plates and fractal photon sieves*. Optics Express, 2009. **17**(15): p. 12418.
193. Li, D., et al., *Molecular, Supramolecular, and Macromolecular Motors and Artificial Muscles*. MRS Bulletin, 2011. **34**(09): p. 671-681.
194. Khoo, I.C., J. Liou, and M.V. Stinger, *Microseconds–Nanoseconds All-Optical Switching of Visible-Near Infrared (0.5 μm –1.55 μm) Lasers with Dye-Doped Nematic Liquid Crystals*. Molecular Crystals and Liquid Crystals, 2010. **527**(1): p. 109/[265]-118/[274].
195. Khoo, I.-C., J.-H. Park, and J.D. Liou, *Theory and experimental studies of all-optical transmission switching in a twist-alignment dye-doped nematic liquid crystal*. Journal of the Optical Society of America B, 2008. **25**(11): p. 1931.
196. Hrozhyk, U.A., et al., *Azobenzene liquid crystalline materials for efficient optical switching with pulsed and/or continuous wave laser beams*. Opt Express, 2010. **18**(8): p. 8697-704.
197. White, T.J., et al., *Widely tunable, photoinvertible cholesteric liquid crystals*. Adv Mater, 2011. **23**(11): p. 1389-92.

198. Graugnard, E., et al., *Electric-field tuning of the Bragg peak in large-pore TiO₂ inverse shell opals*. Physical Review B, 2005. **72**(23).
199. Li, J., et al., *Refractive Indices of Liquid Crystals for Display Applications*. Journal of Display Technology, 2005. **1**(1): p. 51-61.
200. Khoo, I.C., et al., *Passive optical self-limiter using laser-induced axially asymmetric and symmetric transverse self-phase modulations in nematic liquid crystals*. Optics Letters, 1986. **11**(4): p. 227.
201. Li, H., Y. Liang, and I.-C. Khoo, *Transient Laser Induced Orthogonal Director-Axis Reorientation in Dye-Doped Liquid Crystals (DDLC)*. Molecular Crystals and Liquid Crystals Science and Technology. Section A. Molecular Crystals and Liquid Crystals, 1994. **251**(1): p. 85-92.
202. Khoo, I.C., *Optical-DC-Field Induced Space Charge Fields and Photorefractive-Like Holographic Grating Formation in Nematic Liquid Crystals*. Molecular Crystals and Liquid Crystals Science and Technology. Section A. Molecular Crystals and Liquid Crystals, 1996. **282**(1): p. 53-66.
203. Chen, H., et al., *Plasmon coupling in clusters composed of two-dimensionally ordered gold nanocubes*. Small, 2009. **5**(18): p. 2111-9.
204. Kou, X., et al., *Curvature-directed assembly of gold nanocubes, nanobranched, and nanospheres*. Langmuir, 2009. **25**(3): p. 1692-8.
205. Wu, X., et al., *High-photoluminescence-yield gold nanocubes: for cell imaging and photothermal therapy*. ACS Nano, 2010. **4**(1): p. 113-20.
206. Lassiter, J.B., et al., *Fano resonances in plasmonic nanoclusters: geometrical and chemical tunability*. Nano Lett, 2010. **10**(8): p. 3184-9.
207. Fan, J.A., et al., *Self-assembled plasmonic nanoparticle clusters*. Science, 2010. **328**(5982): p. 1135-8.
208. Fan, J.A., et al., *Fano-like interference in self-assembled plasmonic quadrumer clusters*. Nano Lett, 2010. **10**(11): p. 4680-5.
209. Lassiter, J.B., et al., *Close encounters between two nanoshells*. Nano Lett, 2008. **8**(4): p. 1212-8.
210. Bardhan, R., et al., *Metallic nanoshells with semiconductor cores: optical characteristics modified by core medium properties*. ACS Nano, 2010. **4**(10): p. 6169-79.
211. Zoric, I., et al., *Localized surface plasmons shed light on nanoscale metal hydrides*. Adv Mater, 2010. **22**(41): p. 4628-33.
212. Langhammer, C., et al., *Localized surface plasmon resonances in aluminum nanodisks*. Nano Lett, 2008. **8**(5): p. 1461-71.
213. Liu, Y.J., et al., *All-Optical Modulation of Localized Surface Plasmon Coupling in a Hybrid System Composed of Photo-Switchable Gratings and Au Nanodisk Arrays*. J Phys Chem C Nanomater Interfaces, 2011. **115**(15): p. 7717-7722.
214. Ebbesen, T.W., et al., Nature, 1998. **391**(6668): p. 667-669.
215. Liu, Y.J., et al., *Optical Transmission Enhancement and Tuning by Overlaying Liquid Crystals on a Gold Film with Patterned Nanoholes*. Plasmonics, 2011. **6**(4): p. 659-664.
216. Nordlander, P., *The ring: a leitmotif in plasmonics*. ACS Nano, 2009. **3**(3): p. 488-92.
217. Halpern, A.R. and R.M. Corn, *Lithographically patterned electrodeposition of gold, silver, and nickel nanoring arrays with widely tunable near-infrared plasmonic resonances*. ACS Nano, 2013. **7**(2): p. 1755-62.
218. Chen, H., et al., *Gold nanorods and their plasmonic properties*. Chem Soc Rev, 2013. **42**(7): p. 2679-724.
219. Zheng, Y., et al., *Coating fabrics with gold nanorods for colouring, UV-protection, and antibacterial functions*. Nanoscale, 2013. **5**(2): p. 788-95.

220. Wurtz, G.A., et al., *Designed ultrafast optical nonlinearity in a plasmonic nanorod metamaterial enhanced by nonlocality*. Nat Nanotechnol, 2011. **6**(2): p. 107-11.
221. Wurtz, G.A., et al., *Guided plasmonic modes in nanorod assemblies: strong electromagnetic coupling regime*. Optics Express, 2008. **16**(10): p. 7460.
222. Lyvers, D.P., et al., *Gold nanorod arrays as plasmonic cavity resonators*. ACS Nano, 2008. **2**(12): p. 2569-76.
223. Kern, A.M. and O.J. Martin, *Excitation and reemission of molecules near realistic plasmonic nanostructures*. Nano Lett, 2011. **11**(2): p. 482-7.
224. Kottmann, J., et al., *Spectral response of plasmon resonant nanoparticles with a non-regular shape*. Optics Express, 2000. **6**(11): p. 213.
225. Lovera, A. and O.J.F. Martin, *Plasmonic trapping with realistic dipole nanoantennas: Analysis of the detection limit*. Applied Physics Letters, 2011. **99**(15): p. 151104.
226. Dionne, J.A., et al., *PlasMOStor: a metal-oxide-Si field effect plasmonic modulator*. Nano Lett, 2009. **9**(2): p. 897-902.
227. Dicken, M.J., et al., *Electrooptic modulation in thin film barium titanate plasmonic interferometers*. Nano Lett, 2008. **8**(11): p. 4048-52.
228. Liu, Y.J., et al., *A frequency-addressed plasmonic switch based on dual-frequency liquid crystals*. Applied Physics Letters, 2010. **97**(9): p. 091101.
229. Pala, R.A., et al., *A nonvolatile plasmonic switch employing photochromic molecules*. Nano Lett, 2008. **8**(5): p. 1506-10.
230. Zhang, X., et al., *Band-selective optical polarizer based on gold-nanowire plasmonic diffraction gratings*. Nano Lett, 2008. **8**(9): p. 2653-8.
231. Zhao, Y., M.A. Belkin, and A. Alu, *Twisted optical metamaterials for planarized ultrathin broadband circular polarizers*. Nat Commun, 2012. **3**: p. 870.
232. Wang, Y., et al., *Metamaterial-plasmonic absorber structure for high efficiency amorphous silicon solar cells*. Nano Lett, 2012. **12**(1): p. 440-5.
233. Aydin, K., et al., *Broadband polarization-independent resonant light absorption using ultrathin plasmonic super absorbers*. Nat Commun, 2011. **2**: p. 517.
234. Laux, E., et al., *Plasmonic photon sorters for spectral and polarimetric imaging*. Nature Photonics, 2008. **2**(3): p. 161-164.
235. Xu, T., et al., *Plasmonic nanoresonators for high-resolution colour filtering and spectral imaging*. Nat Commun, 2010. **1**: p. 59.
236. Liu, Y.J., et al., *Optically tunable plasmonic color filters*. Applied Physics A, 2011. **107**(1): p. 49-54.
237. Liu, Y.J., et al., *Light-driven plasmonic color filters by overlaying photoresponsive liquid crystals on gold annular aperture arrays*. Adv Mater, 2012. **24**(23): p. OP131-5.
238. Zhang, J., et al., *Continuous metal plasmonic frequency selective surfaces*. Opt Express, 2011. **19**(23): p. 23279-85.
239. Kumar, K., et al., *Printing colour at the optical diffraction limit*. Nat Nanotechnol, 2012. **7**(9): p. 557-61.
240. Si, G., et al., *Direct and accurate patterning of plasmonic nanostructures with ultrasmall gaps*. Nanoscale, 2013. **5**(10): p. 4309-13.
241. Baida, F.I. and D. Van Labeke, *Light transmission by subwavelength annular aperture arrays in metallic films*. Optics Communications, 2002. **209**(1-3): p. 17-22.
242. Baida, F.I., et al., *New design for enhanced transmission and polarization control through near-field optical microscopy probes*. Optics Communications, 2005. **256**(1-3): p. 190-195.
243. Baida, F.I., et al., *Extraordinary transmission beyond the cut-off through sub-annular aperture arrays*. Optics Communications, 2009. **282**(7): p. 1463-1466.

244. Salvi, J., et al., *Annular aperture arrays: study in the visible region of the electromagnetic spectrum*. Optics Letters, 2005. **30**(13): p. 1611.
245. Baida, F. and D. Van Labeke, *Three-dimensional structures for enhanced transmission through a metallic film: Annular aperture arrays*. Physical Review B, 2003. **67**(15).
246. Baida, F., et al., *Subwavelength metallic coaxial waveguides in the optical range: Role of the plasmonic modes*. Physical Review B, 2006. **74**(20).
247. Heshmat, B., et al., *Tuning plasmonic resonances of an annular aperture in metal plate*. Opt Express, 2011. **19**(7): p. 5912-23.
248. Orbons, S.M., et al., *Dual resonance mechanisms facilitating enhanced optical transmission in coaxial waveguide arrays*. Optics Letters, 2008. **33**(8): p. 821.
249. Banzer, P., et al., *Extraordinary transmission through a single coaxial aperture in a thin metal film*. Opt Express, 2010. **18**(10): p. 10896-904.
250. Orbons, S.M., et al., *Extraordinary optical transmission with coaxial apertures*. Applied Physics Letters, 2007. **90**(25): p. 251107.
251. Haftel, M.I., C. Schlockermann, and G. Blumberg, *Role of cylindrical surface plasmons in enhanced transmission*. Applied Physics Letters, 2006. **88**(19): p. 193104.
252. Haftel, M., C. Schlockermann, and G. Blumberg, *Enhanced transmission with coaxial nanoapertures: Role of cylindrical surface plasmons*. Physical Review B, 2006. **74**(23).
253. Barakat, E.H., M.P. Bernal, and F.I. Baida, *Second harmonic generation enhancement by use of annular aperture arrays embedded into silver and filled by lithium niobate*. Opt Express, 2010. **18**(7): p. 6530-6.
254. Burgos, S.P., et al., *A single-layer wide-angle negative-index metamaterial at visible frequencies*. Nat Mater, 2010. **9**(5): p. 407-12.
255. de Waele, R., et al., *Negative refractive index in coaxial plasmon waveguides*. Opt Express, 2010. **18**(12): p. 12770-8.
256. Rodriguez-Fortuno, F.J., et al., *Coaxial plasmonic waveguide array as a negative-index metamaterial*. Opt Lett, 2009. **34**(21): p. 3325-7.
257. Poujet, Y., J. Salvi, and F.I. Baida, *90% Extraordinary optical transmission in the visible range through annular aperture metallic arrays*. Optics Letters, 2007. **32**(20): p. 2942.
258. Belkhir, A. and F.I. Baida, *Three-dimensional finite-difference time-domain algorithm for oblique incidence with adaptation of perfectly matched layers and nonuniform meshing: Application to the study of a radar dome*. Physical Review E, 2008. **77**(5).
259. Van Labeke, D., et al., *An angle-independent Frequency Selective Surface in the optical range*. Optics Express, 2006. **14**(25): p. 11945.
260. Zhao, Y., et al., *Mechanically Tuning the Localized Surface Plasmon Resonances of Gold Nanostructure Arrays*. Journal of Nanotechnology in Engineering and Medicine, 2012. **3**(1): p. 011007.
261. Smalley, J.S., et al., *High contrast modulation of plasmonic signals using nanoscale dual-frequency liquid crystals*. Opt Express, 2011. **19**(16): p. 15265-74.
262. Zhao, Y., et al., *Nanoscale super-resolution imaging via a metal-dielectric metamaterial lens system*. Journal of Physics D: Applied Physics, 2011. **44**(41): p. 415101.
263. Atwater, H.A., *The Promise of PLASMONICS*. Scientific American sp, 2007. **17**(3): p. 56-63.
264. Pendry, J.B., D. Schurig, and D.R. Smith, *Controlling electromagnetic fields*. Science, 2006. **312**(5781): p. 1780-2.
265. Leonhardt, U., *Optical conformal mapping*. Science, 2006. **312**(5781): p. 1777-80.
266. Chen, H., C.T. Chan, and P. Sheng, *Transformation optics and metamaterials*. Nat Mater, 2010. **9**(5): p. 387-96.

267. Gordon, R., *Proposal for Superfocusing at Visible Wavelengths Using Radiationless Interference of a Plasmonic Array*. Physical Review Letters, 2009. **102**(20).
268. Fang, N., et al., *Sub-diffraction-limited optical imaging with a silver superlens*. Science, 2005. **308**(5721): p. 534-7.
269. Melville, D.O.S. and R.J. Blaikie, *Super-resolution imaging through a planar silver layer*. Optics Express, 2005. **13**(6): p. 2127.
270. Jacob, Z., L.V. Alekseyev, and E. Narimanov, *Optical Hyperlens: Far-field imaging beyond the diffraction limit*. Optics Express, 2006. **14**(18): p. 8247.
271. Zhao, Y., et al., *Super resolution imaging by compensating oblique lens with metallodielectric films*. Optics Express, 2008. **16**(8): p. 5697.
272. Hao, Q., et al., *Frequency-addressed tunable transmission in optically thin metallic nanohole arrays with dual-frequency liquid crystals*. Journal of Applied Physics, 2011. **109**(8): p. 084340.
273. Hsiao, V.K.S., et al., *Light-Driven Plasmonic Switches Based on Au Nanodisk Arrays and Photoresponsive Liquid Crystals*. Advanced Materials, 2008. **20**(18): p. 3528-3532.
274. Zheng, Y.B., et al., *Incident-angle-modulated molecular plasmonic switches: a case of weak exciton-plasmon coupling*. Nano Lett, 2011. **11**(5): p. 2061-5.
275. Zheng, Y.B., B. Kiraly, and T.J. Huang, *Molecular machines drive smart drug delivery*. Nanomedicine (Lond), 2010. **5**(9): p. 1309-12.
276. Zheng, Y.B., *Light-driven artificial molecular machines*. Journal of Nanophotonics, 2010. **4**(1): p. 042501.
277. Juluri, B.K., et al., *Coupling between Molecular and Plasmonic Resonances: Effect of Molecular Absorbance*. The Journal of Physical Chemistry C, 2009. **113**(43): p. 18499-18503.
278. Huang, T.J., *Recent Developments in Artificial Molecular-Machine-Based Active Nanomaterials and Nanosystems*. MRS Bulletin, 2011. **33**(03): p. 226-231.
279. Huang, T.J., et al., *A nanomechanical device based on linear molecular motors*. Applied Physics Letters, 2004. **85**(22): p. 5391.
280. Srituravanich, W., et al., *Flying plasmonic lens in the near field for high-speed nanolithography*. Nat Nanotechnol, 2008. **3**(12): p. 733-7.
281. Juluri, B.K., et al., *Scalable manufacturing of plasmonic nanodisk dimers and cusp nanostructures using salting-out quenching method and colloidal lithography*. ACS Nano, 2011. **5**(7): p. 5838-47.
282. Hao, Q., et al., *Metallic membranes with subwavelength complementary patterns: distinct substrates for surface-enhanced Raman scattering*. ACS Nano, 2011. **5**(7): p. 5472-7.
283. Zheng, Y.B., et al., *Ordered Au Nanodisk and Nanohole Arrays: Fabrication and Applications*. Journal of Nanotechnology in Engineering and Medicine, 2010. **1**(3): p. 031011.
284. MacDonald, K.F. and N.I. Zheludev, *Active plasmonics: current status*. Laser & Photonics Reviews, 2009. **4**(4): p. 562-567.
285. Dionne, J.A., et al., *Silicon-Based Plasmonics for On-Chip Photonics*. IEEE Journal of Selected Topics in Quantum Electronics, 2010. **16**(1): p. 295-306.
286. Zheng, Y.B., et al., *Chemically Tuning the Localized Surface Plasmon Resonances of Gold Nanostructure Arrays*. The Journal of Physical Chemistry C, 2009. **113**(17): p. 7019-7024.
287. Cai, W., J.S. White, and M.L. Brongersma, *Compact, high-speed and power-efficient electrooptic plasmonic modulators*. Nano Lett, 2009. **9**(12): p. 4403-11.
288. Elezzabi, A.Y., et al., *Ultrafast all-optical modulation in silicon-based nanoplasmonic devices*. Optics Express, 2009. **17**(13): p. 11045.

289. Pacifici, D., H.J. Lezec, and H.A. Atwater, *All-optical modulation by plasmonic excitation of CdSe quantum dots*. Nature Photonics, 2007. **1**(7): p. 402-406.
290. Krasavin, A.V. and N.I. Zheludev, *Active plasmonics: Controlling signals in Au/Ga waveguide using nanoscale structural transformations*. Applied Physics Letters, 2004. **84**(8): p. 1416.
291. Krasavin, A.V., et al., *High-contrast modulation of light with light by control of surface plasmon polariton wave coupling*. Applied Physics Letters, 2004. **85**(16): p. 3369.
292. Gagnon, G., et al., *Thermally Activated Variable Attenuation of Long-Range Surface Plasmon-Polariton Waves*. Journal of Lightwave Technology, 2006. **24**(11): p. 4391-4402.
293. Wiley, B., et al., *Shape-Controlled Synthesis of Silver and Gold Nanostructures*. MRS Bulletin, 2011. **30**(05): p. 356-361.
294. Xia, Y. and N.J. Halas, *Shape-Controlled Synthesis and Surface Plasmonic Properties of Metallic Nanostructures*. MRS Bulletin, 2011. **30**(05): p. 338-348.
295. Murray, W.A., J.R. Suckling, and W.L. Barnes, *Overlayers on silver nanotriangles: Field confinement and spectral position of localized surface plasmon resonances*. Nano Lett, 2006. **6**(8): p. 1772-7.
296. Sun, Y. and Y. Xia, *Shape-controlled synthesis of gold and silver nanoparticles*. Science, 2002. **298**(5601): p. 2176-9.
297. Wang, H., et al., *Nanorice: a hybrid plasmonic nanostructure*. Nano Lett, 2006. **6**(4): p. 827-32.
298. Wang, H., et al., *Plasmonic nanostructures: artificial molecules*. Acc Chem Res, 2007. **40**(1): p. 53-62.
299. Yonzon, C.R., et al., *Towards advanced chemical and biological nanosensors-An overview*. Talanta, 2005. **67**(3): p. 438-48.
300. Juluri, B.K., et al., *Effects of Geometry and Composition on Charge-Induced Plasmonic Shifts in Gold Nanoparticles*. The Journal of Physical Chemistry C, 2008. **112**(19): p. 7309-7317.
301. MacDonald, K.F., et al., *Ultrafast active plasmonics*. Nature Photonics, 2008. **3**(1): p. 55-58.
302. Liu, Y.J., et al., *High-speed optical humidity sensors based on chiral sculptured thin films*. Sensors and Actuators B: Chemical, 2011. **156**(2): p. 593-598.
303. Chen, X., et al., *Langmuir-Blodgett patterning: a bottom-up way to build mesostructures over large areas*. Acc Chem Res, 2007. **40**(6): p. 393-401.
304. Yang, S., et al., *Surface Nanometer-Scale Patterning in Realizing Large-Scale Ordered Arrays of Metallic Nanoshells with Well-Defined Structures and Controllable Properties*. Advanced Functional Materials, 2010. **20**(15): p. 2527-2533.
305. Collings, N., et al., *Evolutionary development of advanced liquid crystal spatial light modulators*. Appl Opt, 1989. **28**(22): p. 4740-7.
306. Konshina, E.A., et al., *Optical modulators based on a dual-frequency nematic liquid crystal*. Journal of Optical Technology, 2008. **75**(10): p. 670.
307. Huang, Y., C.-H. Wen, and S.-T. Wu, *Polarization-independent and submillisecond response phase modulators using a 90° twisted dual-frequency liquid crystal*. Applied Physics Letters, 2006. **89**(2): p. 021103.
308. Xianyu, H., S.-T. Wu, and C.-L. Lin, *Dual frequency liquid crystals: a review*. Liquid Crystals, 2009. **36**(6-7): p. 717-726.
309. Wu, S.-T. and U. Efron, *Optical properties of thin nematic liquid crystal cells*. Applied Physics Letters, 1986. **48**(10): p. 624.

310. Cuennet, J.G., et al., *Optofluidic modulator based on peristaltic nematogen microflows*. Nature Photonics, 2011. **5**(4): p. 234-238.
311. Bunning, T.J., et al., *HOLOGRAPHIC POLYMER-DISPERSED LIQUID CRYSTALS (H-PDLCs) I*. Annual Review of Materials Science, 2000. **30**(1): p. 83-115.
312. Fan, Y.-H., et al., *Dual-frequency liquid crystal gels with submillisecond response time*. Applied Physics Letters, 2004. **85**(13): p. 2451.
313. Wen, C.-H. and S.-T. Wu, *Dielectric heating effects of dual-frequency liquid crystals*. Applied Physics Letters, 2005. **86**(23): p. 231104.
314. Graugnard, E., et al., *Enhanced tunable Bragg diffraction in large-pore inverse opals using dual-frequency liquid crystal*. Applied Physics Letters, 2007. **91**(11): p. 111101.
315. Pishnyak, O., S. Sato, and O.D. Lavrentovich, *Electrically tunable lens based on a dual-frequency nematic liquid crystal*. Applied Optics, 2006. **45**(19): p. 4576.
316. Shi, H., et al., *Beam manipulating by metallic nano-slits with variant widths*. Optics Express, 2005. **13**(18): p. 6815.
317. Smolyaninov, I.I., Y.J. Hung, and C.C. Davis, *Magnifying superlens in the visible frequency range*. Science, 2007. **315**(5819): p. 1699-701.
318. Pendry, J.B., *Negative Refraction Makes a Perfect Lens*. Physical Review Letters, 2000. **85**(18): p. 3966-3969.
319. Shelby, R.A., D.R. Smith, and S. Schultz, *Experimental verification of a negative index of refraction*. Science, 2001. **292**(5514): p. 77-9.
320. Kwon, D.-H., et al., *Near-infrared metamaterials with dual-band negative-index characteristics*. Optics Express, 2007. **15**(4): p. 1647.
321. Yao, J., et al., *Optical negative refraction in bulk metamaterials of nanowires*. Science, 2008. **321**(5891): p. 930.
322. Valentine, J., et al., *Three-dimensional optical metamaterial with a negative refractive index*. Nature, 2008. **455**(7211): p. 376-9.
323. Pendry, J.B. and S.A. Ramakrishna, *Refining the perfect lens*. Physica B: Condensed Matter, 2003. **338**(1-4): p. 329-332.
324. Melville, D.O.S. and R.J. Blaikie, *Experimental comparison of resolution and pattern fidelity in single- and double-layer planar lens lithography*. Journal of the Optical Society of America B, 2006. **23**(3): p. 461.
325. Podolskiy, V.A. and E.E. Narimanov, *Near-sighted superlens*. Optics Letters, 2005. **30**(1): p. 75.
326. Lee, H., et al., *Realization of optical superlens imaging below the diffraction limit*. New Journal of Physics, 2005. **7**: p. 255-255.
327. Lin, L., et al., *A cone-shaped concentrator with varying performances of concentrating*. Optics Express, 2008. **16**(10): p. 6809.
328. Lin, L., et al., *Design of electromagnetic refractor and phase transformer using coordinate transformation theory*. Optics Express, 2008. **16**(10): p. 6815.
329. Valentine, J., et al., *An optical cloak made of dielectrics*. Nat Mater, 2009. **8**(7): p. 568-71.
330. Ergin, T., et al., *Three-dimensional invisibility cloak at optical wavelengths*. Science, 2010. **328**(5976): p. 337-9.
331. Kwon, D.-H. and D.H. Werner, *Two-dimensional eccentric elliptic electromagnetic cloaks*. Applied Physics Letters, 2008. **92**(1): p. 013505.
332. Kwon, D.-H. and D.H. Werner, *Two-dimensional electromagnetic cloak having a uniform thickness for elliptic cylindrical regions*. Applied Physics Letters, 2008. **92**(11): p. 113502.

333. Yang, J., et al., *Metamaterial electromagnetic concentrators with arbitrary geometries*. Opt Express, 2009. **17**(22): p. 19656-61.
334. Lee, H., et al., *Development of optical hyperlens for imaging below the diffraction limit*. Optics Express, 2007. **15**(24): p. 15886.
335. Xiong, Y., et al., *Two-dimensional imaging by far-field superlens at visible wavelengths*. Nano Lett, 2007. **7**(11): p. 3360-5.
336. Belov, P. and Y. Hao, *Subwavelength imaging at optical frequencies using a transmission device formed by a periodic layered metal-dielectric structure operating in the canalization regime*. Physical Review B, 2006. **73**(11).
337. Belov, P.A., et al., *Experimental study of the subwavelength imaging by a wire medium slab*. Applied Physics Letters, 2006. **89**(26): p. 262109.
338. Zhao, Y., P.A. Belov, and Y. Hao, *Spatially dispersive finite-difference time-domain analysis of sub-wavelength imaging by the wire medium slabs*. Optics Express, 2006. **14**(12): p. 5154.
339. Belov, P., et al., *Transmission of images with subwavelength resolution to distances of several wavelengths in the microwave range*. Physical Review B, 2008. **77**(19).
340. Schurig, D. and D.R. Smith, *Sub-diffraction imaging with compensating bilayers*. New Journal of Physics, 2005. **7**: p. 162-162.
341. Moharam, M.G., et al., *Formulation for stable and efficient implementation of the rigorous coupled-wave analysis of binary gratings*. Journal of the Optical Society of America A, 1995. **12**(5): p. 1068.
342. Smith, D. and D. Schurig, *Electromagnetic Wave Propagation in Media with Indefinite Permittivity and Permeability Tensors*. Physical Review Letters, 2003. **90**(7).
343. Wood, B., J. Pendry, and D. Tsai, *Directed subwavelength imaging using a layered metal-dielectric system*. Physical Review B, 2006. **74**(11).
344. Liu, Z., et al., *Focusing surface plasmons with a plasmonic lens*. Nano Lett, 2005. **5**(9): p. 1726-9.
345. Chang, C.K., et al., *Recording Bessel-like beam shapes generated by plasmonics lens*. Optics Express, 2009. **17**(16): p. 13946.
346. Lerman, G.M., A. Yanai, and U. Levy, *Demonstration of nanofocusing by the use of plasmonic lens illuminated with radially polarized light*. Nano Lett, 2009. **9**(5): p. 2139-43.
347. Shackleford, J.A., et al., *Integrated plasmonic lens photodetector*. Applied Physics Letters, 2009. **94**(8): p. 083501.
348. Fu, Y., et al., *Experimental investigation of superfocusing of plasmonic lens with chirped circular nanoslits*. Opt Express, 2010. **18**(4): p. 3438-43.
349. Atwater, H.A., *The Promise of Plasmonics*. Scientific American, 2007. **296**(4): p. 56-62.
350. Martin-Moreno, L., *Plasmonic circuits: Detecting unseen light*. Nature Physics, 2009. **5**(7): p. 457-458.
351. Chen, W., et al., *Experimental confirmation of miniature spiral plasmonic lens as a circular polarization analyzer*. Nano Lett, 2010. **10**(6): p. 2075-9.
352. Yang, S., et al., *Miniature circular polarization analyzer with spiral plasmonic lens*. Opt Lett, 2009. **34**(20): p. 3047-9.
353. Verslegers, L., et al., *Planar lenses based on nanoscale slit arrays in a metallic film*. Nano Lett, 2009. **9**(1): p. 235-8.
354. Lin, L., et al., *Plasmonic lenses formed by two-dimensional nanometric cross-shaped aperture arrays for Fresnel-region focusing*. Nano Lett, 2010. **10**(5): p. 1936-40.

- 355. Kim, S., et al., *Off-axis directional beaming of optical field diffracted by a single subwavelength metal slit with asymmetric dielectric surface gratings*. Applied Physics Letters, 2007. **90**(5): p. 051113.
- 356. Liu, Z., et al., *Tuning the focus of a plasmonic lens by the incident angle*. Applied Physics Letters, 2006. **88**(17): p. 171108.
- 357. Bozhevolnyi, S.I., et al., *Channel plasmon subwavelength waveguide components including interferometers and ring resonators*. Nature, 2006. **440**(7083): p. 508-11.
- 358. Verhagen, E., A. Polman, and L. Kuipers, *Nanofocusing in laterally tapered plasmonic waveguides*. Optics Express, 2008. **16**(1): p. 45.
- 359. Pile, D.F.P. and D.K. Gramotnev, *Channel plasmon-polariton in a triangular groove on a metal surface*. Optics Letters, 2004. **29**(10): p. 1069.
- 360. Sondergaard, T., et al., *Extraordinary optical transmission enhanced by nanofocusing*. Nano Lett, 2010. **10**(8): p. 3123-8.
- 361. Stegeman, G.I., R.F. Wallis, and A.A. Maradudin, *Excitation of surface polaritons by end-fire coupling*. Optics Letters, 1983. **8**(7): p. 386.
- 362. Gordon, R. and A.G. Brolo, *Increased cut-off wavelength for a subwavelength hole in a real metal*. Optics Express, 2005. **13**(6): p. 1933.
- 363. Sun, Z. and H.K. Kim, *Refractive transmission of light and beam shaping with metallic nano-optic lenses*. Applied Physics Letters, 2004. **85**(4): p. 642.
- 364. Fu, Y., et al., *Plasmonic microzone plate: Superfocusing at visible regime*. Applied Physics Letters, 2007. **91**(6): p. 061124.

VITA

Yanhui Zhao

Yanhui Zhao received his bachelor degree from Zhejiang University at 2006. After that, he joined Institute of Optics and Electronics, Chinese Academy of Sciences for his master studies and graduated at 2009 with a presidential award for his research excellence. Since then, he has been working with Professor Tony Jun Huang at Penn State University for his Ph.D studies, with his research topics focusing on interdisciplinary research concerning optics, nanotechnology, microfluidics, and fundamental biochemistry. He made distinctive achievements during his Ph.D studies, with **36** journal publications (a total number of 41) and **625** citations (a total number of 639) after he joined Penn State, 2 conference talks and multiple conference proceedings. 5 of his works were selected as front journal cover images by American Institute of Physics (AIP) and Royal Society of Chemistry (RSC). Another 5 of his works were listed among the top 20 most download/read articles on journals of *Lab on a Chip*, *Nanoscale*, *Biomicrofluidics*, and *Applied Physics Letters*. Some of his works attracted attentions from various websites and mediums, including the National Science Foundation and technical websites such as ScienceDaily, PHYS.ORG, etc. He was also the recipients of several most prestigious awards and scholarships for his research achievements, including the 2014 Penn State Alumni Association Dissertation Award, 2013 Boris P. Stoicheff Memorial Scholarship from the Optical Society (OSA) and Canadian Association of Physicists (CAP), the 2013 Harold K. Schilling Dean's Graduate Scholarship of Penn State Graduate School, and 2012 Optics and Photonics Education Scholarship from the International Society of Optics and Photonics (SPIE). In addition, he served as reviewers for 24 scientific journals, including top ranked journals such as *Advanced Materials*, *Advanced Functional Materials*, *Optics Letters*, *Optics Express*, *Lab on a Chip*, *Nanoscale*, and other prestigious journals in optics, material science, and analytical chemistry.